

# UC Riverside

## UC Riverside Electronic Theses and Dissertations

### Title

Coordination Chemistry Enables Tunable Crosslinking, Reversible Phase Transition, and 3D Printing of Hydrogels for Biomedical Applications

### Permalink

<https://escholarship.org/uc/item/2jz375tg>

### Author

Xu, Changlu

### Publication Date

2022

Peer reviewed|Thesis/dissertation

UNIVERSITY OF CALIFORNIA  
RIVERSIDE

Coordination Chemistry Enables Tunable Crosslinking, Reversible Phase Transition, and  
3D Printing of Hydrogels for Biomedical Applications

A Dissertation submitted in partial satisfaction  
of the requirements for the degree of

Doctor of Philosophy

in

Materials Science and Engineering

by

Changlu Xu

December 2022

Dissertation Committee:

Dr. Huinan H. Liu, Chairperson

Dr. Jianzhong Wu

Dr. Iman Noshadi

Copyright by  
Changlu Xu  
2022

The Dissertation of Changlu Xu is approved:

---

---

---

Committee Chairperson

University of California, Riverside

## **Acknowledgements**

I would like to thank my wife, my soul mate, and my closest friend, Mrs. Jing Liu, for her support, companionship, and love while I am pursuing my dreams. We have helped and encouraged each other and built our lives together over the last six years. I would want to express my gratitude to my parents for their unwavering support, encouragement, and love. Despite their limited knowledge and lack of expressiveness, my parents have always done their utmost to safeguard my development. I would also want to thank my elder sister for her companionship throughout my childhood and youth, which provided me with many happy memories. I would also want to express my gratitude to my grandma, a traditional Chinese lady who spent her whole life in a distant and underdeveloped rural part of China. She had contributed to my success in silence, allowing me to grow from a child to a man of unbreakable spirit. I pray for her happiness in paradise.

I would like to thank Dr. Huinan Liu, my PhD adviser, for her consistent support, advice, and encouragement during my PhD studies. Additionally, I would like to thank Drs. Jianzhong Wu and Iman Noshadi for their informative and professional feedback on my PhD defense and dissertation. I would also want to send my sincere thank to my colleagues and friends, Dr. Chaoxing Zhang, Dr. Wensen Jiang, Dr. Jiajia Lin, Dr. Dongwei Sun, Dr. Wayne Leu, Dr. Xiang Yu, Dr. Xijuan Chai, Dr. Naiyin Zhang, Mrs. Patricia Holt-Torres, Miss Yiqing Chen, Miss Jinrui Tan, Mr. Jing Mu, Mr. Ruoyu

Sheng, and Mr. Ivan Chiang for their support and help in my academic and personal lives.

The text of this dissertation, in part or in full, is a reprint of the material as it appears in “Tunable Crosslinking, Reversible Phase Transition, and 3D Printing of Hyaluronic Acid Hydrogels via Dynamic Coordination of Innate Carboxyl Groups and Metallic Ions. ACS Applied Bio Materials. 2021, 4, 3, 2408–2428” and “Direct and Indirect Culture Methods for Studying Biodegradable Implant Materials In Vitro. Journal of Visualized Experiments: Jove. 2022, 182, e63065”. The co-author listed in these publications directed and supervised the research which forms the basis for this dissertation.

I would like to acknowledge UC Riverside Dean’s Distinguished Fellowship, U.S. National Science Foundation (NSF) Partnerships in Research (NSF PIRE 1545852), NSF Non-Academic Research Internship Award, UC Riverside Stem Cell Center Travel Award, NSF INNOVAR Award, NSF MVP/PoC Prototyping Award, and UC Riverside Dissertation Year Program Award (DYP) for the financial support.

## ABSTRACT OF THE DISSERTATION

Coordination Chemistry Enables Tunable Crosslinking, Reversible Phase Transition, and 3D Printing of Hydrogels for Biomedical Applications

by

Changlu Xu

Doctor of Philosophy, Graduate Program in Materials Science and Engineering  
University of California, Riverside, December 2022  
Dr. Huinan H. Liu, Chairperson

Hyaluronic acid (HyA) hydrogels are promising in various biomedical applications such as tissue regeneration, drug delivery, cell therapy, and biosensing. Three-dimensional printing (3D printing) can precisely control the structures and properties of the HyA hydrogels, which is highly desirable for many biomedical applications. However, the crosslinking and 3D printing of HyA hydrogels usually require chemical modifications. This may raise toxicity concerns on the hydrogels, especially when regulatory approval is required for the clinical translation of the final products. This dissertation investigated the mechanisms of dynamic coordination and the relationships among the key parameters in controlling the tunable crosslinking, reversible phase transition, and 3D printing of HyA hydrogels for biomedical applications, without blending with other polymers or adding new functional groups. In the first part, tunable crosslinking and reversible phase transition of HyA hydrogels were achieved and

demonstrated via dynamic coordination of  $\text{Fe}^{3+}$  ions with innate carboxyl groups. The concentrations of  $\text{Fe}^{3+}$  and  $\text{H}^+$  ions and the reaction time determine the coordination state, leading to the low-to-high crosslinking densities and reversible solid-liquid phase transition of HyA hydrogels. In chapters 3 and 4, three different 3D printing approaches for HyA hydrogels were developed, for the first time. Two 3D printing strategies, namely cold-stage and direct-writing methods, were achieved based on the tunable crosslinking and reversible phase transition of the HyA hydrogel. Direct writing of HyA solution in  $\text{FeCl}_3$  solution was also achieved by decelerating the solidification process of the hydrogel in  $\text{FeCl}_3$  solution. In chapter 5, the cytocompatibility of HyA hydrogels with different crosslinking densities and 3D-printed HyA constructs was investigated via the direct exposure culture method with bone marrow-derived mesenchymal stem cells (BMSCs). The last part of this dissertation investigated the incorporation of magnetic nanoparticles (MNPs) in the HyA hydrogels in situ. The MNP content and agglomeration in the magnetic hydrogels were tunable by controlling concentrations of  $\text{Fe}^{3+}$  and  $\text{Fe}^{2+}$  ions. Cell study results indicated that BMSC adhesion density decreased when increasing the MNP content in HyA hydrogels.

## Table of Contents

Acknowledgements.....	iv
Table of Contents.....	viii
List of Figures.....	xiv
CHAPTER 1 Background on the Crosslinking and Three-Dimensional Printing of Hyaluronic Acid Hydrogels for Biomedical Applications.....	1
CHAPTER 2 Tunable Crosslinking and Reversible Phase Transition of Hyaluronic Acid Hydrogels via Dynamic Coordination of Carboxyl Groups and Metallic Ions .....	5
2.1 Introduction.....	5
2.2 Materials and Methods.....	6
2.2.1 Determine the Effects of Fe <sup>3+</sup> Concentration and pH Value on the Crosslinking Densities and Reversible Phase Transition of HyA Hydrogels .....	6
2.2.2 Demonstrate the Tunable Crosslinking and Reversible Phase Transition of HyA Hydrogels.....	8
2.2.3 Measure the Reduction of Size, Volume, and Water Content and the Release of Fe <sup>3+</sup> Ions During the Phase Transition From HyA_M to HyA_H.....	9
2.2.4 Characterize Microstructure and Properties of the HyA_L, HyA_M, HyA_H, and HyA.....	12
2.3 Results.....	15

2.3.1 Tunable Ratios of Mono-, Bi- and Tridentate Coordination in HyA Determine the Low-to-High Crosslinking Densities and Solid-Liquid Reversibility of Hydrogels ....	15
2.3.2 The Effects of Fe <sup>3+</sup> Concentration and pH Value on the Tunable Ratios of Mono-, Bi-, and Tridentate Coordination and the Resulted Low-to-High Crosslinking Densities of HyA Hydrogels.....	19
2.3.3 Reversible Solid-Liquid Phase Transition of HyA Hydrogels Achieved via the Tunable Ratios of Mono-, Bi-, and Tridentate Coordination and the Resulted Low-to-High Crosslinking Densities .....	23
2.3.4 The Microstructure, Composition, Thermal, Chemical, Mechanical, and Rheological Properties of HyA Hydrogels With Low-to-High Crosslinking Densities	28
2.4 Discussion .....	38
2.5 Conclusion .....	42
CHAPTER 3 Three-Dimensional Printing of Hyaluronic Acid Hydrogels via Reversible Phase Transition: Cold-Stage and Direct Writing Approaches .....	43
3.1 Introduction.....	43
3.2 Materials and Methods.....	45
3.2.1 Determine the Conditions for Preparing HyA_P .....	45
3.2.2 Demonstrate Cold-Stage Method and Direct Writing Method for 3D-Printing of the HyA_P.....	45

3.2.3 Evaluate the Morphology and Structural Stability of the Filaments Printed by Two Different Methods.....	46
3.3 Results.....	47
3.3.1 Effects of Fe <sup>3+</sup> and H <sup>+</sup> Ion Concentrations and Reaction Time on HyA_P for 3DP .....	47
3.3.2 Morphology and Structural Stability of 3D Printed HyA Hydrogels via Cold-Stage and Direct Writing Methods .....	52
3.4 Discussion.....	55
3.5 Conclusion .....	57
CHAPTER 4 Direct Writing of Hyaluronic Acid Solution in Fe <sup>3+</sup> Ion Solution .....	58
4.1 Introduction.....	58
4.2 Materials and Methods.....	59
4.2.1 Preload Cations in HyA Solution.....	59
4.2.2 Measure the Rheological Properties .....	59
4.2.3 Characterize the Chemical Bonding .....	60
4.2.4 Determine the Direct Writing Capability of HyA Solution.....	60
4.2.5 Determine the Boundary Condition of Reaction Time .....	61
4.2.6 Determine the Boundary Condition of pH of Water.....	61
4.2.7 Demonstrate the Direct Writing of HyA Solution in FeCl <sub>3</sub> Solution .....	62

4.2.8 Determine the Effects of HyA Concentration and FeCl <sub>3</sub> Solution Concentration on the Shrinkage Coefficient of HyA Hydrogels During Phase Transition.....	62
4.3 Results.....	63
4.3.1 Direct Writing of HyA Solution in FeCl <sub>3</sub> Solution.....	63
4.3.2 Rheological Properties of HyA Solution Preloaded With Cations .....	65
4.3.3 Direct Writing Capability of HyA Solution Preloaded With Cations.....	70
4.3.4 Minimum and Maximum Reaction Time in Solution II.....	72
4.3.5 Effects of pH Value of Water .....	75
4.3.6 Demonstration of Direct Writing of HyA Solution in FeCl <sub>3</sub> Solution.....	76
4.3.7 Effects of HyA Concentration and FeCl <sub>3</sub> Solution Concentration on the Shrinkage Coefficient of HyA Hydrogels During Phase Transition .....	76
4.4 Discussion.....	78
4.5 Conclusion .....	79
CHAPTER 5 Cytocompatibility of Hyaluronic Acid Hydrogels Crosslinked via Dynamic Coordination of Innate Carboxyl Groups and Metallic Ions .....	80
5.1 Introduction.....	80
5.2 Materials and Methods.....	82
5.2.1 Evaluate the Cytocompatibility of HyA Hydrogels With BMSCs in Direct Exposure Culture <i>in Vitro</i> .....	82

5.2.2 Evaluate the Cytocompatibility of HyA Hydrogels Prepared via Direct Writing of HyA Solution in FeCl <sub>3</sub> Solution .....	89
5.3 Results.....	90
5.3.1 Cytocompatibility of HyA Hydrogels With BMSCs in Direct Exposure Culture <i>in Vitro</i> .....	90
5.3.2 Cytocompatibility of HyA Hydrogels Prepared via Direct Writing of HyA Solution in FeCl <sub>3</sub> Solution .....	100
5.4 Discussion.....	103
5.4.1 Phase Transition of HyA Hydrogels in Cell Culture Environment .....	103
5.4.2 Strategies on Addressing the Toxicity Concern of Fe <sup>3+</sup> and H <sup>+</sup> Ions in the Crosslinked HyA Hydrogels .....	104
5.4.3 Prospects of HyA Hydrogels Crosslinked via Carboxylate-Fe <sup>3+</sup> Coordination for Biomedical Applications.....	107
5.5 Conclusion .....	110
CHAPTER 6 Incorporation of Magnetic Nanoparticles in the Hyaluronic Acid Hydrogels in Situ for Biomedical Applications .....	111
6.1 Introduction.....	111
6.2 Materials and Methods.....	114
6.2.1 Incorporate MNPs in HyA Hydrogels in Situ.....	114
6.2.2 Determine Microstructure and Elemental Composition .....	115

6.2.3 Determine Magnetic Response .....	116
6.2.4 Thermogravimetric Analysis .....	116
6.2.5 Crystal Structure .....	117
6.2.6 Evaluation of the Cytocompatibility of Magnetic Hydrogels.....	117
6.2.7 Statistical Analysis.....	120
6.3 Results.....	121
6.3.1 Microstructure and Elemental Composition .....	121
6.3.2 Magnetic Responses.....	123
6.3.3 MNP Content and Crystal Structure .....	124
6.3.4 Cytocompatibility of Magnetic Hydrogels With BMSC in Vitro.....	126
6.4 Discussion .....	130
6.5 Conclusion .....	131
Reference .....	133

## List of Figures

- Figure 1.1** Functionalization strategies of HyA molecule. .... 2
- Figure 2.1** The innate pH values of FeCl<sub>3</sub> solutions at different concentrations. .... 15
- Figure 2.2** Schematics for controlling dynamic Fe<sup>3+</sup>-carboxyl coordination states and tunable crosslinking densities of HyA hydrogels. (a) Illustration for dynamic carboxylate-Fe<sup>3+</sup> ion coordination when sodium HyA solution is mixed with FeCl<sub>3</sub> solution. Each disaccharide unit of HyA molecular chain has one carboxyl group. The FeCl<sub>3</sub> solution consists of Fe<sup>3+</sup> ion, Fe<sup>3+</sup> complex, H<sup>+</sup> ion, and other Cl<sup>-</sup> counter ions. Fe<sup>3+</sup> could form mono-, bi-, and tridentate coordination bonding with carboxyl groups on HyA chains, and the carboxyl groups can also bond with H<sup>+</sup> in the acidic FeCl<sub>3</sub> solution. (b) The key parameters of Fe<sup>3+</sup> and H<sup>+</sup> concentrations and the reaction time determine the coordination states of HyA hydrogels and the tunable crosslinking densities. (c) Illustration for the reversibility of HyA hydrogels with low-to-high crosslinking densities. (1) HyA\_L with a low degree of crosslinking has a monodentate-dominant coordination state. (2) HyA\_M with a medium degree of crosslinking has a mixed state of mono-, bi-, and tridentate coordination. (3) HyA\_H with a high crosslinking density has a tridentate-dominant coordination state. HyA\_P with the crosslinking densities between HyA\_L and HyA\_M is 3D printable. .... 18
- Figure 2.3** The structural stability of crosslinked HyA hydrogels demonstrated the effects of Fe<sup>3+</sup> concentration and pH value on the tunable crosslinking of HyA hydrogels. (a) The representative photographs of as-injected (or as-printed) network pattern of HyA solution in the well at time zero (T=0 h) and HyA gels immersed in 2 to 300 mM of FeCl<sub>3</sub> solutions with innate pH values after 24 hours of reaction (T=24 h). (b) The representative photographs of as-injected (or as-printed) network pattern of HyA solution in the well at time zero (T=0 h) and HyA gels in 10 mM, 20 mM, and 30 mM FeCl<sub>3</sub> solution with decreasing pH values after 24 hours of reaction (T=24 h)..... 21
- Figure 2.4** The storage modulus of crosslinked HyA hydrogels demonstrated the effects of Fe<sup>3+</sup> concentration, pH value, and reaction time on the tunable crosslinking of HyA hydrogels. (a) The curves of storage modulus over shear strain for HyA hydrogels crosslinked with 10 mM, 20 mM, and 30 mM FeCl<sub>3</sub> solutions with a constant pH of 1.7 for 5 min (Left), 15 min (Middle), and 30 min (Right). (b) The curves of storage modulus over shear strain for HyA hydrogels crosslinked in the 20 mM FeCl<sub>3</sub> solution with an adjusted pH value of 1.5, 1.7, and 1.9, respectively, for 5 min (Left), 15 min (Middle), and 30 min (Right). .... 22
- Figure 2.5** Reversible phase transition of crosslinked HyA hydrogels with low (HyA\_L), medium (HyA\_M), and high (HyA\_H) crosslinking densities. (a) Evidence of phase transition from HyA\_M to HyA\_L, from HyA\_M to HyA\_H, and from HyA\_L to HyA\_H. Specifically, adding 300 mM FeCl<sub>3</sub> solution (indicated in brown color) in the

PTFE mold caused crosslinking of HyA solution (indicated in green color). A soft flexible gel (HyA\_M) formed after a 5-min reaction and a viscous liquid gel (HyA\_L) formed after a 1-h reaction. A hard and stiff hydrogel (HyA\_H) formed by immersing HyA\_M or HyA\_L in DI water for 24 hours. (b) Evidence of phase transition from HyA\_L to HyA\_M. The as-injected HyA\_L transformed to HyA\_M after a 5-min immersion in 30 mM FeCl<sub>3</sub> solution. (c) Evidence of phase transition from HyA\_H to HyA\_M and from HyA\_H to HyA\_L. HyA\_H transformed to HyA\_M after being immersed in 300 mM FeCl<sub>3</sub> solution for 1 hour; HyA\_H transformed to HyA\_L after a 2-h immersion in 300 mM FeCl<sub>3</sub> solution..... 25

**Figure 2.6** Volume shrinkage of HyA hydrogels. (a) Photographs showing that the HyA\_M in DI water had a dramatic volume shrinkage over time to become HyA\_H (from left to right). (b) Diameter and volume change ratio overtime during the phase transition from HyA\_M to HyA\_H in DI water. Diameter is shown on the left axis with data in red and volume change ratio is shown on the right axis with data in blue. Data are shown as mean ± standard deviation (n=3). Inset is the magnified graph of the first 4 hours. (c) The water content of the hydrogel overtime during the phase transition from HyA\_M to HyA\_H in DI water. Data are shown as mean ± standard deviation (n=3). Inset is the magnified graph of the first 4 hours. (d) Cumulative Fe<sup>3+</sup> released overtime during the phase transition from HyA\_M to HyA\_H in DI water. Data are shown as mean ± standard deviation (n=3). Inset is the magnified graph of the first 4 hours..... 27

**Figure 2.7** SEM images of cross-sections of lyophilized HyA\_M, HyA\_H, and HyA at the original magnifications of 1000× and 10000×, and the overlay of SEM and EDS maps for HyA\_M and HyA\_H at the original magnification of 10000×. Red circles indicate the areas that were magnified in the images highlighted with the red border. Fe elemental distribution in EDS maps is indicated by red color. .... 29

**Figure 2.8** Thermal properties and chemical bonding of HyA hydrogels with low-to-high crosslinking densities. (a) Mass (%) of HyA\_L, HyA\_M, HyA\_H, and HyA as the temperature increased in the TGA testing. (b) DSC curves of HyA\_L, HyA\_M, HyA\_H, and HyA. (c) FTIR-ATR spectra of HyA\_L, HyA\_M, HyA\_H, and HyA. .... 33

**Figure 2.9** Mechanical and rheological properties of HyA hydrogels with low-to-high crosslinking densities. (a,b) The photographs of elongation for (a) HyA\_M and (b) HyA\_H during the tensile testing. (c) The representative stress-strain curves of HyA\_M and HyA\_H. (d) Tensile strength of HyA\_M and HyA\_H. (e) Tensile modulus of HyA\_M and HyA\_H. (f) Elongation of HyA\_M and HyA\_H at break in the tensile testing. In (c-f), the data for HyA\_M are in orange color on the left axis, and the data for HyA\_H are in red on the right axis. In (d-f), the data are shown as mean ± standard deviation (n=3). (g) The curves of storage modulus (G') and loss modulus (G'') over shear strain for HyA\_L (yellow) and HyA (black) according to the rheological testing. (h) The viscosity over shear rate for HyA\_L (yellow) and HyA (black). .... 36

**Figure 2.10** Tensile testing results of HyA\_H at different strain rates. (a) Representative stress-strain curves from the tensile testing of HyA\_H at different strain rates of 10 mm/min, 20 mm/min, and 30 mm/min. (b) Tensile strength of HyA\_H at different strain rates of 10 mm/min, 20 mm/min, and 30 mm/min. (c) Tensile modulus of HyA\_H at different strain rates of 10 mm/min, 20 mm/min, and 30 mm/min. (d) Elongation at break of HyA\_H at different strain rates of 10 mm/min, 20 mm/min, and 30 mm/min. Data in (b, c, d) are shown as mean  $\pm$  standard deviation (n=3). ..... 37

**Figure 3.1** The conditions required for three-dimensional printing (3DP) of crosslinked HyA gels. (a) Illustration showing thermodynamic and kinetic factors determine the coordination states of HyA hydrogels. (b) Three coordination states of HyA hydrogels. (c) Boundary conditions of FeCl<sub>3</sub> concentrations and pH values for HyA gel to be printable. The green region indicates the conditions with feasible FeCl<sub>3</sub> concentration and pH value for achieving printability of crosslinked HyA gels. (d) The curves of storage modulus ( $G'$ ) and loss modulus ( $G''$ ) over shear strain for the HyA hydrogels crosslinked in 300 mM FeCl<sub>3</sub> solution for the reaction time of 5-120 min and non-crosslinked HyA. (e) The viscosity of the crosslinked HyA hydrogels and non-crosslinked HyA in (b). In (b,c), red square, green circle, pink diamond, and brown triangle indicate the reaction time of 5, 15, 30, and 120 min, respectively; and the black star indicates non-crosslinked HyA solution as a control. .... 49

**Figure 3.2** Structural stability of (a) the printable gel (HyA\_P) with a crosslinking density between HyA\_L and HyA\_M over a period of 20 minutes, in contrast to the rapid structural change of (b) the HyA control over 15 seconds, after they were printed or injected onto the surface of a petri dish. .... 50

**Figure 3.3** Illustration showing two type of 3D printing method. (a) Illustration of the cold-stage method for 3DP of printable HyA hydrogels (named as HyA\_P), in which the HyA\_P was printed on a cold stage followed by immersing in DI water. (b) Illustration of the direct writing method for 3DP of HyA\_P, in which the HyA\_P was directly printed in DI water at room temperature. .... 52

**Figure 3.4** Structural stability of 3D printed constructs. (a, b) Top and bottom view of HyA hydrogels printed by (a) the cold-stage method and (b) direct writing method. (c) Cross-section view of the filament printed using the cold-stage method and direct writing method, and their respective aspect ratios post-printing. The aspect ratio is height/width (AR=H/W). Data are mean  $\pm$  standard deviation (n=5). .... 54

**Figure 4.1** Schematic diagrams showing direct writing of HyA solution in FeCl<sub>3</sub> solution. (a) Crosslinking and phase transition of HyA hydrogels crosslinked using FeCl<sub>3</sub> solution at different concentrations. (b) Procedures of directly writing HyA solution in FeCl<sub>3</sub> solution. .... 64

**Figure 4.2** Photograph showing HyA filaments prepared by direct writing of HyA solution in the FeCl<sub>3</sub> solution. .... 65

**Figure 4.3** Rheological properties of HyA solution at different HCl concentrations. (a-b) Storage ( $G'$ ) and loss modulus ( $G''$ ) (a) and the ratio of  $G'/G''$  (b) of HyA solution at different frequencies. (c-d)  $G'$  and  $G''$  (c) and the ratio of  $G'/G''$  (d) of HyA solution at different shear strains. (e) The viscosity of HyA solution at different shear rates. .... 67

**Figure 4.4** Rheological properties of HyA solution at different  $\text{CaCl}_2$  concentrations. (a-b) Storage ( $G'$ ) and loss modulus ( $G''$ ) (a) and the ratio of  $G'/G''$  (b) of HyA solution at different frequencies. (c-d)  $G'$  and  $G''$  (c) and the ratio of  $G'/G''$  (d) of HyA solution at different shear strains. (e) The viscosity of HyA solution at different shear rates. .... 68

**Figure 4.5** Rheological properties of HyA solution at different HCl and  $\text{CaCl}_2$  concentrations. (a-b) Storage ( $G'$ ) and loss modulus ( $G''$ ) (a) and the ratio of  $G'/G''$  (b) of HyA solution at the different frequencies. (c-d)  $G'$  and  $G''$  (c) and the ratio of  $G'/G''$  (d) of HyA solution at different shear strains. (e) The viscosity of HyA solution at different shear rates. .... 69

**Figure 4.6** FTIR-ATR spectra of HyA solution preloaded with different cations. .... 70

**Figure 4.7** Determination of direct writing capability of HyA solution preloaded with cations. (a) Illustration showing the direct writing of HyA filaments in  $\text{FeCl}_3$  solution. (b) Photographs showing the status of crossed filaments. (c) Status of the crossed filaments. .... 71

**Figure 4.8** Determination of  $\text{FeCl}_3$  concentration and minimum reaction time. (a) Cross-sectional SEM images of HyA filaments crosslinked using  $\text{FeCl}_3$  solution at concentrations of 10-40 mM. (b) Cross-sectional SEM images of HyA filaments crosslinked using  $\text{FeCl}_3$  solution at concentrations of 50-300 mM for different reaction times. .... 73

**Figure 4.9** Photographs showing the status of HyA filaments crosslinked using  $\text{FeCl}_3$  solution at the concentrations of 50-300 mM for different reaction times. .... 74

**Figure 4.10** Reaction time in the secondary crosslinking of HyA hydrogels. (a) The minimum reaction time of obtaining fully crosslinked HyA filaments using  $\text{FeCl}_3$  solution at the concentrations of 50-300 mM. (e) The maximum reaction time of retaining solid HyA filaments using  $\text{FeCl}_3$  solution at concentrations of 50-300 mM. .... 74

**Figure 4.11** Optical images showing the change of HyA hydrogels immersed in water with different pH values. .... 75

**Figure 4.12** Procedures of Direct writing of HyA solution in  $\text{FeCl}_3$  solution and the optical images of printed HyA hydrogels. .... 76

**Figure 4.13** 3D printing resolution enhancement via volume shrinkage. (a) Photographs showing the volume shrinkage of HyA hydrogels prepared using different concentrations

of HyA solution. (b) Photographs showing the volume shrinkage of HyA hydrogels crosslinked using different FeCl<sub>3</sub> concentrations. (c) Quantitative volume shrinkage of HyA hydrogels prepared using different concentrations of HyA solution. (d) Quantitative volume shrinkage of HyA hydrogels crosslinked using different FeCl<sub>3</sub> concentrations. 77

**Figure 5.1** Illustration showing three different cell culture methods to evaluate the cytocompatibility of biodegradable materials..... 81

**Figure 5.2** Representative fluorescence images of BMSCs directly in contact with the samples (direct contact) and on the culture plate surrounding each corresponding sample (indirect contact) after a 24-hour culture. Scale bar =100 μm for all images. .... 92

**Figure 5.3** Optical image of the cells adhered on the culture plate before adding any samples, that is, the cells at time zero (T=0)..... 93

**Figure 5.4** Representative optical images of BMSCs directly in contact with the samples (direct contact) and cells on the culture plate surrounding each corresponding sample (indirect contact) after 24-hour direct exposure culture. Scale bar =100 μm for all images. .... 94

**Figure 5.5** BMSC adhesion densities under direct and indirect contact conditions in the groups of HyA\_H\_3D, HyA\_H, HyA\_M, HyA\_P, HyA\_L, and Glass, and in the control groups of Fe@2.09 mM, Fe@6.08 mM, HyA, and Cell. Data are shown as mean ± standard deviation (n=3); \*p<0.05, \*\*p<0.01, \*\*\*p<0.001. .... 95

**Figure 5.6** Photographs of the samples in the culture media before (T=0) and after (T=24) the prescribed 24-h incubation. The dashed circles indicate the samples in the media. The brightness and contrast of the images were adjusted to highlight the samples in the media. Scale bar=5 mm for all images..... 96

**Figure 5.7** Photographs of the collected media containing visible degradation products from the samples. Dashed circles are used to indicate the degradation products. Scale bar=5 mm for all images. .... 97

**Figure 5.8** The media analysis for HyA degradation and associated changes in the BMSC culture. (a) The pH values of media when the samples were added (T=0 h). (b) The pH values of media after 24 hours of culture with the samples (T=24 h). (c, d) The concentrations of Fe<sup>3+</sup> and Ca<sup>2+</sup> ions in the media at T=24 h. Data are shown as mean ± standard deviation (n=3); \*p<0.05, \*\*p<0.01, \*\*\*p<0.001. .... 99

**Figure 5.9** Representative fluorescence images of BMSCs cultured with HyA hydrogels crosslinked via direct writing of HyA solution in FeCl<sub>3</sub> solution after a 24-hour direct exposure culture. Scale bar =100 μm for all images..... 100

<b>Figure 5.10</b> Cytocompatibility of HyA hydrogels printed via direct writing. (a) Quantitative BMSC adhesion density in different experimental and control groups. (b) pH value of post-culture media. (c) Iron ion concentration of post-culture media. (d) Ca <sup>2+</sup> concentration of post-culture media.....	102
<b>Figure 6.1</b> Illustration showing procedures of incorporating MNPs in HyA hydrogels in situ.....	115
<b>Figure 6.2</b> Microstructure and elemental composition of the cross-sections of lyophilized magnetic hydrogels. ....	122
<b>Figure 6.3</b> Photographs showing the responses of magnetic hydrogels to a magnet. ....	123
<b>Figure 6.4</b> Thermal properties and crystal structure of magnetic hydrogels. (a) Mass-temperature curves of magnetic hydrogels. (b) XRD spectra of magnetic hydrogels. ....	125
<b>Figure 6.5</b> Representative fluorescence images of BMSCs cultured with magnetic hydrogels after a 24-hour direct exposure culture. ....	126
<b>Figure 6.6</b> Quantitative cell adhesion density of BMSCs cultured with magnetic hydrogels after a 24-hour direct exposure culture. ....	127
<b>Figure 6.7</b> Photographs showing the status of hydrogels after a 24-hour direct exposure culture. ....	129
<b>Figure 6.8</b> Post-culture analysis of media. (a) pH value. (b) Fe <sup>3+</sup> concentration. (c) Ca <sup>2+</sup> concentration in the post-culture media after a 24-hour direct exposure culture. ....	129

## **CHAPTER 1 Background on the Crosslinking and Three-Dimensional Printing of Hyaluronic Acid Hydrogels for Biomedical Applications**

Hydrogels are three-dimensional (3D) crosslinked polymeric networks that can maintain high water content in their structures and can be created from both synthetic and natural polymers.<sup>1</sup> Hyaluronic acid (HyA) is a hydrophilic polysaccharide that naturally presents in the human body and plays a critical role in the biological functions of many different tissues and organs.<sup>2-3</sup> The aqueous solution of HyA with a concentration greater than 0.1 mg/mL is viscoelastic because of the entanglement of its molecular chains.<sup>4</sup> The entangled molecular networks of HyA still retain flowability before crosslinking.<sup>4</sup> The crosslinking of HyA can be achieved via interactions between its carboxyl groups and cations such as Fe<sup>3+</sup> ions,<sup>5-6</sup> blending with other polymers,<sup>7-8</sup> or modification with other functional groups.<sup>9-13</sup> These three types of methods for crosslinking HyA have been explored for a variety of biomedical applications, such as tissue repair,<sup>14-17</sup> drug delivery,<sup>18-19</sup> cell encapsulation,<sup>20-21</sup> and biosensing.<sup>22-23</sup> For example, HyA hydrogel crosslinked via carboxylate-Fe<sup>3+</sup> coordination has been clinically used as an adhesion barrier gel, commercially called Intergel<sup>®</sup>, for preventing peritoneal adhesion after surgeries such as laparotomy.<sup>5, 16, 24</sup> Blending HyA with other polymers could also produce crosslinked hydrogels. For example, when the oxidized HyA (aldehyde HyA) was blended with N-succinyl-chitosan, the gelation was achieved via the Schiff base reaction between aldehyde groups on the oxidized HyA and amino groups from the N-succinyl-chitosan.<sup>7</sup> Lastly, HyA can be chemically modified to form HyA derivatives by

adding new functional groups, and these HyA derivatives can be crosslinked with or without adding crosslinking initiator, as shown in Figure 1.1. For example, iminodiacetic acids (IDA)-modified HyA relied on the addition of cations to achieve the crosslinking via metal-ligand coordination.<sup>13</sup> The methacrylate-modified HyA (MeHyA) was crosslinked under ultraviolet (UV) irradiation with the addition of a photoinitiator.<sup>12</sup> The thiol-modified HyA molecules were crosslinked by oxidation of thiols to disulfides in the air without an initiator.<sup>10</sup> The crosslinking density of these HyA hydrogels can be tuned by adjusting the parameters such as the molecular weight and concentration of HyA,<sup>25</sup> the types and concentrations of crosslinkers,<sup>26-27</sup> the ratios of HyA to the co-blended polymers,<sup>7</sup> the percentage of modified functional groups,<sup>9</sup> as well as the conditions of chemical reactions.<sup>2, 28-29</sup> The tunable crosslinking densities have been achieved using the methods of functionalizing HyA<sup>9</sup> or blending HyA with other polymers,<sup>26</sup> but the reversibility of the crosslinked HyA hydrogels has not been demonstrated and some crosslinked hydrogels such as UV-crosslinked MeHyA are not reversible.

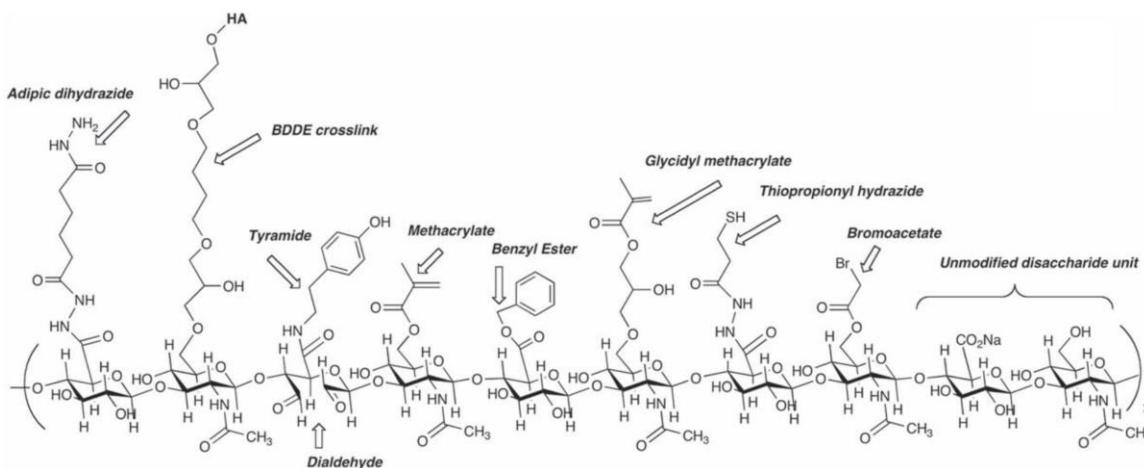


**Figure 1.1** Functionalization strategies of HyA molecule. This figure is adapted from<sup>2</sup>.

Reversible crosslinking is critical for hydrogels to achieve self-healing capability that allows recovery of their original structure,<sup>30</sup> mechanical properties,<sup>31-34</sup> and electrical properties<sup>31-32</sup> after the fracture. Self-healing hydrogel is favorable for many applications, e.g. repairing tissues that undergo cyclic loading such as heart muscle.<sup>35-36</sup> Reversible crosslinking of HyA hydrogels has been achieved via reactions such as guest-host interaction<sup>37-38</sup> and dynamic ligand-metallic ion coordination.<sup>28, 39-40</sup> For instance, adamantane (Ad) modified and cyclodextrin (CD) modified HyA (named as Ad-HyA and CD-HyA) was crosslinked via Ad-CD guest-host interaction to form a self-healing hydrogel,<sup>37-38</sup> and bisphosphonate (BP) modified HyA was crosslinked by  $\text{Ca}^{2+}$  to form the reversible BP- $\text{Ca}^{2+}$  crosslinking.<sup>28</sup> The reversible phase transition of catechol modified HyA hydrogels has been achieved via controlling catechol- $\text{Fe}^{3+}$  coordination by adding HCl or NaOH.<sup>39-40</sup>

Three-dimensional (3D) network structures of hydrogels are highly desirable for a wide range of applications. To achieve controllable 3D microstructures and properties, it is critical to create 3D printable hydrogels. HyA has achieved 3DP capability when blended with other polymers as reported in various studies.<sup>20-21</sup> For example, alginate/HyA hydrogels at a weight ratio of 10:1 were successfully 3D printed into a crosslinking solution containing 100 mM  $\text{Ca}^{2+}$  ions, 25 mM HEPES buffer, 0.1 w/v% PEI, and 0.95% w/v% Poly (vinyl alcohol) (PVA).<sup>20</sup> Alternative methods without blending with other polymers, such as Ad-CD guest-host interaction,<sup>37-38</sup> BP- $\text{Ca}^{2+}$  coordination,<sup>28</sup> and photocrosslinking,<sup>12</sup> have also shown success in 3DP of HyA hydrogels. However, all these HyA hydrogels required certain chemical modifications

such as blending with other polymers or adding functional groups to achieve 3D printing (3DP), which may raise additional concerns on their interactions with host cells and biocompatibility for medical applications, especially when the regulatory approval is required for clinical translation of the final products.<sup>2, 41-42</sup> Moreover, blending with other polymers increases the chemical complexity,<sup>7</sup> while the addition of new functional groups raises the safety concern on undesirable solvent residue.<sup>37</sup> The chemically modified HyA hydrogels in literature have demonstrated some aspects of tunable crosslinking, reversible phase transition, and 3DP,<sup>28, 37-39</sup> but not all. Thus, it is highly desirable to develop a new approach that could eliminate the need for chemical modifications of HyA such as blending with other polymers or adding functional groups, while achieving tunable crosslinking density, reversible phase transition, and 3DP capability of hydrogels, all in one.

## **CHAPTER 2 Tunable Crosslinking and Reversible Phase Transition of Hyaluronic Acid Hydrogels via Dynamic Coordination of Carboxyl Groups and Metallic Ions**

### **2.1 Introduction**

In this chapter, I will elucidate the relationships of key parameters in controlling the dynamic coordination of  $\text{Fe}^{3+}$  ions with the innate carboxyl groups on HyA chains, and reveal how we can use such principles to achieve tunable crosslinking and reversible phase transition of HyA hydrogels. Although the interactions between carboxyl groups and cations such as  $\text{Fe}^{3+}$  ions have been explored before,<sup>5-6</sup> this study made several key advancements. For the first time, this chapter revealed the effects of  $\text{Fe}^{3+}$  and  $\text{H}^+$  concentrations and reaction time on the ratios of mono-, bi-, and tridentate coordination bonding, and described the mathematical equations governing the low-to-high tunable crosslinking densities of the hydrogels and reversible solid-liquid phase transition. The mechanism and principle for dynamic carboxylate- $\text{Fe}^{3+}$  ion coordination is applicable for crosslinking of other polymer hydrogels with carboxyl groups.

## **2.2 Materials and Methods**

### **2.2.1 Determine the Effects of Fe<sup>3+</sup> Concentration and pH Value on the Crosslinking Densities and Reversible Phase Transition of HyA Hydrogels**

#### *2.2.1.1 Determine the Effects of Fe<sup>3+</sup> Concentration on the Crosslinking Densities and Reversible Phase Transition of HyA Hydrogels*

Sodium hyaluronate (abbreviated as HyA; Bulk Supplements, Henderson, NV) solution at the concentration of 5 w/v% was manually printed onto a 6-well plate to create a 24×24 mm network pattern with 16 squares of 6×6 mm. The 24×24 mm network pattern was first drawn on a piece of paper that was placed under the transparent well plates to serve as a guide during the printing. A syringe with a needle size of 0.35 mm was utilized for printing. After creating the HyA network pattern, 10 mL of Fe<sup>3+</sup> solution (FeCl<sub>3</sub>, #169430010, Sigma-Aldrich, St. Louis, MO) at the concentrations of 2 mM, 3 mM, 5 mM, 10 mM, 20 mM, 30 mM, 50 mM, 100 mM, and 300 mM was added in different wells to crosslink the HyA, respectively. After 24-hour immersion, the crosslinking states of respective HyA gels were photographed.

#### *2.2.1.2 Determine the Effects of pH Value on the Crosslinking Densities and Reversible Phase Transition of HyA Hydrogels*

FeCl<sub>3</sub> solution at the concentrations of 10 mM, 20 mM, and 30 mM was prepared. The FeCl<sub>3</sub> solution at 10 mM, 20 mM, and 30 mM was adjusted to the respective pH range of 2.1~2.4, 2.05~2.3, and 2~2.2, respectively using hydrochloric acid (HCl). HyA network patterns were created in a 6-well plate as described above, 10 mL of FeCl<sub>3</sub>

solution at 10mM, 20mM, and 30mM was then added to the respective wells. After 24-hour immersion, the crosslinking states of HyA gels were photographed.

### *2.2.1.3 Determine the Effects of $Fe^{3+}$ Concentration and pH Value on the Storage*

#### *Modulus of Crosslinked HyA Gels*

To investigate the effects of  $Fe^{3+}$  concentration on the storage modulus of crosslinked HyA gels, we prepared  $FeCl_3$  solution at the concentrations of 10 mM, 20 mM, and 30 mM, and the pH value of these solutions was intentionally adjusted to 1.7 using HCl. HyA solution at the concentration of 5 w/v% was injected into the respective  $FeCl_3$  solutions of 10, 20, and 30 mM using a syringe with a needle of 0.35 mm in diameter. At the respective time points of 5 min, 15 min, and 30 min, the crosslinked HyA gels were collected using a spoon and tested for storage moduli using a rheometer (MCR 92 with PP25 measuring system, Anton Paar), respectively. For rheological testing, around 1 mL of each collected gel sample was added onto the stage of the rheometer, and then the testing spindle (PP25, Anton Paar) was moved down and the extra gel sample was removed. The gap between the bottom plane of the spindle and stage was set as 1 mm. The strain angular frequency was set as 10 1/s for all the samples, and the storage modulus of the sample at the shear strain of 1%~1000% (or shear strain of 0.01-10) was recorded at 25 °C.

To investigate the effects of pH value on storage modulus of crosslinked HyA gels, we prepared  $FeCl_3$  solution at the concentration of 20 mM and intentionally adjusted its pH value to 1.5, 1.7, and 1.9 using HCl, respectively. HyA solution at the concentration of 5 w/v% was injected into the 20mM  $FeCl_3$  solutions with respective pH

of 1.5, 1.7, and 1.9 following the same method described above. The crosslinked HyA gel was collected and tested for storage modulus using the same rheometer setup.

### **2.2.2 Demonstrate the Tunable Crosslinking and Reversible Phase Transition of HyA Hydrogels**

Based on the different crosslinking degree (or coordination states), the crosslinked HyA gels are classified as HyA hydrogel with low (HyA\_L), medium (HyA\_M), and high (HyA\_H) crosslinking degree.

Demonstrate the phase transition from HyA\_M to HyA\_L: For this, 8 mL sodium hyaluronate (abbreviated as HyA; Bulk Supplements, Henderson, NV) solution at the concentration of 5 w/v% was injected into a PTFE mold (Bottom size: 4×8 cm) using a syringe with a needle of 0.84 mm in diameter. It took 10 min for the viscous HyA solution to form a uniform HyA layer with a thickness of 0.25 mm on the bottom of the mold. After that, 32 mL of FeCl<sub>3</sub> (#169430010, Sigma-Aldrich, St. Louis, MO) solution at the concentration of 300 mM was added into the mold to crosslink the HyA. The crosslinking degree of HyA can be controlled by the reaction time with FeCl<sub>3</sub> solution. When the reaction time was 5 min, HyA\_M formed. When the reaction time was 1 hour, HyA\_L formed.

Demonstrate the phase transition from HyA\_M to HyA\_H and HyA\_L to HyA\_H: To obtain HyA\_H, the as-prepared HyA\_M or HyA\_L was immersed in DI water in a beaker for 24 hours at room temperature and pressure. DI water was refreshed every 12 hours.

Demonstrate the phase transition from HyA\_L to HyA\_M: HyA\_L is injectable and can be used to directly write letters or patterns. To obtain HyA\_M, HyA\_L was first injected onto a plastic weighing dish using a syringe with a needle of 0.84mm in diameter to form a 1mm-thin layer of the hydrogel, and then 20 mL FeCl<sub>3</sub> solution at the concentration of 30 mM was added on top of the HyA\_L to completely cover the HyA\_L layer. HyA\_M formed after HyA\_L reacted with 30 mM FeCl<sub>3</sub> solution for 5 mins at room temperature and pressure.

Demonstrate phase transition from HyA\_H to HyA\_M and HyA\_M to HyA\_L: When HyA\_H was immersed in 300 mM FeCl<sub>3</sub> solution in a plastic weighing dish for 1 hour, HyA\_H transformed to HyA\_M. When HyA\_H was immersed in 300 mM Fe Cl<sub>3</sub> solution in a plastic weighing dish for 2 hours, HyA\_H transformed to HyA\_L. The collected HyA\_L can be injected or printed to form a line, letters, or patterns using a syringe with a needle of 0.84 mm in diameter.

All the processes described above were recorded in both videos and photographs using a camera.

### **2.2.3 Measure the Reduction of Size, Volume, and Water Content and the Release of Fe<sup>3+</sup> Ions During the Phase Transition From HyA\_M to HyA\_H**

HyA\_M with a diameter of 13 mm and a thickness of 2 mm was immersed in the DI water for up to 96 hours at room temperature and pressure. After immersed in DI water for 0.25 h, 0.5 h, 1 h, 1.5 h, 2.5 h, 4 h, 12 h, and 24 h, 36 h, 48 h, and 96 h, the gels were collected from the DI water using a tweezer and were then photographed respectively. The diameter of the sample was measured before and after immersion in DI

water for a prescribed period, based on the scale bar in each photograph using the tools in ImageJ software. The mass and buoyant mass of the sample was measured before and after immersion in DI water for a prescribed period using the analytical balance (ME-T, Meter Toledo) and buoyant balance (analytical balance equipped with a density Kit, XPR-S, Meter Toledo). The volume ( $v$ ) of the hydrogel before and after immersion in DI water for a prescribed period was calculated as:

$$v = \frac{m_1 - m_2}{\rho} \quad (2.1)$$

Where  $v$  is the volume of the hydrogel at a specific timepoint,  $m_1$  and  $m_2$  are the mass and buoyant mass of the hydrogel at a specific time point, and  $\rho$  is the density of water (i.e. 1 g/cm<sup>3</sup>).

The volume change ratio at a specific time point was calculated as:

$$\text{Volume change ratio} = \frac{v}{v_0} \quad (2.2)$$

Where  $v$  is the volume of the hydrogel at that specific time point, and  $v_0$  is the volume of hydrogel before immersion in DI water.

After being immersed in DI water for 96 h, the crosslinked HyA hydrogel was lyophilized using a lyophilizer (FreeZone Benchtop Freeze Dryer, Labconco) at the temperature of -54 oC and the pressure of 0.01 mBar. The water content in the sample at a specific time point was calculated as:

$$\text{Water content} = \left( \frac{m - m_0}{m} \right) \times 100\% \quad (2.3)$$

Where  $m$  is the wet mass of the hydrogel at the prescribed time point, and  $m_0$  is the sample dry mass. The sample wet mass was measured after the gel was collected from

the DI water and dried by a gentle wipe. The sample dry mass reached a constant after lyophilization and was then weighed as  $m_0$ . The water content describes the mass percentage of water in the wet swelling hydrogel.

The  $Fe^{3+}$  ion release during the phase transition from HyA\_M to HyA\_H in DI water was measured using inductively coupled plasma-optical emission spectrometry (ICP-OES; Optima 8000, PerkinElmer, Waltham, MA). Specifically, HyA\_M with a diameter of 13 mm and a thickness of 2 mm was immersed in 50 mL DI water in a 50 mL tube at room temperature and pressure. At the time points of 0 h, 0.25 h, 0.5 h, 1 h, 1.5 h, 2.5 h, 4 h, 12 h, 24 h, 36 h, 48 h, and 96 h, the immersion solution of 0.1 mL was collected from the tube at each time point and was diluted with a factor of 1:100 using DI water (Millipore). The diluted solution was loaded onto the autosampler for ICP-OES. The  $Fe^{3+}$  concentration in the immersion solution was calculated based on the curves of  $Fe^{3+}$  standards at the respective concentrations of 0.1, 0.5, 1.0 mg/L, which was prepared by dissolving  $FeCl_3$  in DI water. The cumulative amount of  $Fe^{3+}$  ion released from HyA hydrogel into the DI water at each time point was calculated using the following equation:

$$Fe^{3+} \text{ ions released} = c \times v \quad (2.4)$$

Where  $c$  is the  $Fe^{3+}$  concentration in the immersion solution measured using ICP-OES, and  $v$  is the volume of the total immersion solution.

The measurements were performed in triplicate samples for the diameter and volume of hydrogels, water content in the hydrogels, and  $Fe^{3+}$  ion release from the hydrogels.

## **2.2.4 Characterize Microstructure and Properties of the HyA\_L, HyA\_M, HyA\_H, and HyA**

### *2.2.4.1 Characterize the Microstructure and the Porosity of HyA\_M, HyA\_H, and HyA*

HyA\_M, HyA\_H, and 5 w/v% HyA solution were lyophilized using a lyophilizer (FreeZone Benchtop Freeze Dryer, Labconco) at the temperature of -54 °C and the pressure of 0.01 mBar, the same as described in Section 2.3. The lyophilized samples were then cut into half and mounted onto a 90° SEM sample holder, the cross-sections were sputter-coated (model 108, Cressington Scientific Instruments Ltd., Watford, U.K.) with platinum/palladium at 20 mA with a 90 s sputter time. The microstructures of the cross-sections of lyophilized HyA\_M, HyA\_H, and HyA were characterized using an Everhart–Thornley detector (ETD) of scanning electronic microscopy (SEM, Nova NanoSEM 450, FEI Co) with an accelerating voltage of 5 kV and a spot size of 3, at the magnification of 1000× and 10000×. Elemental compositions of the cross-sections of the lyophilized HyA\_M and HyA\_H were characterized using a detector for energy dispersive X-ray spectroscopy (EDS; X-Max 50 silicon drift detector) attached to SEM with an accelerating voltage of 10 kV and a spot size of 3, at the magnification of 10000×. Aztec Energy software (Oxford Instruments, Abingdon, Oxfordshire, U.K.) were used to analyze the elemental composition and distribution. The porosity of HyA\_M, HyA\_H, and HyA was determined in the SEM images using the image analysis tools in ImageJ software.

#### *2.2.4.2 Characterize the Thermal Properties of HyA\_L, HyA\_M, HyA\_H, and HyA*

The HyA samples of interest were analyzed using a thermogravimetric analyzer (TGA; TG 209 F1 Libra®, Netzsch) and a differential scanning calorimeter (DSC 214, Netzsch) for thermal properties. Before the TGA and DSC testing, all the samples were lyophilized using the same method as described in Sections 2.3 and 2.4.1. For TGA, the lyophilized HyA\_L, HyA\_M, HyA\_H, and HyA sample of 10 mg each were placed in alumina crucibles and heated from 30 °C to 800 °C at a heating rate of 10 °C /min in a nitrogen (N<sub>2</sub>) atmosphere with a N<sub>2</sub> flow rate of 20 mL/min. The sample mass change over the temperature was analyzed and plotted. For DSC measurements, the lyophilized HyA\_L, HyA\_M, HyA\_H, and HyA samples of 5 mg each were placed in aluminum containers and an empty container was used as a reference. The samples were heated from 0 °C to 120 °C, then cooled to 0 °C, and reheated to 350 °C. The heating and cooling rates were set as 10 °C /min and the test was performed in a N<sub>2</sub> atmosphere with a N<sub>2</sub> flow rate of 10 mL/min.

#### *2.2.4.3 Characterize the Chemical Bonding of HyA\_L, HyA\_M, HyA\_H, and HyA*

Fourier transform infrared spectroscopy-attenuated total reflection (FTIR-ATR, Nicolet iS10, ThermoFisher Scientific) was used to measure the transmittance of the HyA\_L, HyA\_M, HyA\_H, and 5 w/v% HyA solution at the wavenumber of 4000-500 cm<sup>-1</sup>. Briefly, the sample was placed on the sample holder to cover the ATR crystal, and a metallic cap was then placed above the sample to prevent water evaporation. FTIR-ATR measurement was performed using the absorbance mode with 64 scans. After the measurement for each sample, the sample holder and the metallic cap were cleaned using

DI water and then dried using a cotton swab to avoid cross-contamination between the samples.

#### *2.2.4.4 Perform the Tensile Testing for HyA\_M and HyA\_H*

The tensile properties of HyA\_M and HyA\_H samples were tested using an Instron 5969 dual column testing system equipped with a 10 N load cell (Instron, Norwood, MA). The HyA\_M sample was cut into a dimension of 50×10×2 mm, and the HyA\_H sample was cut into a dimension of 20×4×0.5 mm for tensile testing. The tensile testing was performed with a 0.005 N preload and a crosshead speed of 10 mm/min. The tensile stress-strain curves were plotted from the data calculated based on the load and extension. The tensile strength was defined as the maximum stress before failure in the stress-strain curve of the respective hydrogel sample. The tensile modulus was determined from the linear region of the stress-strain curve by fitting a straight line between 0% and 20% strain. The percent of sample elongation at the breakage point was also calculated.

#### *2.2.4.5 Measure the Dynamic Modulus and Viscosity of HyA\_L and HyA*

The rheological properties of HyA\_L and HyA (5 w/v%) were determined using a rheometer (MCR 92 with PP25 measuring system, Anton Paar). For this purpose, the HyA\_L was prepared by injecting 5 w/v% HyA solution to 300 mM FeCl<sub>3</sub> solution using a syringe with a needle size of 0.35 mm and reacted for 4 h. The storage modulus and loss modulus of the sample at the shear strain of 1%~1000% (or shear strain of 0.01-10) was recorded at 25 °C, similarly as described above. For viscosity measurement, the gap

between the bottom plane of the spindle and stage was set as 1 mm, and the viscosity of the sample at the shear rate of 0.1 1/s~100 1/s was recorded at 25 °C.

## 2.3 Results

### 2.3.1 Tunable Ratios of Mono-, Bi- and Tridentate Coordination in HyA Determine the Low-to-High Crosslinking Densities and Solid-Liquid Reversibility of Hydrogels

It is well known that the ferric iron ( $\text{Fe}^{3+}$ ) solution such as iron chloride ( $\text{FeCl}_3$ ) solution is inherently acidic because the electrons between the O-H bond of the water in this solution become polarized until an  $\text{H}^+$  ion from water is liberated.<sup>43</sup> Our results indeed confirmed that the innate pH value of  $\text{FeCl}_3$  solution (i.e.,  $\text{FeCl}_3$  solution dissolved in DI water without pH adjustment) decreases as  $\text{Fe}^{3+}$  concentration increases; specifically, the innate pH of  $\text{FeCl}_3$  solution showed a negative linear relationship with the logarithmic form of  $\text{Fe}^{3+}$  concentration, as shown in Figure 2.1.

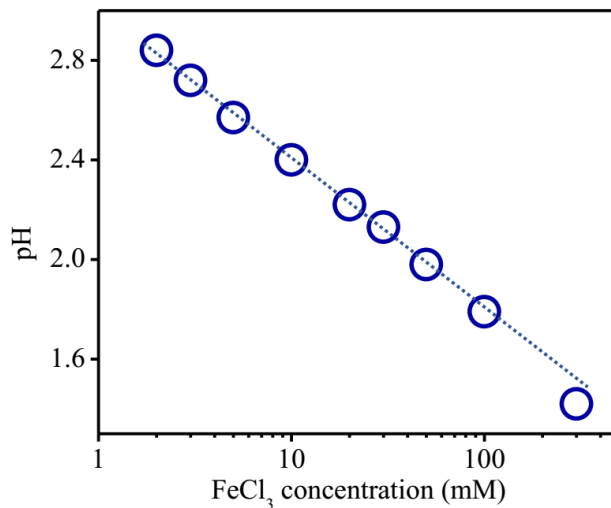


**Figure 2.1** The innate pH values of  $\text{FeCl}_3$  solutions at different concentrations.

Figure 2.2a shows the chemical structure of sodium hyaluronate, which is the salt form of HyA with one carboxyl group per disaccharide unit. When a FeCl<sub>3</sub> solution is added to the sodium hyaluronate, three different coordination of mono-, bi- and tridentate coordination of carboxyl groups with Fe<sup>3+</sup> ions on HyA molecular chains could form, as shown in Figure 2.2a. In addition to the Fe<sup>3+</sup> ions and their complex (e.g., [Fe(H<sub>2</sub>O)<sub>6</sub>]<sup>3+</sup>),<sup>44</sup> the iron salt solution has abundant hydrogen ions (H<sup>+</sup>), thus forming an acidic solution. As a result, the coordination sites of carboxyl groups in HyA can also be occupied by H<sup>+</sup> ions due to the acidic nature of Fe<sup>3+</sup> solution. Thermodynamically, both Fe<sup>3+</sup> and H<sup>+</sup> (pH) ion concentrations determine the tunable ratios of mono-, bi-, and tridentate coordination states and the resulted low-to-high crosslinking densities of Fe<sup>3+</sup> crosslinked HyA hydrogels, as shown in Figure 1b. The equilibrium constant for mono (K<sub>1</sub>), bi (K<sub>2</sub>), and tridentate (K<sub>3</sub>) coordination, and H<sup>+</sup> (K<sub>4</sub>) replacement is defined below respectively:

$$K_1 = \frac{[\text{Fe}^{3+}\text{COO}^-]}{[\text{Fe}^{3+}][\text{COO}^-]} \quad (2.5)$$

$$K_2 = \frac{[\text{Fe}^{3+}(\text{COO}^-)_2]}{[\text{Fe}^{3+}][\text{COO}^-]^2} \quad (2.6)$$

$$K_3 = \frac{[\text{Fe}^{3+}(\text{COO}^-)_3]}{[\text{Fe}^{3+}][\text{COO}^-]^3} \quad (2.7)$$

$$K_4 = \frac{[\text{H}^+\text{COO}^-]}{[\text{H}^+][\text{COO}^-]} \quad (2.8)$$

Equation (2.5a-2.8a) below are derived from Equation (2.5-2.8) to show the ratio of bonded to free carboxyl groups.

$$\frac{[\text{Fe}^{3+}\text{COO}^-]}{[\text{COO}^-]} = [\text{Fe}^{3+}]K_1 \quad (2.5a)$$

$$\frac{[\text{Fe}^{3+}(\text{COO}^-)_2]}{[\text{COO}^-]^2} = [\text{Fe}^{3+}]K_2 \quad (2.6a)$$

$$\frac{[\text{Fe}^{3+}(\text{COO}^-)_3]}{[\text{COO}^-]^3} = [\text{Fe}^{3+}]K_3 \quad (2.7a)$$

$$\frac{[\text{H}^+\text{COO}^-]}{[\text{COO}^-]} = [\text{H}^+]K_4 \quad (2.8a)$$

Equation (2.5b-2.7b) are derived from Equation (2.5-2.8) to show the concentration ratio of mono, bi, and tridentate carboxylate- $\text{Fe}^{3+}$  to carboxylate- $\text{H}^+$  coordination.

$$\frac{[\text{Fe}^{3+}\text{COO}^-]}{[\text{H}^+\text{COO}^-]} = \frac{K_1}{K_4} \cdot \frac{[\text{Fe}^{3+}]}{[\text{H}^+]} \quad (2.5b)$$

$$\frac{[\text{Fe}^{3+}(\text{COO}^-)_2]}{[\text{H}^+\text{COO}^-]} = \frac{K_2}{K_4} \cdot \frac{[\text{Fe}^{3+}]}{[\text{H}^+]} \cdot [\text{COO}^-] \quad (2.6b)$$

$$\frac{[\text{Fe}^{3+}(\text{COO}^-)_3]}{[\text{H}^+\text{COO}^-]} = \frac{K_3}{K_4} \cdot \frac{[\text{Fe}^{3+}]}{[\text{H}^+]} \cdot [\text{COO}^-]^2 \quad (2.7b)$$

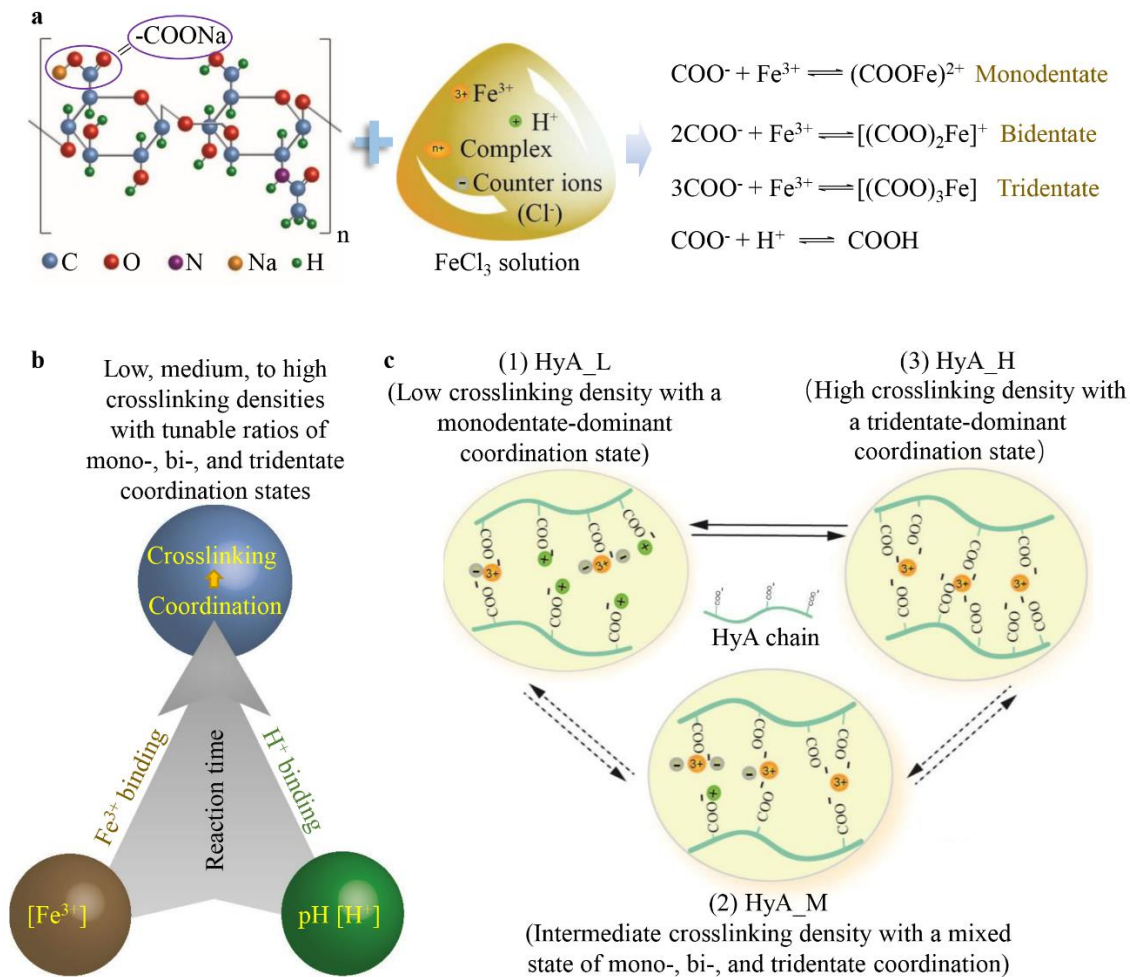


**Figure 2.2** Schematics for controlling dynamic  $\text{Fe}^{3+}$ -carboxyl coordination states and tunable crosslinking densities of HyA hydrogels. (a) Illustration for dynamic carboxylate- $\text{Fe}^{3+}$  ion coordination when sodium HyA solution is mixed with  $\text{FeCl}_3$  solution. Each disaccharide unit of HyA molecular chain has one carboxyl group. The  $\text{FeCl}_3$  solution consists of  $\text{Fe}^{3+}$  ion,  $\text{Fe}^{3+}$  complex,  $\text{H}^+$  ion, and other  $\text{Cl}^-$  counter ions.  $\text{Fe}^{3+}$  could form mono-, bi-, and tridentate coordination bonding with carboxyl groups on HyA chains, and the carboxyl groups can also bond with  $\text{H}^+$  in the acidic  $\text{FeCl}_3$  solution. (b) The key parameters of  $\text{Fe}^{3+}$  and  $\text{H}^+$  concentrations and the reaction time determine the coordination states of HyA hydrogels and the tunable crosslinking densities. (c) Illustration for the reversibility of HyA hydrogels with low-to-high crosslinking densities. (1) HyA\_L with a low degree of crosslinking has a monodentate-dominant coordination state. (2) HyA\_M with a medium degree of crosslinking has a mixed state of mono-, bi-, and tridentate coordination. (3) HyA\_H with a high crosslinking density has a tridentate-dominant coordination state. HyA\_P with the crosslinking densities between HyA\_L and HyA\_M is 3D printable.

Kinetically, however, the intermediate coordination states and the resulted crosslinking densities can also be achieved by controlling the reaction time, as illustrated in Figure 2.2b and 2.2c. When taking both thermodynamically equilibrium states and kinetically metastable states into consideration, three different coordination states with varied ratios of mono-, bi-, and tridentate coordination could form. Specifically, as shown in Figure 1c, HyA hydrogel with low crosslinking density (named as HyA\_L) could form when  $H^+$  ions replace the  $Fe^{3+}$  ions in the coordination site and  $Fe^{3+}$  ions form monodentate-dominant coordination with carboxyl groups; HyA hydrogel with high crosslinking density (named as HyA\_H) could form when  $Fe^{3+}$  ions form tridentate-dominant coordination with carboxyl groups; and HyA hydrogel with medium crosslinking density (named as HyA\_M) could form as an intermediate state by controlling the reaction time, when carboxyl groups are bonded with both  $H^+$  ions and  $Fe^{3+}$  ions to form a mixture of mono-, bi-, or tridentate coordination with carboxyl groups.

### **2.3.2 The Effects of $Fe^{3+}$ Concentration and pH Value on the Tunable Ratios of Mono-, Bi-, and Tridentate Coordination and the Resulted Low-to-High Crosslinking Densities of HyA Hydrogels**

Figure 2.3 shows the effects of  $Fe^{3+}$  ion concentrations and pH values ( $H^+$  ion concentrations) on the ratios of mono-, bi-, and tridentate carboxylate- $Fe^{3+}$  coordination and the resulted low-to-high crosslinking densities of HyA hydrogels. As shown in Figure 2.3a, we injected 5 w/v% of HyA solution onto a dish and added 2-300 mM  $FeCl_3$  solutions to react for 24 hours. The 2-300 mM  $FeCl_3$  solutions were used at their

respective innate pH values (Figure 2.1 in the supplementary materials). The HyA exhibited dramatically different structural changes in the FeCl<sub>3</sub> solutions of different concentrations. At the Fe<sup>3+</sup> concentration of less than 5 mM (2-3 mM), HyA hydrogels swelled and lost the structural integrity. At the Fe<sup>3+</sup> concentrations of 5-30 mM, HyA hydrogels crosslinked and retained their 3D structure. At the Fe<sup>3+</sup> concentration of greater than 30 mM (50-300 mM), HyA dissolved in the FeCl<sub>3</sub> solution. To demonstrate the effects of pH on HyA crosslinking, we further crosslinked the HyA utilizing 10-30 mM FeCl<sub>3</sub> solution with their pH adjusted to different values using HCl solution. As shown in Figure 2.3b, we adjusted the pH values of 10 mM, 20 mM, and 30 mM FeCl<sub>3</sub> solutions to a respective range to achieve the solid or liquid states of HyA after a reaction time of 24 hours, as highlighted using red dashes. When the pH values of 10 mM FeCl<sub>3</sub> solution were adjusted to be  $\geq 2.2$  up to the innate pH of 2.4, HyA exhibited as a solid phase. When the pH values of 10 mM FeCl<sub>3</sub> solution were adjusted to be  $\leq 2.15$ , HyA was in a liquid phase. Similarly, HyA was in a solid phase when the pH values of 20 mM FeCl<sub>3</sub> solution were adjusted to be  $\geq 2.15$  up to the innate pH of 2.22, or in a liquid phase when the pH values were adjusted to be  $\leq 2.1$ . HyA showed as a solid phase when the pH values of 30 mM FeCl<sub>3</sub> solution were adjusted to be  $\geq 2.11$  up to the innate pH of 2.13, or liquid phase when the pH values were adjusted to  $\leq 2.07$ . The results indicated that in the FeCl<sub>3</sub> solutions with higher Fe<sup>3+</sup> ion concentration, the lower pH values were required to achieve the liquid phase of HyA gel. Furthermore, we performed the rheological testing to determine the effects of Fe<sup>3+</sup> ion concentration, pH value (H<sup>+</sup> ion concentrations), and reaction time on the storage moduli of HyA hydrogels at the solid or liquid phases.

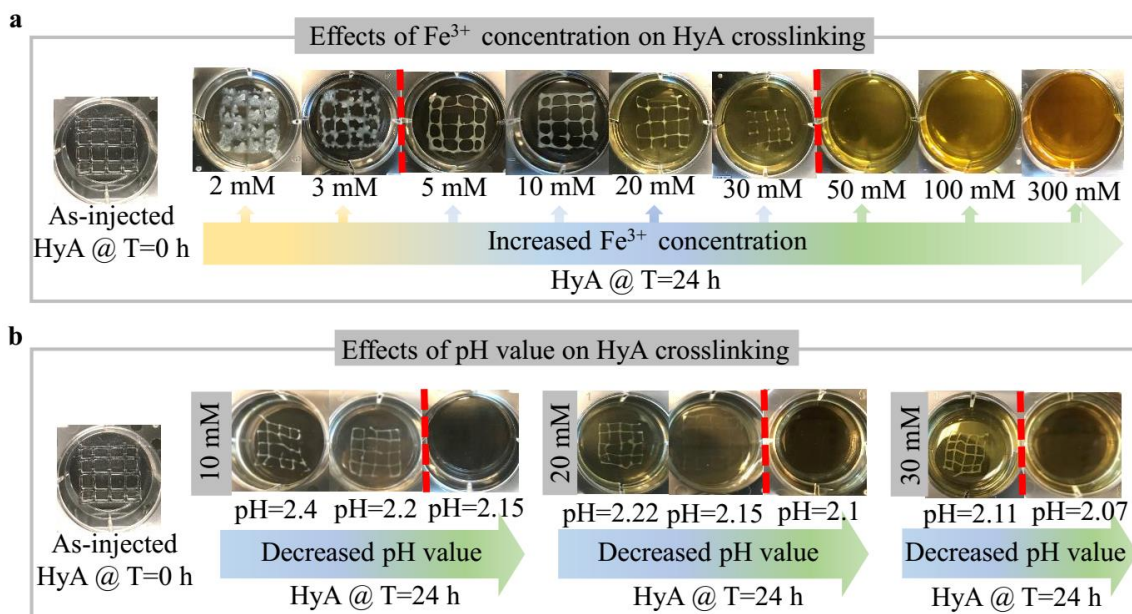


**Figure 2.3** The structural stability of crosslinked HyA hydrogels demonstrated the effects of Fe<sup>3+</sup> concentration and pH value on the tunable crosslinking of HyA hydrogels. (a) The representative photographs of as-injected (or as-printed) network pattern of HyA solution in the well at time zero (T=0 h) and HyA gels immersed in 2 to 300 mM of FeCl<sub>3</sub> solutions with innate pH values after 24 hours of reaction (T=24 h). (b) The representative photographs of as-injected (or as-printed) network pattern of HyA solution in the well at time zero (T=0 h) and HyA gels in 10 mM, 20 mM, and 30 mM FeCl<sub>3</sub> solution with decreasing pH values after 24 hours of reaction (T=24 h).

In Figure 2.4a, when the pH values of 10 mM, 20 mM, and 30 mM FeCl<sub>3</sub> solutions were adjusted to a constant of 1.7, the storage moduli of HyA hydrogels decreased as the shear strain increased, indicating the shear-thinning property of the hydrogels. Shear-thinning was also observed in HyA hydrogels formed by other metal-ligand coordination, such as HyA hydrogels crosslinked via BP-Ca<sup>2+</sup> coordination<sup>28</sup> or catechol-Fe<sup>3+</sup>.coordination.<sup>39</sup> The storage moduli of the crosslinked HyA hydrogel increased with the increase of Fe<sup>3+</sup> concentration, which was observed at all time points of 5-15 min. In Figure 2.4b, when the Fe<sup>3+</sup> concentration was fixed at 20 mM, the storage moduli of the

crosslinked HyA hydrogel decreased with decreasing pH values. In both Figure 2.4a and 2.4b, all hydrogel samples exhibited similar shear-thinning property and time-dependent rheological property. The storage moduli of all groups decreased with increasing reaction time from 5min to 15 min, revealing the reaction time as a kinetic parameter.

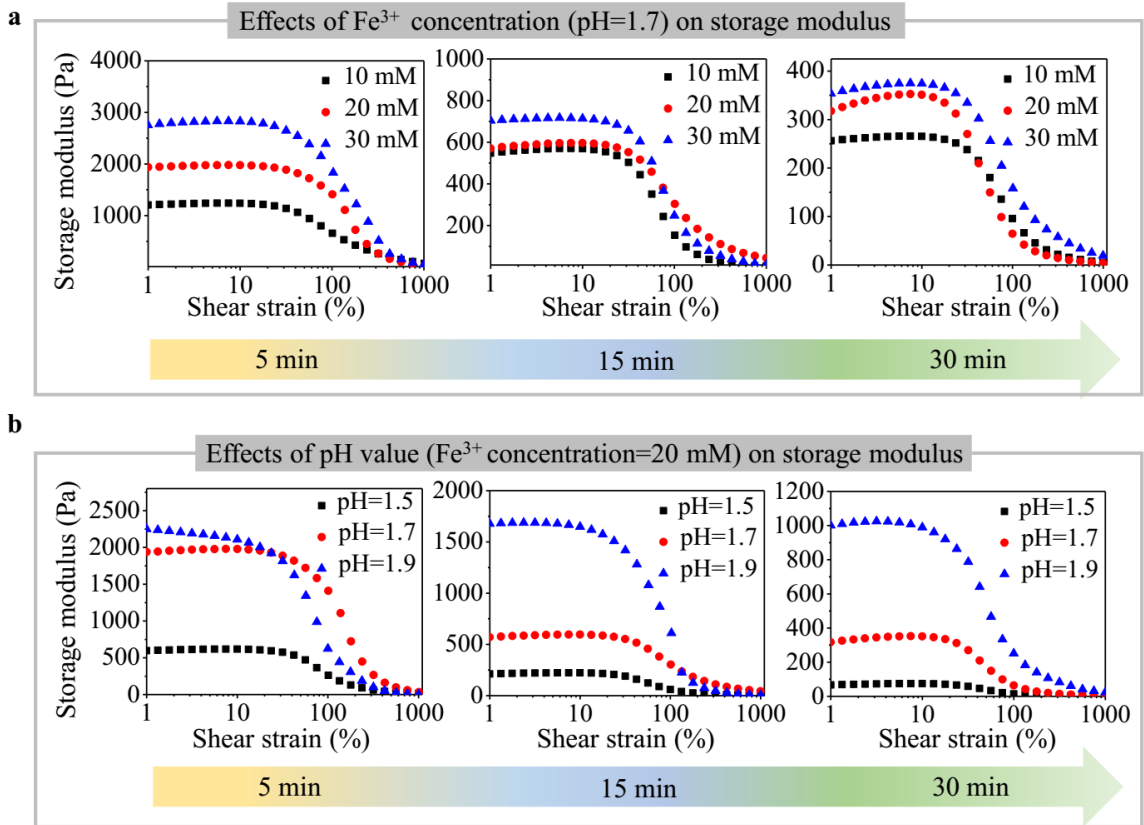


**Figure 2.4** The storage modulus of crosslinked HyA hydrogels demonstrated the effects of Fe<sup>3+</sup> concentration, pH value, and reaction time on the tunable crosslinking of HyA hydrogels. (a) The curves of storage modulus over shear strain for HyA hydrogels crosslinked with 10 mM, 20 mM, and 30 mM FeCl<sub>3</sub> solutions with a constant pH of 1.7 for 5 min (Left), 15 min (Middle), and 30 min (Right). (b) The curves of storage modulus over shear strain for HyA hydrogels crosslinked in the 20 mM FeCl<sub>3</sub> solution with an adjusted pH value of 1.5, 1.7, and 1.9, respectively, for 5 min (Left), 15 min (Middle), and 30 min (Right).

### **2.3.3 Reversible Solid-Liquid Phase Transition of HyA Hydrogels Achieved via the Tunable Ratios of Mono-, Bi-, and Tridentate Coordination and the Resulted Low-to-High Crosslinking Densities**

Solid or liquid phases of the HyA hydrogels are highly tunable and reversible, based on the effects of  $\text{Fe}^{3+}$  ion and  $\text{H}^+$  ion concentrations on the tunable ratios of mono-, bi-, and tridentate coordination and the resulted low-to-high crosslinking densities in HyA hydrogels. We achieved the reversible phase transitions between HyA\_L, HyA\_M, and HyA\_H by controlling the tunable ratios of mono-, bi-, and tridentate carboxylate- $\text{Fe}^{3+}$  coordination, that is, adjusting  $\text{Fe}^{3+}$  and  $\text{H}^+$  (pH) concentrations of the  $\text{FeCl}_3$  solutions, as demonstrated in Figure 2.5. Specifically, we cast a thin layer of HyA solution with the dimension of  $4 \times 8 \times 0.25$  cm in a PTFE mold, and 32 mL of  $\text{FeCl}_3$  solution was poured into the mold to crosslink the hydrogel. When we used 300 mM  $\text{FeCl}_3$  solution in this demonstration, the liquid phase HyA\_L formed at its equilibrium state, based on the conditions established in Figures 2.3 and 2.4. As shown in Figure 2.5a, the formation of HyA\_M and HyA\_L hydrogels is dependent on the reaction time. After 5 min of reaction, the soft HyA\_M hydrogel formed, and it bent when being held vertically using a tweezer. When the reaction time was extended to more than 1 hour, the soft HyA\_M transformed into the viscous liquid HyA\_L. Interestingly, both HyA\_M and HyA\_L transformed to a strong HyA\_H hydrogel when being immersed in deionized (DI) water for 24 hours, and the HyA\_H did not bend when being held up vertically using a tweezer. HyA\_L is a viscous liquid gel with certain fluidity and injectability, as shown in Figures 2.5a and 2.5b. When a thin 1-mm layer of HyA\_L was printed onto a plastic

dish in Figure 2.5b, a piece of soft and bendable hydrogel formed after 5 min of reaction with 20 mL of 30 mM FeCl<sub>3</sub> solution, indicating the phase transition from HyA\_L to HyA\_M. In Figure 2.5c, the stiff HyA\_H shows the phase transition to HyA\_M and HyA\_L. HyA\_H swelled in 300 mM FeCl<sub>3</sub> solution and transformed into soft and bendable HyA\_M after 1 hour of reaction time. After another 1-hour reaction, the transition of solid to liquid phase occurred and a viscous gel of HyA\_L formed, demonstrating the phase transition from HyA\_M to HyA\_L.

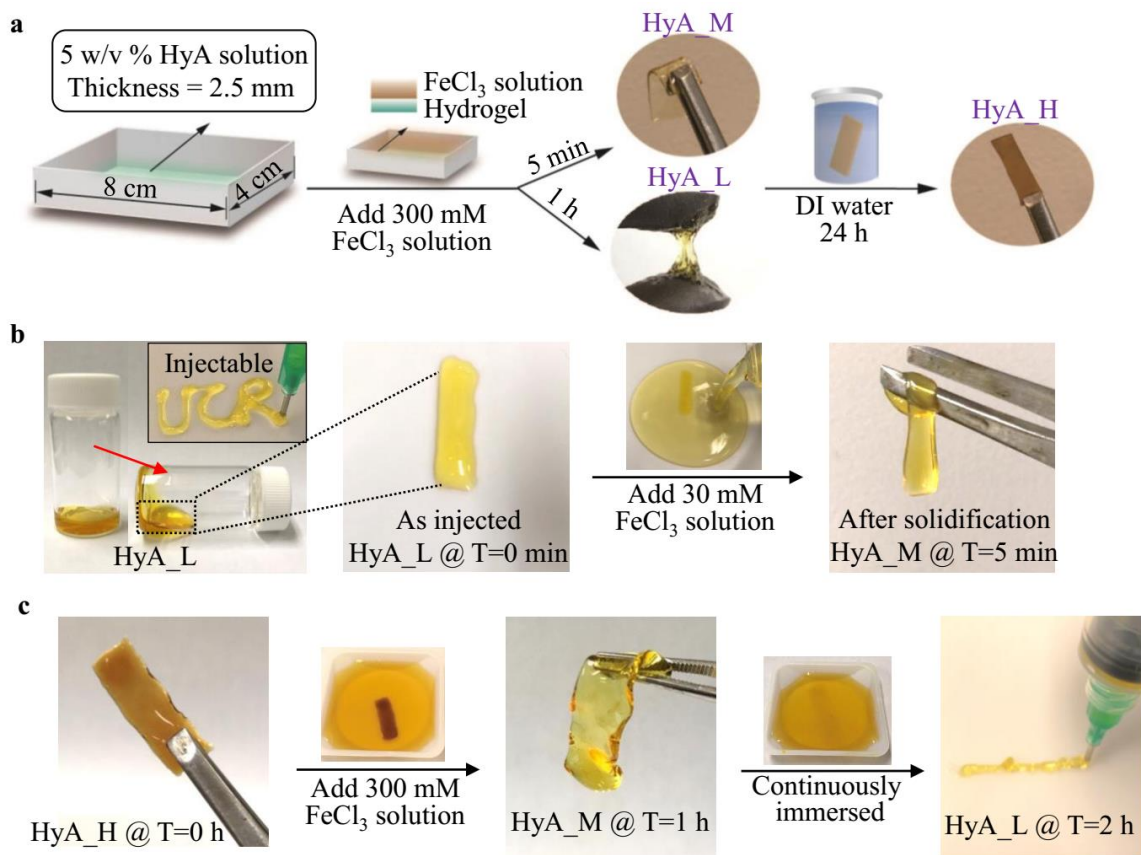


**Figure 2.5** Reversible phase transition of crosslinked HyA hydrogels with low (HyA\_L), medium (HyA\_M), and high (HyA\_H) crosslinking densities. (a) Evidence of phase transition from HyA\_M to HyA\_L, from HyA\_M to HyA\_H, and from HyA\_L to HyA\_H. Specifically, adding 300 mM FeCl<sub>3</sub> solution (indicated in brown color) in the PTFE mold caused crosslinking of HyA solution (indicated in green color). A soft flexible gel (HyA\_M) formed after a 5-min reaction and a viscous liquid gel (HyA\_L) formed after a 1-h reaction. A hard and stiff hydrogel (HyA\_H) formed by immersing HyA\_M or HyA\_L in DI water for 24 hours. (b) Evidence of phase transition from HyA\_L to HyA\_M. The as-injected HyA\_L transformed to HyA\_M after a 5-min immersion in 30 mM FeCl<sub>3</sub> solution. (c) Evidence of phase transition from HyA\_H to HyA\_M and from HyA\_H to HyA\_L. HyA\_H transformed to HyA\_M after being immersed in 300 mM FeCl<sub>3</sub> solution for 1 hour; HyA\_H transformed to HyA\_L after a 2-h immersion in 300 mM FeCl<sub>3</sub> solution.

In the phase transition from HyA\_M to HyA\_H, as shown in Figure 2.6, the dimension such as volume or diameter of HyA hydrogels and the water content in the hydrogel decreased over the reaction time, while the  $\text{Fe}^{3+}$  ion released from the HyA hydrogel increased over the reaction time. The major changes in HyA dimension, water content, and  $\text{Fe}^{3+}$  ion concentration occurred in the first hour of immersion in DI water and reached a plateau after 1 hour. The photographs in Figure 2.6a show that the diameter and volume of HyA\_M shrank dramatically when immersed in DI water over 0-1 hour and gradually transformed into HyA\_H. In Figure 2.6b, when the diameter of HyA\_M was measured over the 96 hours of reaction, the diameter reduced from  $13.02 \pm 0.37$  mm to  $5.63 \pm 0.24$  mm, and the final over initial volume ratio reduced to 0.008 over the first hour, and HyA hydrogel reached an equilibrium state after 1 hour. Similarly, the water content of the hydrogel decreased from  $95\% \pm 0.14\%$  to  $66.78\% \pm 0.95\%$  over the first hour and reached a stable state as shown in Figure 2.6c. The cumulative release of  $\text{Fe}^{3+}$  ions from the hydrogel increased to  $5.45 \pm 0.38$  mg over the first hour of immersion in DI water and stabilized afterward, as shown in Figure 2.6d, following the reverse trend of the changes in diameter, volume ratio, and water content of the HyA hydrogel.

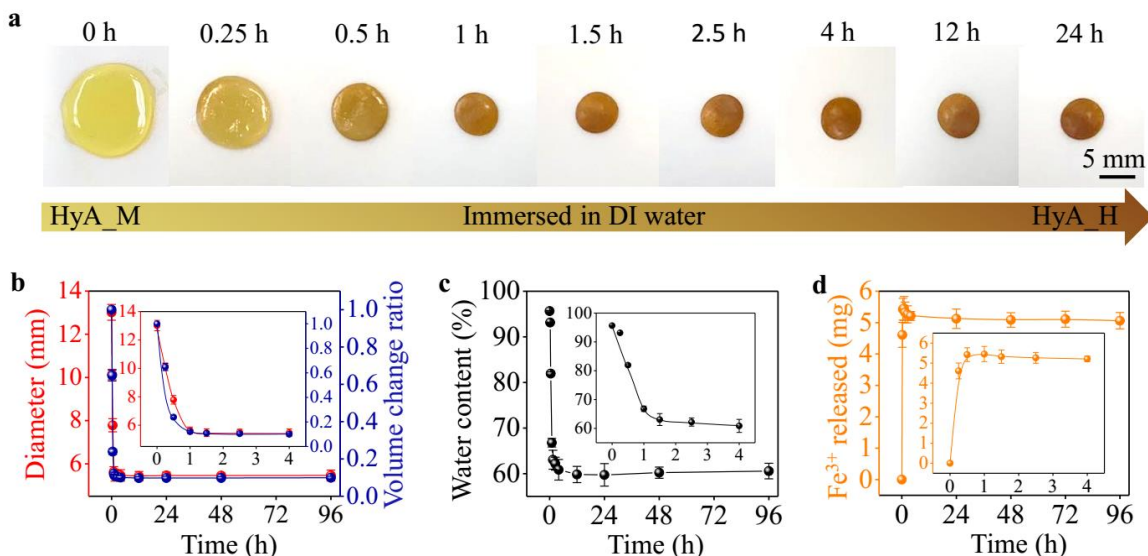


**Figure 2.6** Volume shrinkage of HyA hydrogels. (a) Photographs showing that the HyA\_M in DI water had a dramatic volume shrinkage over time to become HyA\_H (from left to right). (b) Diameter and volume change ratio overtime during the phase transition from HyA\_M to HyA\_H in DI water. Diameter is shown on the left axis with data in red and volume change ratio is shown on the right axis with data in blue. Data are shown as mean  $\pm$  standard deviation ( $n=3$ ). Inset is the magnified graph of the first 4 hours. (c) The water content of the hydrogel overtime during the phase transition from HyA\_M to HyA\_H in DI water. Data are shown as mean  $\pm$  standard deviation ( $n=3$ ). Inset is the magnified graph of the first 4 hours. (d) Cumulative Fe<sup>3+</sup> released overtime during the phase transition from HyA\_M to HyA\_H in DI water. Data are shown as mean  $\pm$  standard deviation ( $n=3$ ). Inset is the magnified graph of the first 4 hours.

### **2.3.4 The Microstructure, Composition, Thermal, Chemical, Mechanical, and Rheological Properties of HyA Hydrogels With Low-to-High Crosslinking Densities**

Figure 2.7 shows the microstructure and composition of HyA\_L, HyA\_M, HyA\_H, and HyA control. As shown in Figure 2.7, scanning electronic microscopy (SEM) images show dramatically different microstructures of the lyophilized HyA\_M, HyA\_H, and HyA control and the Fe distribution of the hydrogels. At the original magnification of 1000x, both HyA\_M and HyA\_H exhibited large pores that were randomly distributed on their cross-sections and formed due to the lyophilization process. Interestingly, at the same magnification of 10000x, the SEM image of the polymeric matrix of the lyophilized HyA\_M shows highly porous networks with a pore size of  $0.91 \pm 0.24 \mu\text{m}$ , while the polymeric matrix of the lyophilized HyA\_H appears much denser with sporadically scattered pores of  $82 \pm 35 \text{ nm}$  in size. The porosity of lyophilized HyA\_M was  $82.88\% \pm 1.52\%$ , which was significantly higher than the lyophilized HyA\_H with a porosity of  $26.98\% \pm 3.31\%$ . This is because HyA\_M had medium crosslinking density, relatively looser hydrogel network, and more space to retain higher water content in its microstructure when compared with HyA\_H with high crosslinking density. The overlaid SEM/EDS maps showed that Fe element distributed around the pores and located on the polymeric network of lyophilized HyA\_M, but uniformly dispersed on the dense polymeric matrix of lyophilized HyA\_H. The atomic percentage of Fe element was 3.3% on the cross-section of lyophilized HyA\_M, and 2.6% on that of HyA\_H. The atomic percentage and distribution of Fe element further confirmed that HyA\_M formed the highly porous polymeric networks because of its lower crosslinking

density than HyA\_H. The SEM images of HyA control showed a highly porous microstructure at both low and high magnifications (1000x and 10000x) with a porosity of  $86.78\% \pm 1.9\%$ . The lyophilized HyA control showed a higher porosity than both HyA\_M and HyA\_H, possibly because 5 w/v% (4.76 wt.%) of HyA solution had a water content of 95.24% and large pores with high porosity formed during the lyophilization process.

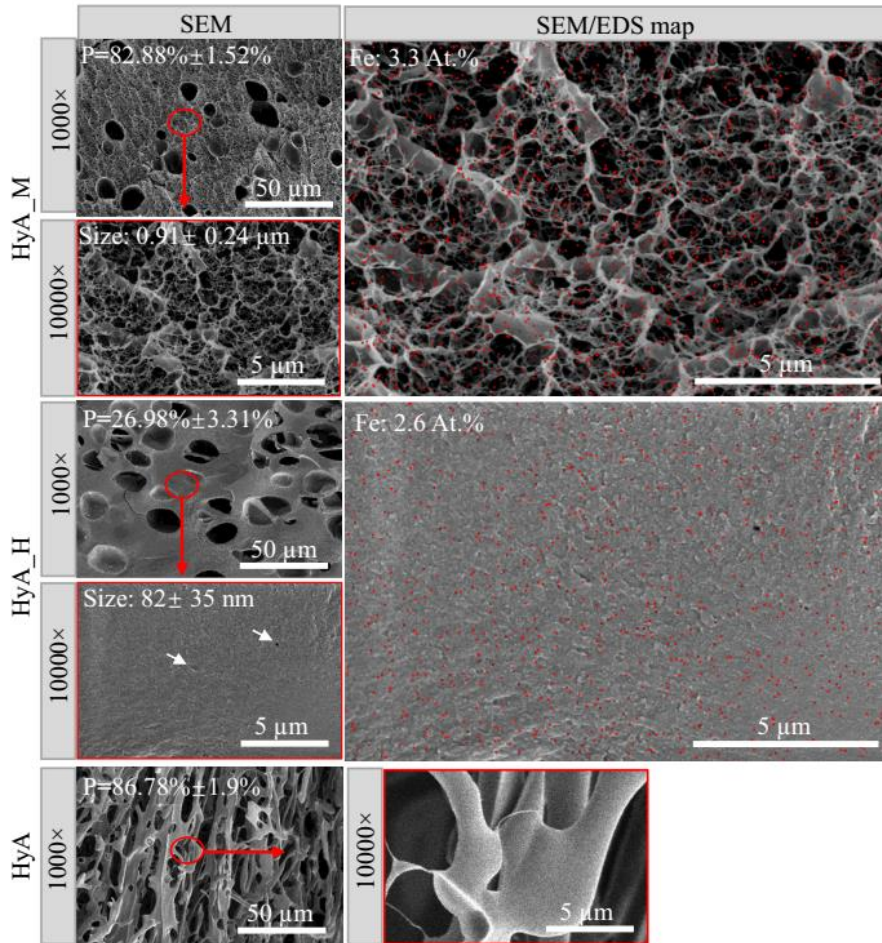


**Figure 2.7** SEM images of cross-sections of lyophilized HyA\_M, HyA\_H, and HyA at the original magnifications of 1000 $\times$  and 10000 $\times$ , and the overlay of SEM and EDS maps for HyA\_M and HyA\_H at the original magnification of 10000 $\times$ . Red circles indicate the areas that were magnified in the images highlighted with the red border. Fe elemental distribution in EDS maps is indicated by red color.

Thermogravimetric analysis (TGA) in Figure 2.8a shows the mass%-temperature curves of lyophilized HyA\_L, HyA\_M, HyA\_H, and HyA control, and varied slopes were observed at distinct temperature ranges. Specifically, HyA\_L first underwent a continuous mass loss of 12% from 50 °C to 150 °C, followed by the second slope of 35% mass loss from 150 °C to 600 °C, and the third slope of 32% mass loss was from 600 °C to 800 °C. After TGA for HyA\_L, 21% of the sample mass remained. The mass%-temperature curves of HyA\_M and HyA\_H were similar with significant overlap, and both samples showed a slope of 12% mass loss from 50 °C to 200 °C, followed by the second slope of 53% mass loss from 200 °C to 400 °C, and then a reduced slope of 15% mass loss for HyA\_M and 12% for HyA\_H from 400 °C to 800 °C. The residual sample mass after TGA was 20% for HyA\_M and 23% for HyA\_H. HyA control showed a mass loss of 8% from 50 °C to 150 °C, and the mass remained stable at 50 °C to 230 °C. Subsequently, a slope of 41% mass loss at 230 °C to 300 °C and a reduced slope of 12% mass loss at 300 °C to 800 °C were observed for HyA control. The residual mass of HyA control after TGA testing was 29%. It has been reported that polysaccharide degradation in the thermogravimetric analysis (TGA) proceeds in four steps, including (1) evaporation of free moisture, (2) dehydration of bonded water, (3) decomposition accompanied by the rupture of C–O and C–C bonds in the ring units resulting in the evolution of CO, CO<sub>2</sub> and H<sub>2</sub>O, and (4) formation of polynuclear aromatic and graphitic carbon structures.<sup>45</sup> Because all of the samples have been lyophilized to remove free moisture before testing, the weight loss at the first slope was mainly attributed to the dehydration of bonded water for HyA\_M, HyA\_H, and HyA control. However, for

HyA\_L, the hydrogel underwent a swelling process and absorbed a large amount of water in its network during the phase transition from HyA\_M to HyA\_L, and the  $\text{Fe}^{3+}$  and  $\text{Cl}^-$  ions dissolved in the absorbed water remained in the lyophilized HyA\_L. Therefore, the lyophilized HyA\_L contained a much higher amount of residual  $\text{FeCl}_3$  particles than the lyophilized HyA\_M and HyA\_H. The residual  $\text{FeCl}_3$  can react with the released water from both  $\text{FeCl}_3 \cdot 6\text{H}_2\text{O}$  and HyA polymeric chain at 100 °C to 200 °C to form  $\text{Fe}(\text{OH})_3$  and HCl gas. The mass loss in the first slope of HyA\_L was therefore possibly due to the dehydration of bonded water and the evaporation of HCl gas. At the temperature higher than 200 °C for HyA\_M and HyA\_H and higher than 230 °C for HyA, the mass loss was mainly caused by the decomposition process of the HyA polymeric phase. For HyA\_L, the mass loss after 150 °C mainly resulted from the decomposition of HyA chains and  $\text{Fe}(\text{OH})_3$ , and a small amount of bonded water and HCl gas could be released at 150 °C-200 °C. It has been reported that  $\text{Fe}(\text{OH})_3$ -polyacrylamide hybrid polymer had a dramatic weight loss from 575 °C to 675 °C because the ionic bond formed between  $\text{Fe}(\text{OH})_3$  and polyacrylamide chains increased the thermal stability of the hybrid,<sup>46</sup> which could explain the second slope of rapid mass loss of HyA\_L after 600 °C. The remaining sample mass is mainly composed of polynuclear aromatic and graphitic carbon materials after decomposition. Moreover, the residual materials of HyA\_L, HyA\_M, and HyA\_H groups may also contain  $\text{Fe}_2\text{O}_3$ , and HyA residual mass may contain  $\text{Na}_2\text{CO}_3$ . As shown in the differential scanning calorimeter (DSC) results in Figure 2.8b, the glass transition temperature ( $T_g$ ) was 125 °C for HyA\_L, 142 °C for HyA\_M, 150 °C for HyA\_H, and 140 °C for HyA. Generally, hydrogels with higher crosslinking density will exhibit a

higher  $T_g$ .<sup>47</sup> The  $T_g$  of HyA hydrogels increased from HyA\_L, to HyA\_M and HyA\_H when the crosslinking densities of these three types of HyA hydrogels increased.  $T_g$  of HyA\_L, however, was much lower than HyA group. which may be attributed to the relatively high content of residual  $FeCl_3$  salt particles. It has been reported that the  $T_g$  of polymer nanocomposites can increase or decrease when the concentration of nanoparticles increases, depending on the specific physical or chemical interactions between the nanoparticles and polymer matrix.<sup>48-49</sup> For example, the alumina nanoparticles in PMMA have been found to reduce  $T_g$  of PMMA nanocomposite, and alumina is known to have limited interactions with PMMA.<sup>50</sup> Similarly, we believe the high content of  $FeCl_3$  particles in HyA\_L may lead to the reduction of  $T_g$ , because the residual  $FeCl_3$  salt particles in lyophilized HyA\_L are expected to have limited interactions with HyA matrix.

Figure 2.8c shows the FTIR-ATR spectra of HyA\_L, HyA\_M, HyA\_H, and HyA control. The red rectangles in Figure 4d highlight the peaks between 1200  $cm^{-1}$  and 1800  $cm^{-1}$  that are assigned to the asymmetric and symmetric stretching vibrations of carboxyl groups.<sup>33</sup> The separation of the bands  $\Delta\nu$ , which is defined as  $\Delta\nu = \nu_{asym}(COO^-) - \nu_{sym}(COO^-)$ , differed for HyA with low-to-high crosslinking densities. Specifically,  $\Delta\nu = 205\text{ cm}^{-1}$  for HyA\_M and  $\Delta\nu = 190\text{ cm}^{-1}$  for HyA\_H, while both HyA\_L and HyA have a  $\Delta\nu$  of  $230\text{ cm}^{-1}$ . The similarity between the spectra of HyA\_L and HyA as highlighted in Figure 2.8c may be attributed to the fact that both samples have monodentate-dominant coordination states. Specifically, HyA\_L had monodentate-dominant carboxylate- $Fe^{3+}$  coordination, while the HyA control had monodentate-

dominant carboxylate- $\text{Na}^+$  coordination because sodium hyaluronate was utilized in this study. The different separation of the bands among the peaks of HyA\_L, HyA\_M, and HyA\_H suggested the change of carboxylate- $\text{Fe}^{3+}$  coordination states, further supporting the transition of the tunable ratios of mono-, bi-, and tridentate coordination illustrated in Figure 2.2c.

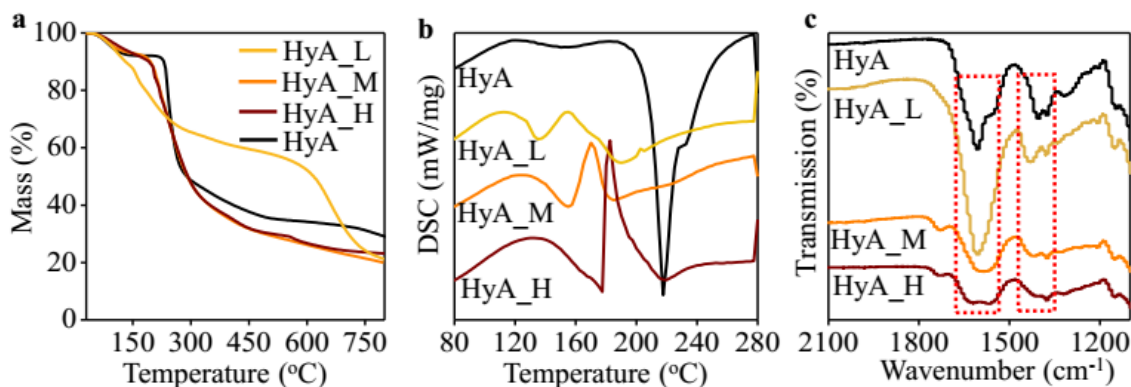


**Figure 2.8** Thermal properties and chemical bonding of HyA hydrogels with low-to-high crosslinking densities. (a) Mass (%) of HyA\_L, HyA\_M, HyA\_H, and HyA as the temperature increased in the TGA testing. (b) DSC curves of HyA\_L, HyA\_M, HyA\_H, and HyA. (c) FTIR-ATR spectra of HyA\_L, HyA\_M, HyA\_H, and HyA.

The tunable ratios of mono-, bi-, and tridentate coordination state determine the low-to-high crosslinking densities and varied microstructures of the hydrogels, which play a significant role in their mechanical properties. Figure 2.9a and 2.9b show the photographs of HyA\_M and HyA\_H during tensile testing, and they were both highly stretchable. The representative stress-strain curves of HyA\_M and HyA\_H in Figure 2.9c demonstrated their huge difference in mechanical properties. Specifically, in Figure 2.9d, the tensile strength of HyA\_H reached  $2620 \pm 490$  kPa, which was almost three orders of magnitude higher than HyA\_M with a tensile strength of  $7.3 \pm 0.65$  kPa. In Figure 2.9e, similar to tensile strength, the tensile modulus of HyA\_H was  $1250 \pm 190$  kPa, while HyA\_M was  $8.66 \pm 1.81$  kPa. In terms of elongation in Figure 2.9f, HyA\_M had an elongation at break of  $330 \pm 81.85\%$ , while that of HyA\_H was  $282.00 \pm 11.53\%$ . The tridentate-dominant coordination state and the resulted high crosslinking density in HyA\_H led to the significantly higher tensile strength and elastic modulus of HyA\_H than HyA\_M. The high elongation at break for both HyA\_M and HyA\_H was attributed to the dynamic coordination that provided the hydrogel with reversible bonding to dissipate the mechanical energy and increase deformability. This mechanism of reversible bonding has also been applied in acrylic polymers to enhance the mechanical properties.<sup>51</sup> For example, carboxylate-Fe<sup>3+</sup> coordination was utilized as a secondary crosslinking to further strengthen the p(AAm-co-AAc) hydrogel which reached a tensile strength of 5.9 MPa.<sup>51</sup> Moreover, different strain rates utilized in the tensile testing dramatically affect the performance of the hydrogels. Figure 2.10 shows the tensile testing results of HyA\_H at different strain rates of 10 mm/min, 20 mm/min, and 30

mm/min. Specifically, as the strain rate increased, tensile strength and tensile modulus of the HyA\_H hydrogels increased but the elongation at break decreased, as shown in Figure 2.10a-2.10d. This is mainly because the reversible coordination bonding in HyA hydrogels is capable of dissipating the mechanical energy generated during the tensile stretching, and the varied strain rates used for tensile testing affect the time available for energy dissipation. For example, at a lower strain rate, more time would be available for reversing the bonding and dissipating the mechanical energy; and thus, the hydrogels should have lower tensile strength and modulus but higher elongation at break in the tensile testing.

The rheological properties of HyA\_L and HyA in Figure 2.9g and 2.9h showed that both HyA\_L and HyA experienced shear-thinning. In Figure 2.9g, the storage modulus and loss modulus of HyA\_L and HyA decreased when the shear strain increased. In Figure 2.9h, the viscosities of HyA\_L ranged from 20514 mPa·s to 1499 mPa·s at the shear rate of 0.1 1/s to 100 1/s, and HyA showed the viscosities from 655000 mPa·s to 6498 mPa·s at the shear rate of 0.1 1/s to 100 1/s. HyA\_L with a low crosslinking density absorbed more water in its network during the solid-liquid phase transition, and thus, had a lower HyA concentration than the HyA control group at 5 w/v% (4.76 wt.%). As a result, HyA\_L had a lower dynamic modulus and viscosity than HyA control.

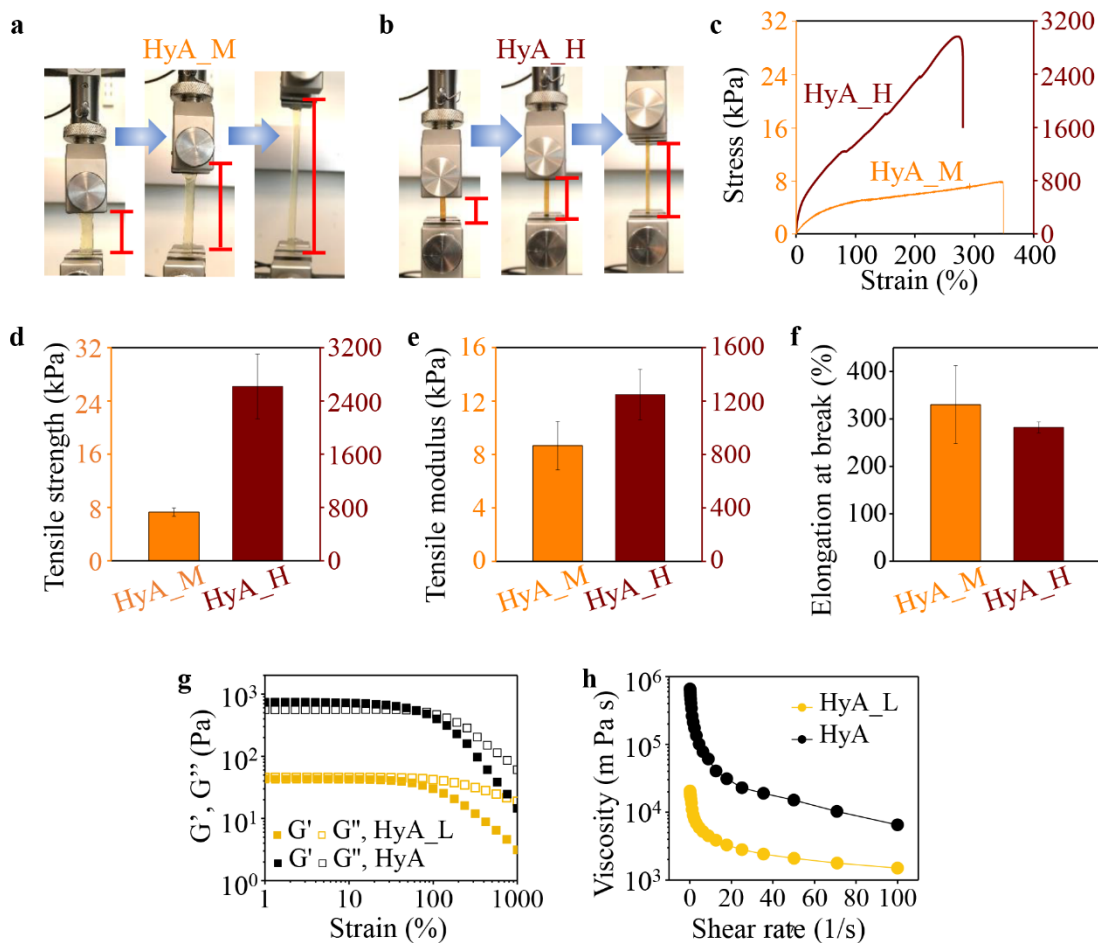


**Figure 2.9** Mechanical and rheological properties of HyA hydrogels with low-to-high crosslinking densities. (a,b) The photographs of elongation for (a) HyA\_M and (b) HyA\_H during the tensile testing. (c) The representative stress-strain curves of HyA\_M and HyA\_H. (d) Tensile strength of HyA\_M and HyA\_H. (e) Tensile modulus of HyA\_M and HyA\_H. (f) Elongation of HyA\_M and HyA\_H at break in the tensile testing. In (c-f), the data for HyA\_M are in orange color on the left axis, and the data for HyA\_H are in red on the right axis. In (d-f), the data are shown as mean  $\pm$  standard deviation ( $n=3$ ). (g) The curves of storage modulus ( $G'$ ) and loss modulus ( $G''$ ) over shear strain for HyA\_L (yellow) and HyA (black) according to the rheological testing. (h) The viscosity over shear rate for HyA\_L (yellow) and HyA (black).

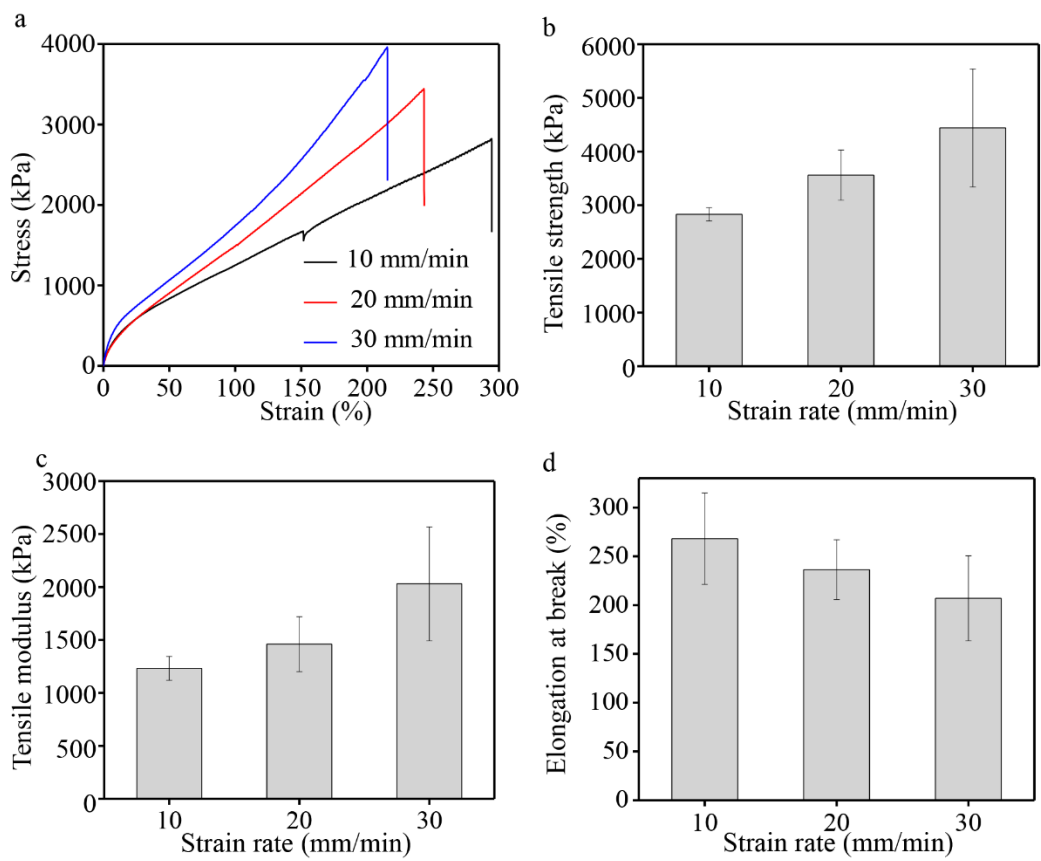


**Figure 2.10** Tensile testing results of HyA\_H at different strain rates. (a) Representative stress-strain curves from the tensile testing of HyA\_H at different strain rates of 10 mm/min, 20 mm/min, and 30 mm/min. (b) Tensile strength of HyA\_H at different strain rates of 10 mm/min, 20 mm/min, and 30 mm/min. (c) Tensile modulus of HyA\_H at different strain rates of 10 mm/min, 20 mm/min, and 30 mm/min. (d) Elongation at break of HyA\_H at different strain rates of 10 mm/min, 20 mm/min, and 30 mm/min. Data in (b, c, d) are shown as mean  $\pm$  standard deviation (n=3).

## 2.4 Discussion

In this part, I elucidated the principles of dynamic coordination of  $\text{Fe}^{3+}$  ions with carboxyl groups and applied these thermodynamic and kinetic principles to integrate the tunable crosslinking and reversible phase transition of HyA hydrogels. Thermodynamically,  $\text{Fe}^{3+}$  and  $\text{H}^+$  concentrations define the tunable coordination states at equilibrium; and kinetically, the reaction time defines the intermediate states of the hydrogels, as illustrated in Figure 2.2. The reversible solid-liquid phase transition HyA hydrogels are based on the tunable crosslinking densities of HyA hydrogels at specific conditions that we revealed in this article. Specifically, the tunable ratios of mono-, bi-, and tridentate coordination of the hydrogels determine the crosslinking densities of the HyA hydrogels, which enables the reversible solid-liquid phase transition of hydrogels. Additionally, we believe the tunable and reversible crosslinking can enable the self-healing capacity of hydrogels.<sup>35</sup>

Thermodynamically, both  $\text{Fe}^{3+}$  and  $\text{H}^+$  concentrations determine the tunable coordination state and crosslinking density of the HyA hydrogel at its equilibrium state. As shown in Equations (2.5a)-(2.8a), at the same HyA concentration with innate pH, the  $\text{Fe}^{3+}$  ion concentration directly determines the ratio of  $[\text{Fe}^{3+}\text{COO}^-]/[\text{COO}^-]$ ,  $[\text{Fe}^{3+}(\text{COO}^-)_2]/[\text{COO}^-]^2$ , and  $[\text{Fe}^{3+}(\text{COO}^-)_3]/[\text{COO}^-]^3$ . That is, the ratios of  $[\text{Fe}^{3+}\text{COO}^-]/[\text{COO}^-]$ ,  $[\text{Fe}^{3+}(\text{COO}^-)_2]/[\text{COO}^-]^2$ , and  $[\text{Fe}^{3+}(\text{COO}^-)_3]/[\text{COO}^-]^3$  increase when the  $\text{Fe}^{3+}$  ion concentration increase. As shown in Equation (2.8a), the  $\text{H}^+$  ion concentration (pH) of HyA solution directly determines the ratio of  $[\text{H}^+\text{COO}^-]/[\text{COO}^-]$ . That is, when the pH of

HyA solution decreases, the ratio of  $[H^+COO^-]/[COO^-]$  increases, because more  $COO^-$  ligands are bonded with  $H^+$  ions. The innate pH of HyA solution decreases when the concentration of HyA increases; and the pH of HyA solution can also be intentionally adjusted to be higher or lower using an acid such as HCl. The concentration ratios of mono-, bi-, and tridentate carboxylate- $Fe^{3+}$  to carboxylate- $H^+$  coordination (on the left of Equation 2.5b-2.7b) determine the HyA crosslinking density. As shown in Equation (2.5b-2.7b),  $K_1$ ,  $K_2$ ,  $K_3$ , and  $K_4$  are constant when the environmental conditions such as temperature and pressure are the same. As shown in Equation (2.5b), the ratio of  $Fe^{3+}$  and  $H^+$  ion concentration, that is,  $[Fe^{3+}]/[H^+]$ , directly determines the ratio of monodentate  $[Fe^{3+}COO^-]/[H^+COO^-]$ , when  $K_1$  and  $K_4$  are constants. In the cases of bidentate and tridentate coordination in Equation (2.6b) and (2.7b), both  $[Fe^{3+}]/[H^+]$  and the  $[COO^-]$  (i.e., the concentration of free  $COO^-$  in HyA) determine the ratios of bi and tridentate coordination states, that is,  $[Fe^{3+}(COO^-)_2]/[H^+COO^-]$  and  $[Fe^{3+}(COO^-)_3]/[H^+COO^-]$ . The ratios of bi- and tridentate coordination states directly define the HyA crosslinking density.

The relationship between the HyA crosslinking density at equilibrium and the concentrations of  $Fe^{3+}$  and  $H^+$  ions in Equation (2.5b-2.7b) clearly explains the results in Figure 2.3a, that is, why HyA was crosslinked to retain its 3D shape in 5-30 mM  $Fe^{3+}$  solutions but dissolved in >30 mM (50-300 mM)  $Fe^{3+}$  solutions after 24 hours of reaction. Specifically, Figure 2.1 in supporting materials showed the innate pH of  $FeCl_3$  solution had a negative linear relationship with the logarithmic form of  $Fe^{3+}$  concentration, which suggested that the  $FeCl_3$  solutions with innate pH values have a

constant ratio of  $[\text{Fe}^{3+}]/[\text{H}^+]$ . Moreover, at the constant HyA concentration, more free carboxyl groups ( $\text{COO}^-$ ) became bonded to  $\text{Fe}^{3+}$  ions when  $\text{Fe}^{3+}$  concentration increased, as shown in Equation (2.5a-2.7a). This means that the concentration of free carboxyl groups ( $[\text{COO}^-]$ ) decreases as  $\text{Fe}^{3+}$  concentration increases when HyA concentration remains the same. As shown in Equation (2.5b-2.7b),  $[\text{Fe}^{3+}(\text{COO}^-)_2]/[\text{H}^+ \text{COO}^-]$  ratio and  $[\text{Fe}^{3+}(\text{COO}^-)_3]/[\text{H}^+ \text{COO}^-]$  ratio will decrease as  $[\text{COO}^-]$  decreases, when  $K_2$ ,  $K_3$ ,  $K_4$ , and  $[\text{Fe}^{3+}]/[\text{H}^+]$  ratio are constant. In these cases, when the concentration of  $\text{FeCl}_3$  solutions was increased to be higher than 30 mM (50-300 mM),  $[\text{Fe}^{3+}]/[\text{H}^+]$  ratio retained as a constant and  $[\text{COO}^-]$  decreased, resulting in the decrease of  $[\text{Fe}^{3+}(\text{COO}^-)_2]/[\text{H}^+ \text{COO}^-]$  ratio and  $[\text{Fe}^{3+}(\text{COO}^-)_3]/[\text{H}^+ \text{COO}^-]$  ratio. The hydrogel thus transitioned toward the monodentate-dominant coordination state, which resulted in low crosslinking density as seen in the swelling and dissolution of the HyA in the high concentrations of 50-300 mM  $\text{FeCl}_3$  solutions.

Kinetically, the formation rate of coordination bond is determined by the kinetic constant  $k(T)$  that is defined below:

$$k(T) = Ae^{-E_a/RT} \quad (2.9)$$

where  $T$  is the temperature,  $A$  is the constant of proportionality,  $E_a$  is the activation energy, and  $R$  is the gas constant. Upon the addition of  $\text{FeCl}_3$  solution to HyA solution, HyA\_M with a mix of mono-, bi, and tridentate carboxylate- $\text{Fe}^{3+}$  coordination first formed because the formation of carboxylate- $\text{Fe}^{3+}$  coordination has a greater  $k(T)$  than carboxylate- $\text{H}^+$  bonding. As the reaction time increased,  $\text{Fe}^{3+}$  ions at the coordination sites are gradually replaced by  $\text{H}^+$  ions toward the equilibrium state of

coordination bonding. The rheological results in Figures 2.4a and 2.4b confirmed that the reaction time is a kinetic factor.

Our FTIR-ATR spectra in Figure 2.8c confirmed the varied coordination states of HyA\_L, HyA\_M, and HyA\_H and their differences in chemical bonding. The dramatic differences in microstructure, glass transition temperature, and rheological and mechanical properties of HyA\_L, HyA\_M, and HyA\_H also confirmed their differences in crosslinking densities, which indicates their respective changes in the coordination states. Similarly, the changes of the dynamic coordination states have been demonstrated in another study where the poly(acrylamide-co-acrylic acid) (p(AAm-co-AAc)) hydrogels were crosslinked via carboxylate-Fe<sup>3+</sup> coordination.<sup>51</sup> Specifically, when adding Fe<sup>3+</sup> ions in a pre-crosslinked p(AAm-co-AAc) hydrogel, Fe<sup>3+</sup> ions formed a mixed coordination of mono-, bi-, and tridentate bonding with carboxyl groups on the PAA molecular chains. When the hydrogel was immersed in DI water, the coordination bonding was reorganized and Fe<sup>3+</sup> ions formed tridentate-dominant coordination with carboxyl groups, resulting in the enhanced mechanical properties of the hydrogels. Moreover, Lee et. al. also confirmed the changes of coordination states under different conditions in the catechol modified HyA hydrogels crosslinked via catechol-Fe<sup>3+</sup> ion coordination, and showed monodentate-dominant coordination at the pH of 4-5, bidentate-dominant coordination at the pH of 7-8, and tridentate-dominant coordination at the pH of 10-11.<sup>39</sup>

We demonstrated the reversible phase transition in Figure 2.5 under the specific conditions that we identified according to the thermodynamic and kinetic principles. Thermodynamically, the phase reversibility of a hydrogel crosslinked via metal-ligand

coordination is dependent on the equilibrium constant ( $K_{eq}$ ) of the coordination bonds. If the  $K_{eq}$  value is excessively large (e.g.,  $> 10^{40}$ ), the hydrogels are considered to be too stable to be characterized by a “break-after-recovery” behavior, i.e. irreversible<sup>35, 52</sup> If the  $K_{eq}$  is in a range of  $10^3$ - $10^{40}$ , the phase reversibility and self-healing property of the hydrogels could be achieved.<sup>35</sup>

## 2.5 Conclusion

This chapter elucidated the mathematical relationships of the  $Fe^{3+}$  and  $H^+$  ion concentrations and the reaction time in controlling dynamic coordination of  $Fe^{3+}$  ions with the innate carboxyl groups on HyA chains, and demonstrated the integration of tunable crosslinking and reversible phase transition of HyA hydrogels for the first time. The concentrations of  $Fe^{3+}$  and  $H^+$  ions and the reaction time determined the tunable ratios of mono-, bi-, and tridentate coordination states and the resulted low-to-high crosslinking densities of the HyA hydrogels. The liquid or solid hydrogels of HyA\_L, HyA\_M, and HyA\_H with low-to-high crosslinking densities were prepared and the reversible phase transition among these hydrogels was demonstrated by controlling the concentrations of  $Fe^{3+}$  and  $H^+$  ions and the reaction time. Specifically, HyA\_L was a viscous liquid. The solid stiff HyA\_H had a much lower porosity in microstructure than the solid soft HyA\_M, and exhibited a dramatically higher tensile strength and tensile modulus than HyA\_M.

## CHAPTER 3 Three-Dimensional Printing of Hyaluronic Acid Hydrogels via Reversible Phase Transition: Cold-Stage and Direct Writing Approaches

### 3.1 Introduction

Traditionally, unmodified HyA solution is not considered to be 3D printable because of the limited structural stability of the printed constructs.<sup>37</sup> Hydrogels crosslinked via interactions between carboxyl groups and cations such as Fe<sup>3+</sup> ions usually lose injectability and 3DP capability because the rapid crosslinking process makes the hydrogel solidify so quickly that it is difficult to extrude the solid hydrogel out of a needle or nozzle. Although some researchers have achieved tunable crosslinking densities<sup>33</sup> and reversible solid-liquid phase transition<sup>39-40</sup> of the hydrogel via metal-ligand coordination chemistry, the 3DP of these hydrogel has not been demonstrated. As we mentioned above, HyA has been blended with other polymers<sup>20-21</sup> or modified with new functional groups<sup>12, 28, 37-38</sup> to achieve the 3DP capability. Currently, only a few strategies, such as adamantane (Ad)-cyclodextrin (CD) guest-host dynamic crosslinking,<sup>37-38</sup> bisphosphonate (BP)-Ca<sup>2+</sup> coordination, and photocrosslinking<sup>12</sup> were utilized to achieve the 3DP of HyA hydrogels without blending polymers. For both Ad-CD guest-host interaction<sup>37-38</sup> and BP-Ca<sup>2+</sup> coordination<sup>28</sup> methods, the 3D printed constructs had limited structural stability, and a supportive hydrogel was required during printing, especially for the printing of complex structures.<sup>28, 38</sup> The 3DP of HyA hydrogel without a supportive gel can be achieved when the HyA molecular chains were modified

with photocurable functional groups and the UV irradiation was applied during the printing process. For example, when methacrylate groups were added to HyA chains modified with respective Ad or CD groups (named as Ad-MeHyA and CD-MeHyA), HyA hydrogel can be printed onto a glass substrate under UV irradiation and showed desired structural stability.<sup>37</sup> Another example also showed that HyA functionalized with methacrylate groups (MeHyA) can be 3D printed to porous cubes and non-porous human L3 vertebrae shapes under UV irradiation.<sup>12</sup> However, blending polymers or new functional groups may raise additional concerns on their interactions with host cells and biocompatibility for medical applications, especially when the regulatory approval is required for clinical translation of final products.<sup>2, 41-42</sup>

In Chapter 2, tunable crosslinking and reversible liquid-solid phase transition of HyA hydrogels were achieved and demonstrated. I hypothesized that 3D printable HyA (HyA\_P) can be prepared by controlling the coordination state and the resulted crosslinking density of the hydrogel. Specifically, HyA hydrogels with a crosslinking density between that of HyA\_L and HyA\_M may have injectability and relatively good structural stability at the same time. The HyA\_P can retain its structure after 3D printing, and the 3D printed constructs can be transformed to HyA\_H to further increase their structural stability. Based on the principles of liquid-solid phase transition, two 3D printing approaches, namely cold-stage and direct writing methods, were demonstrated in this Chapter, for the first time.

## **3.2 Materials and Methods**

### **3.2.1 Determine the Conditions for Preparing HyA\_P**

Crosslinked HyA hydrogels were prepared by injecting 5 w/v% HyA solution into 300 mM FeCl<sub>3</sub> solution using a syringe with a needle size of 0.35 mm. The reaction time was set to be 5 min, 15 min, 30 min, and 120 min. The samples were collected using a spoon for rheological testing using the same method as described above. The storage modulus, loss modulus, and viscosity of crosslinked HyA hydrogels with different reaction times and HyA control (5 w/v%) were measured to highlight the conditions to achieve HyA\_P.

### **3.2.2 Demonstrate Cold-Stage Method and Direct Writing Method for 3D-Printing of the HyA\_P**

To prepare the HyA\_P, 10 mL of HyA solution at the concentration of 5 w/v% was injected into 40 mL of 300 mM FeCl<sub>3</sub> solution using a syringe with a needle size of 0.35 mm. After 15 min of reaction, the HyA\_P was collected using a spoon and filled in the printing tube. HyA\_P was printed onto the cold petri dish surface at 0 °C using a 3D Bioplotter (Developer series, EnvisionTec, Germany). The architecture was changed by printing filaments with 0 and 90 angles between two successive layers. The injection pressure, speed of the printing head, nozzle size, and the distance between neighboring filaments were set as 1.5~3.0 bar, 5~10 mm/s, 0.84 mm, and 2.3 mm, respectively. After printing, the as-printed gel was immersed in DI water for 24 hours, and optical images of

both the top and bottom view of the printed sample were recorded using an optical microscope (SE303R-P, Amscope).

HyA\_P was prepared using the same protocol described above, but the reaction time was extended to 1 h. The HyA\_P was directly printed onto a petri dish (10 cm in diameter) containing DI water. To increase the adhesion of the printed gel onto the substrate, masking tape was placed on the bottom of the dish to increase surface roughness. The injection pressure, speed of the printing head, nozzle size, and the distance between two neighbor filaments were set as 1~1.5 bar, 3~8 mm/s, 0.84 mm, and 2.3 mm, respectively. After printing, the printed gel was immersed in DI water for 24 hours, and optical images of both top and bottom views of the printed sample were recorded using optical microscopy (SE303R-P, Amscope).

### **3.2.3 Evaluate the Morphology and Structural Stability of the Filaments Printed by Two Different Methods**

For the cold-stage method group, a single filament was printed on a cold petri dish surface at 0 °C, kept at room temperature and pressure for 0 min, 1 min, 5 min, and 10 min, respectively, and then immersed in DI water for 24 h. For the direct writing method group, a single filament was directly printed into a petri dish with DI water, and these filaments were continuously immersed in DI water during printing and after printing for 24 h. The filaments were cut, and their cross-sections were imaged using optical microscopy (SE303R-P, Amscope). The height (H) and width (W) of the filament cross-section in the optical micrographs were measured using Image J. The aspect ratio

(AR) of height/width was calculated for the filament cross-section. These measurements were repeated for 5 samples.

### **3.3 Results**

#### **3.3.1 Effects of Fe<sup>3+</sup> and H<sup>+</sup> Ion Concentrations and Reaction Time on HyA\_P for 3DP**

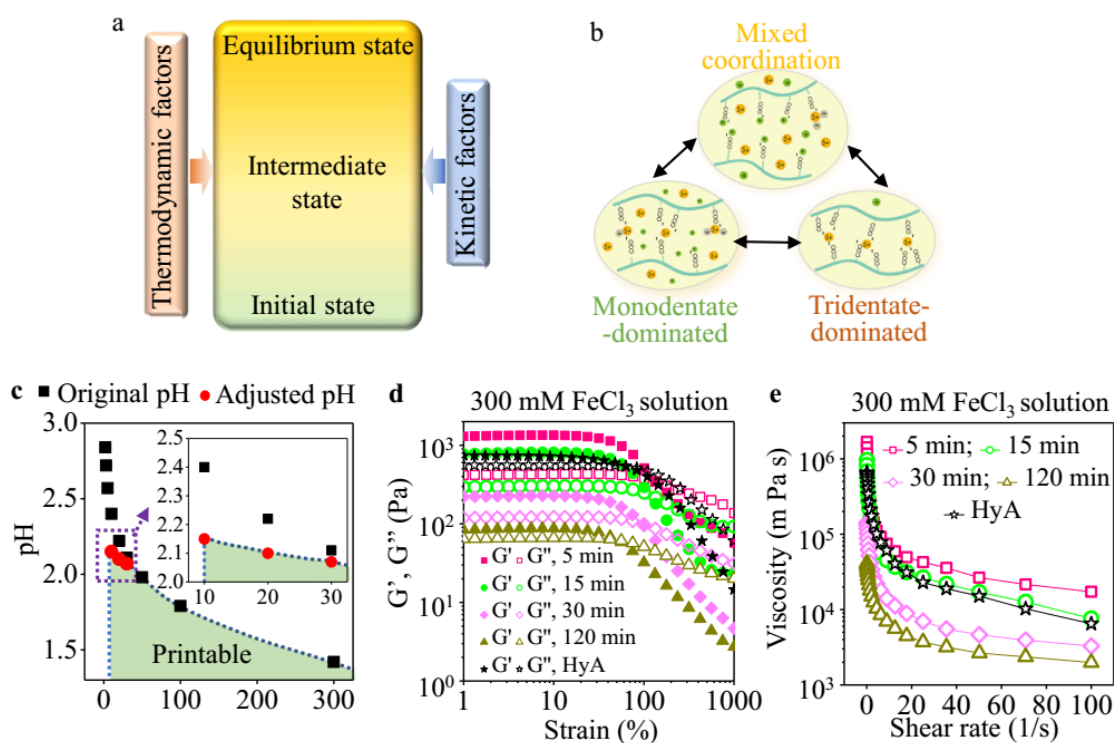
We further demonstrated the feasibility of 3DP of HyA via dynamic coordination of carboxylate-Fe<sup>3+</sup> ion, inspired by the tunable crosslinking densities and reversible phase transition capability of HyA achieved via tunable ratios of mono-, bi-, and tridentate coordination (Figures 3.1a and 3.1b). Traditionally, unmodified HyA solution is not considered to be 3D printable because of the limited structural stability of the printed constructs.<sup>37</sup> In this study, we demonstrated that HyA hydrogels had tunable crosslinking densities and reversible phase transition capability, enabling 3DP at certain conditions.

Figure 3.1c shows the conditions of Fe<sup>3+</sup> concentration and pH value at which the solid-to-liquid phase transition can be achieved, based on the data in Figures 2.3 and 2.4. We identified the range of crosslinking densities of HyA hydrogels that are between HyA\_L and HyA\_M (Figure 2.2c), at which HyA gels have good injectability under certain shear strain due to the shear thinning and the printed structures have good structural stability after 3DP. Hereafter, the 3D printable HyA gel with the suitable range of coordination states and crosslinking densities was named as HyA\_P. Theoretically, FeCl<sub>3</sub> solution at the concentrations and pH values in the green region in Figure 3.1c can

produce HyA\_P with the crosslinking densities between HyA\_L and HyA\_M. Moreover, we can obtain HyA\_P either by (1) reversing the crosslinking from HyA\_H or HyA\_M to HyA\_P via the reversible phase transition, or (2) directly crosslinking the HyA to HyA\_P under specific conditions. In this article, we used method (1) to demonstrate the 3DP of HyA hydrogel.

Specifically, HyA\_M or HyA\_H was immersed in FeCl<sub>3</sub> solutions at the concentrations and pH values in the green region of Figure 3.1c, for a specific suitable reaction time, to reverse the crosslinking to achieve HyA\_P. The suitable reaction time is dependent on the specific concentration and pH of FeCl<sub>3</sub> solutions. To demonstrate, we injected 5w/v% HyA solution to 300 mM FeCl<sub>3</sub> solution with an innate pH of 1.3 to form HyA\_M immediately, and then we extended the reaction time to 5-120 min to achieve HyA\_P. Figure 3.1d and 3.1e show the various rheological properties of partially crosslinked HyA\_P that were produced with the extended reaction time of 5 min (red square), 15 min (green circle), 30 min (pink diamond), and 120 min (brown triangle), respectively, and HyA control (black star). Storage modulus ( $G'$ ), loss modulus ( $G''$ ), and viscosity of the various HyA\_P all decreased when the reaction time increased. For all of the samples,  $G'$  and  $G''$  decreased when the shear strain increased as shown in Figure 3.1d, and their viscosity also decreased when the shear strain rate increased as shown in Figure 3.1e. The partially crosslinked HyA\_P and HyA control all exhibited a solid-state at low shear strain range ( $G' > G''$ ). Specifically, the “gel point” ( $G' = G''$ ) of the partially crosslinked HyA gels at different reaction time was 156% at 5 min, 118% at 15 min, 100% at 30 min, and 49% at 120 min. In contrast, the “gel point value” for the

5w/v% HyA control was 73%. The results further confirmed that at the specific  $\text{Fe}^{3+}$  concentration and pH value, the rheological properties ( $G'$ ,  $G''$ , and viscosity) of partially crosslinked HyA\_P are controllable and tunable simply by adjusting the reaction time of HyA\_M or HyA\_H in  $\text{FeCl}_3$  solution.



**Figure 3.1** The conditions required for three-dimensional printing (3DP) of crosslinked HyA gels. (a) Illustration showing thermodynamic and kinetic factors determine the coordination states of HyA hydrogels. (b) Three coordination states of HyA hydrogels. (c) Boundary conditions of  $\text{FeCl}_3$  concentrations and pH values for HyA gel to be printable. The green region indicates the conditions with feasible  $\text{FeCl}_3$  concentration and pH value for achieving printability of crosslinked HyA gels. (d) The curves of storage modulus ( $G'$ ) and loss modulus ( $G''$ ) over shear strain for the HyA hydrogels crosslinked in 300 mM  $\text{FeCl}_3$  solution for the reaction time of 5-120 min and non-crosslinked HyA. (e) The viscosity of the crosslinked HyA hydrogels and non-crosslinked HyA in (b). In (b,c), red square, green circle, pink diamond, and brown triangle indicate the reaction time of 5, 15, 30, and 120 min, respectively; and the black star indicates a non-crosslinked HyA solution as a control.

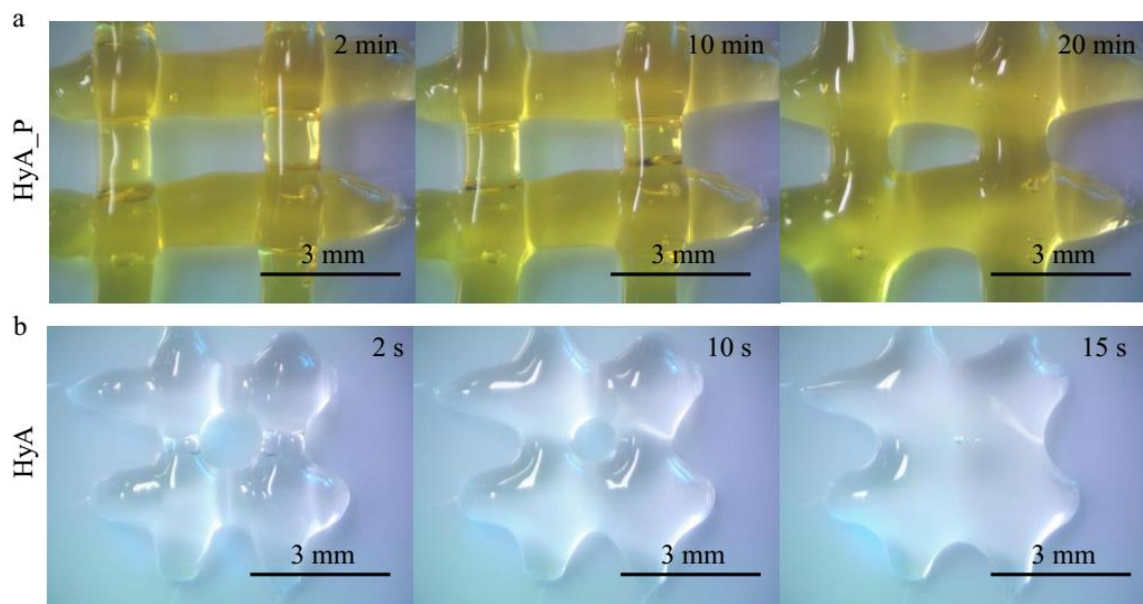


**Figure 3.2** Structural stability of (a) the printable gel (HyA\_P) with a crosslinking density between HyA\_L and HyA\_M over a period of 20 minutes, in contrast to the rapid structural change of (b) the HyA control over 15 seconds, after they were printed or injected onto the surface of a petri dish.

A balance between structural stability and injectability should be achieved for 3DP of the hydrogels. The hydrogels that require a higher shear strain to reach the gel point in Figure 3.1d should have higher structural stability. For example, the HyA\_P produced at 15-min reaction time showed better structural stability than HyA in Figure 3.2. Specifically, when printed or injected onto the surface of a petri dish, HyA\_P produced using 15-min reaction time still maintained its original structure after 20 min (Figure 3.2a) while the HyA control lost its original architecture rapidly after 15 s (Figure 3.2b). However, the hydrogels with high viscosity may require higher force or pressure to inject or extrude for 3DP, which poses additional requirements for 3DP instruments.

As demonstrated in Figures 3.3a and 3.3b, we used two strategies for 3DP of HyA hydrogels, namely, the cold-stage method and the direct writing method. In Figure 3.3a, we printed HyA\_P on a cold stage at 0 °C to enhance the structural stability of the printed constructs and then immersed the printed constructs in DI water to achieve stable HyA\_H. In Figure 3.3b, we directly printed HyA\_P in DI water, utilizing the phase transition from HyA\_P to HyA\_H in water and the supporting benefit of water to enhance the structural stability of the printed constructs. The requirements on the rheological properties of the HyA\_P were different in these two 3DP methods. The cold-stage method requires HyA\_P to have high structural stability and good injectability, and thus, the reaction time in 300 mM FeCl<sub>3</sub> solution should be 15 min to 30 min to obtain HyA\_P. In contrast, the direct writing method reduces the requirements for structural stability and accepts the HyA\_P with a wider range of structural stability, because the phase transition from HyA\_P to HyA\_H in water provides additional structural stability during 3DP. Thus, the suitable reaction time in 300 mM FeCl<sub>3</sub> solution should be 15 min to 120 min to obtain HyA\_P for direct writing.

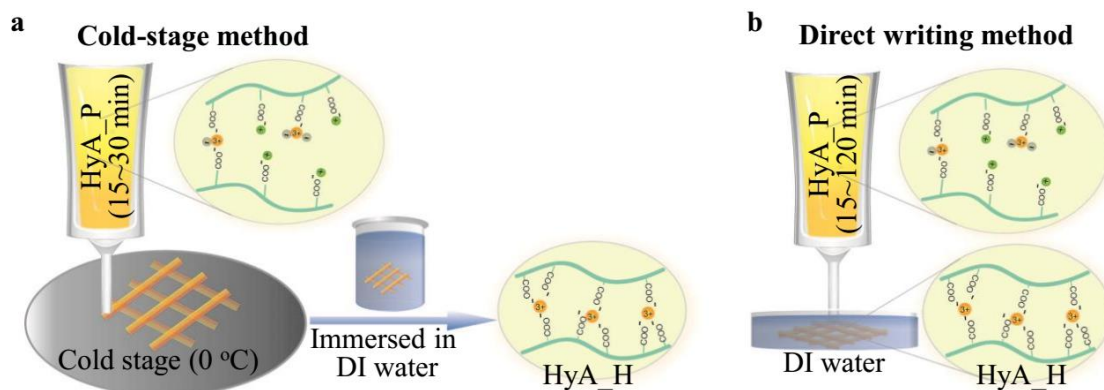


**Figure 3.3** Illustration showing two types of 3D printing methods. (a) Illustration of the cold-stage method for 3DP of printable HyA hydrogels (named as HyA\_P), in which the HyA\_P was printed on a cold stage followed by immersing in DI water. (b) Illustration of the direct writing method for 3DP of HyA\_P, in which the HyA\_P was directly printed in DI water at room temperature.

### 3.3.2 Morphology and Structural Stability of 3D Printed HyA Hydrogels via Cold-Stage and Direct Writing Methods

The optical micrographs in Figure 3.4a show the top and bottom view of the printed HyA hydrogels via the cold-stage method, and the printed structure appeared similar to what we designed. The images presented that the printed filament on the top layer maintained the original cylindrical shape well while the filament on the bottom layer exhibited flat. The deformation of filaments on the bottom was attributed to the spreading of the gel on the substrate during the printing process. The magnified image shows that the intersection of two filaments at neighboring layers deformed due to the surface tension. The optical micrographs in Figure 3.4b exhibit the hydrogels printed using the direct writing method with the layer-by-layer structure as what we designed. The filaments of hydrogels presented similar morphology at both top and bottom view,

and all maintained their original cylindrical shape after printing. Moreover, the intersection of two layers from neighboring layers also maintained an ideal cylindrical structure, further indicating the significant structural stability enhancement effects of the phase transition from HyA\_P to HyA\_H and water on the 3DP. Figure 3.4c shows the comparison of the cross-sections for the hydrogel filaments printed via the cold-stage method and direct writing method. For filaments prepared using the cold-stage method, these gels were kept for 0 min, 1 min, 5 min, and 10 min, respectively, at room temperature and pressure, after printing, and were then immersed in DI water for 24 h. The representative micrographs show that the filament printed on the cold stage gradually deformed due to the gravity. The quantitative height/width ratio of the cross-section reduced with time for the samples that were printed using the cold-stage method and were kept in room conditions for a different time, specifically,  $0.85\pm 0.08$  for 0 min,  $0.79\pm 0.04$  for 1 min,  $0.59\pm 0.04$  for 5 min, and  $0.47\pm 0.05$  for 10 min. In contrast, the cross-section of filament printed by direct writing method showed a near-circular shape with a height/width ratio of  $0.9\pm 0.05$ , and confirmed that the hydrogels printed in DI water retained their structure better and are more close to the designed structure.

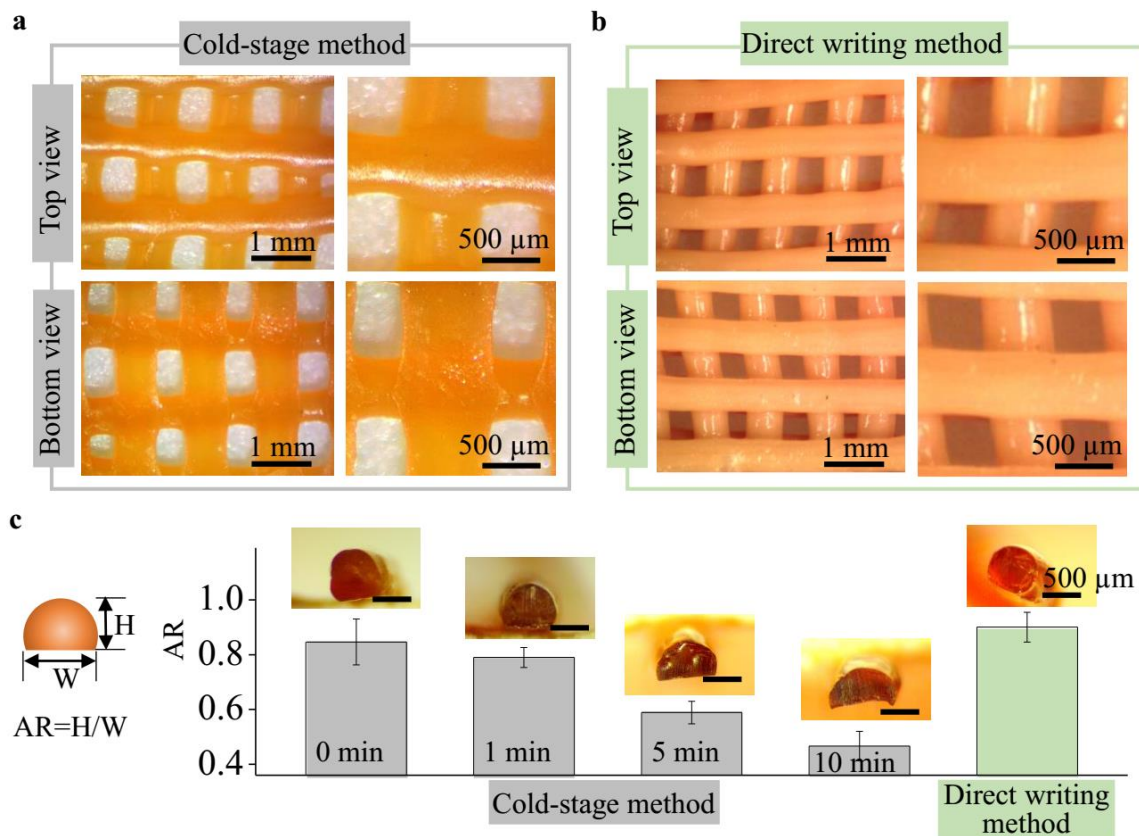


**Figure 3.4** Structural stability of 3D printed constructs. (a, b) Top and bottom view of HyA hydrogels printed by (a) the cold-stage method and (b) the direct writing method. (c) Cross-section view of the filament printed using the cold-stage method and direct writing method, and their respective aspect ratios post-printing. The aspect ratio is height/width ( $AR=H/W$ ). Data are mean  $\pm$  standard deviation ( $n=5$ ).

### 3.4 Discussion

To achieve the 3DP, we utilized tunable crosslinking densities and reversible solid-liquid phase transition of HyA hydrogels based on the thermodynamic and kinetic principles as well as the specific conditions that we identified. Specifically, we prepared HyA\_P by transitioning the solid HyA\_M phase to an injectable phase with a lower crosslinking density, and we stabilized the printed constructs by transitioning the injectable HyA\_P to a solid HyA\_H with a higher crosslinking density, under the specific conditions we revealed in this study. The thermodynamic principle explains the mechanism of the phase transition from HyA\_P to HyA\_H in DI water during the 3DP. Specifically, after immersing the printed constructs in DI water or directly printing HyA\_P into DI water, the  $\text{COO}^-$  concentration increased because the  $\text{Fe}^{3+}$  and  $\text{H}^+$  ions that were bonded onto the carboxyl groups decreased while the HyA concentration remained a constant. The ratio of bi- and tridentate carboxylate- $\text{Fe}^{3+}$  to carboxylate- $\text{H}^+$  coordination and the resulted crosslinking density of the hydrogel thus increased when  $[\text{Fe}^{3+}]/[\text{H}^+]$  is a constant, as shown in Equation (2.5b-2.7b).

The structural stability of HyA\_P highly determined the morphology and geometry of the printed constructs, especially when a cold-stage method was used, as demonstrated in this study. Unfortunately, when we prepare HyA\_P from HyA\_H and HyA\_M via reversing crosslinking, HyA\_P is usually in an intermediate state and has a crosslinking density between HyA\_M and HyA\_L, at which the crosslinking density will further decrease with the reaction time. Thus, the structural stability of HyA\_P decreased

with the reaction time, since the equilibrium state of this system is HyA<sub>L</sub>. This was confirmed by the results that HyA hydrogels printed on a cold stage had worse structural stability and the resulted shape changes were greater when they were kept in air for a longer time before immersed in DI water. The relationship between the coordination state and structural stability of the hydrogel suggests that when preparing HyA<sub>P</sub> reversed from HyA<sub>H</sub> and HyA<sub>M</sub>, it is important to select suitable Fe<sup>3+</sup> and H<sup>+</sup> ion concentrations which guarantee the equilibrium state of the hydrogel system is HyA<sub>P</sub>. For example, we can immerse HyA<sub>H</sub> or HyA<sub>M</sub> into innate FeCl<sub>3</sub> solution at the concentration of 30-50 mM, at which the equilibrium state of HyA gel is between the HyA<sub>M</sub> and HyA<sub>L</sub>, thus the HyA<sub>P</sub> will have relatively constant structural stability during the 3DP. Theoretically, it is also possible to directly crosslink the HyA to form partially crosslinked HyA<sub>P</sub>, that is, skipping the reverse phase transition from HyA<sub>M</sub> or HyA<sub>H</sub>. HyA solution with reduced pH will make the H<sup>+</sup> ions occupy the coordination sites first. After the addition of Fe<sup>3+</sup> ions, the Fe<sup>3+</sup> ions will need to replace the H<sup>+</sup> ions at the coordination sites and eventually achieve equilibrium. In this scenario, we only need to consider the thermodynamic factors, the exact pH of HyA solution and the concentration of FeCl<sub>3</sub> can be determined based on the results in Figures 2.3 and 2.4 and the relationship between crosslinking density and the concentrations of Fe<sup>3+</sup> and H<sup>+</sup> ion, as shown in Equation (2.5b-2.7b). For example, we can inject HyA solution with reduced pH directly to 5-30 mM FeCl<sub>3</sub> solutions, the final pH value of the hydrogel should be lower than the innate pH of the 5-30 mM FeCl<sub>3</sub> solutions but higher than the innate pH of 50 mM FeCl<sub>3</sub> solution. Theoretically, we can also directly print HyA solution with

reduced pH into 5-30 mM concentration range of FeCl<sub>3</sub> solution. It is difficult to directly print HyA solution with innate pH values into the FeCl<sub>3</sub> solution because the instant crosslinking of HyA hydrogel will prevent the bonding of printed filaments at the neighboring layers. However, when injecting HyA solution with a reducing pH into the FeCl<sub>3</sub> solution, a large amount of H<sup>+</sup> ions initially occupied the coordination sites would slow down the hydrogel crosslinking, which allows time for the printed filament to bond to one another in the layer-by-layer structure.

### **3.5 Conclusion**

This study successfully demonstrated 3DP of HyA hydrogels using the cold-stage method and direct writing method via controlling the dynamic coordination of Fe<sup>3+</sup> ions with the innate carboxyl groups on HyA chains, without adding other polymers or functional groups. Better structural stability of 3D constructs was achieved using the direct writing method.

## CHAPTER 4 Direct Writing of Hyaluronic Acid Solution in Fe<sup>3+</sup> Ion Solution

### 4.1 Introduction

In Chapter 3, 3D printing of HyA hydrogels was achieved by both cold-stage and direct writing methods via reversible phase transition. However, the lack of structural stability of 3D printing ink in the cold-stage method and undesired volume shrinkage that occurred during direct writing largely limited the application of these approaches, especially when 3D printing is time-consuming.<sup>53</sup> It is highly desirable to achieve the direct writing of HyA solution in Fe<sup>3+</sup> ion solution since this approach can increase the structural stability and reduce the volume shrinkage of 3D printed constructs. However, kinetically, Fe<sup>3+</sup> ions crosslink the HyA solution in a very short time, leading to rapid solidification of HyA solution in Fe<sup>3+</sup> ions. As a result, different layers printed in the Fe<sup>3+</sup> solution cannot form integrity. To achieve the direct writing of HyA solution in Fe<sup>3+</sup> ion solution, one strategy is to decelerate the crosslinking (or solidification) rate of HyA hydrogel. We hypothesized that the preloading of cations in HyA solution may slow down the crosslinking because it takes more time for Fe<sup>3+</sup> ions to replace these cations on the crosslinking sites than to react with the unoccupied carboxyl groups on the HyA molecular chains.

The direct writing of HyA solution in Fe<sup>3+</sup> ion solution can be used in the 3D printing of constructs with complex structures. For example, this strategy is promising in

the field of biofabrication, such as the bioprinting of tissues and organs with complex structures.

## **4.2 Materials and Methods**

### **4.2.1 Preload Cations in HyA Solution**

In this chapter, we used  $H^+$  and  $Ca^{2+}$  ions to occupy the crosslinking sites in the HyA solution. To preload  $H^+$  ions, HCl solutions at concentrations of 20, 40, 60, and 80 mM were prepared. HyA powders were then added to each HyA solution to form a 5 w/v% HyA solution. The HyA solution was mixed by dual asymmetric centrifugal (DAC 150.1 FVZ-K, FlackTek, Inc.) speedmixing at 2500 rpm for 5 minutes every 8 hours. It took 2-3 days for the solution to become uniform. These samples are named as H20, H40, H60, and H80. The preloading of  $Ca^{2+}$  ions followed the similar method described above,  $CaCl_2$  concentrations of 0.5, 1, 2, and 2.5 M were utilized in this study. The samples were named as Ca0.5, Ca1, Ca2, and Ca2.5. For HyA solution preloaded with  $H^+$  and  $Ca^{2+}$  ions, the samples had  $Ca^{2+}$  ion concentrations of 2 M and  $H^+$  ion concentrations of 20, 40, 60, and 80 mM. These samples were named as CH20, CH40, CH60, and CH80.

### **4.2.2 Measure the Rheological Properties**

The rheological properties of HyA solutions preloaded with cations were determined using a rheometer (MCR 92 with PP25 measuring system, Anton Paar). The gap between the bottom plane of the spindle and the stage was set as 1 mm. The storage modulus and loss modulus of the sample at different frequencies of 0.1-100 and at the constant shear strain of 1% were recorded at 25 °C. The storage modulus and loss

modulus of the sample was also measured at the different shear strain of 1%-1000% and at the constant frequency of 10. The ratios of storage modulus and loss modulus at different frequencies and shear strain were calculated and plotted. The viscosity of the sample at the shear rate of 0.1 1/s~100 1/s was recorded at 25 °C.

#### **4.2.3 Characterize the Chemical Bonding**

Fourier transform infrared spectroscopy-attenuated total reflection (FTIR-ATR, Nicolet iS10, ThermoFisher Scientific) was used to measure the transmittance of HyA solutions with and without the preloading of cations at the wavenumber of 4000-500  $\text{cm}^{-1}$ . Briefly, the sample was placed on the sample holder to cover the ATR crystal, and a metallic cap was then placed above the sample to prevent water evaporation. FTIR-ATR measurement was performed using the absorbance mode with 64 scans. After the measurement for each sample, the sample holder and the metallic cap were cleaned using DI water and then dried using a cotton swab to avoid cross-contamination between the samples.

#### **4.2.4 Determine the Direct Writing Capability of HyA Solution**

To determine the boundary conditions of cation loading on the direct writing capability, HyA solution preloaded with cations was printed to crossed filaments on the petri dish filled with 30 mM  $\text{FeCl}_3$  solution using a syringe with a needle of 0.84 mm. After 1 min, the  $\text{FeCl}_3$  solution was poured out of the petri dish. The filament on top of the crossed lines was peeled off by using a tweezer to see whether the two filaments were stuck or detached. The HyA solutions can be directly printed in the  $\text{FeCl}_3$  solution to form a 3D structure when their corresponding filaments can stick with each other.

#### **4.2.5 Determine the Boundary Condition of Reaction Time**

To determine the minimum reaction time that the  $\text{Fe}^{3+}$  ions can fully crosslink the HyA filaments, HyA solution was injected into  $\text{FeCl}_3$  solutions at different concentrations of 10-300 mM. After different reaction times, the crosslinked hydrogel filaments were lyophilized using the same method as described in chapter 2. The cross-section of these filaments was characterized using SEM, following the same method as described in chapter 2.

To determine the maximum reaction time that the crosslinked hydrogel filaments can retain their solid states, hydrogel filaments were prepared using the same method as described above. At different timepoint, these filaments were picked out of the  $\text{FeCl}_3$  solutions and were photographed using a camera. The reaction time was recorded once the solid-liquid phase transition occurred.

#### **4.2.6 Determine the Boundary Condition of pH of Water**

After the secondary crosslinking, 3D-printed constructs were immersed in water to form HyA\_H. To determine the boundary condition of pH of water that the 3D printed constructs can transform to HyA\_H, HyA\_M hydrogels were prepared using the method described in chapter 2 and then immersed in water with different pH value. The acidic water was prepared by adding HCl in DI water, while the alkaline water was prepared by adding ammonia hydroxide to the DI water. At the timepoints of 0, 0.25, 1, 2, and 24 h, the hydrogels were photographed using a camera.

#### **4.2.7 Demonstrate the Direct Writing of HyA Solution in FeCl<sub>3</sub> Solution**

To demonstrate the direct writing of HyA solution in FeCl<sub>3</sub> solution, HyA solution preloaded with 30 mM HCl and 2 M CaCl<sub>2</sub> was directly printed onto a petri dish (10 cm in diameter) containing 30 mM FeCl<sub>3</sub> solution. The architecture was changed by printing filaments with 0 and 90 angles between two successive layers. The injection pressure, speed of the printing head, nozzle size, and the distance between two neighbor filaments were set as 1~1.5 bar, 3~8 mm/s, 0.84 mm, and 2.3 mm, respectively. After printing, the printed gel was immersed in 300 mM FeCl<sub>3</sub> solution for 1 min, followed by in DI water for 24 hours. Optical images of both top and cross-sectional views of the printed sample were recorded using optical microscopy (SE303R-P, Amscope).

#### **4.2.8 Determine the Effects of HyA Concentration and FeCl<sub>3</sub> Solution Concentration on the Shrinkage Coefficient of HyA Hydrogels During Phase Transition**

HyA\_M discs with a diameter of 13 mm and thickness of 1 mm were prepared using a similar method as described in chapter 2. To determine the effects of HyA concentration on the shrinkage of hydrogels, 10%, 7.5%, and 5% HyA solutions and constant FeCl<sub>3</sub> solution concentration were utilized in the preparation. The as-prepared HyA\_M discs were then immersed in the DI water for 24 hours. The volume of the hydrogel before and after immersion was measured, and the volume shrinkage was calculated. To determine the effects of FeCl<sub>3</sub> solution concentration on the shrinkage of hydrogels, FeCl<sub>3</sub> solutions at the concentrations of 50, 100, 200, and 300 mM and a constant HyA concentration of 5% were utilized. The volume shrinkage was calculated using the same method as described above.

## 4.3 Results

### 4.3.1 Direct Writing of HyA Solution in FeCl<sub>3</sub> Solution

Figure 4.1a illustrates the status of HyA filaments crosslinked using FeCl<sub>3</sub> solution at different concentrations. As shown in Figure 3.3, HyA hydrogels exhibited the solid phase at equilibrium state when crosslinked using FeCl<sub>3</sub> solutions in the region I and showed liquid phase at equilibrium state when crosslinked using FeCl<sub>3</sub> solutions in region II. As shown in Figure 4.1a, the HyA solution will have a core-shell structure when crosslinked using FeCl<sub>3</sub> solutions in the region I. Specifically, a dense HyA hydrogel layer will form on the outer layer of the filament, and the hydrogel layer will prevent the diffusion of Fe<sup>3+</sup> ions towards the center of the filament, making the filament has a crosslinked shell and non-crosslinked core. When crosslinking the filaments using FeCl<sub>3</sub> solutions in region II, it is easier for the diffusion of Fe<sup>3+</sup> ions towards the center of the filament, and the whole structure will be crosslinked. The filaments will transform into a liquid state when extending the reaction time.

To achieve the Direct writing of HyA solution in FeCl<sub>3</sub> solution, the HyA solution should be printed into the FeCl<sub>3</sub> solutions in the region I to retain the solid states of the printed constructs. However, the rapid solidification of HyA solution in Fe<sup>3+</sup> ions will make the printed filaments fail to stick together, as shown in Figure 4.2. As shown in Figure 4.1b, when preloading cations in HyA solution to occupy the coordination sites, the crosslinking and solidification of HyA filaments may be delayed. The printed filaments may have enough time to react and stick with each other. Since the as-printed

structure will have a core-shell structure, a secondary crosslinking of printed constructs using  $\text{FeCl}_3$  solutions in region II is needed to fully crosslink the hydrogels.

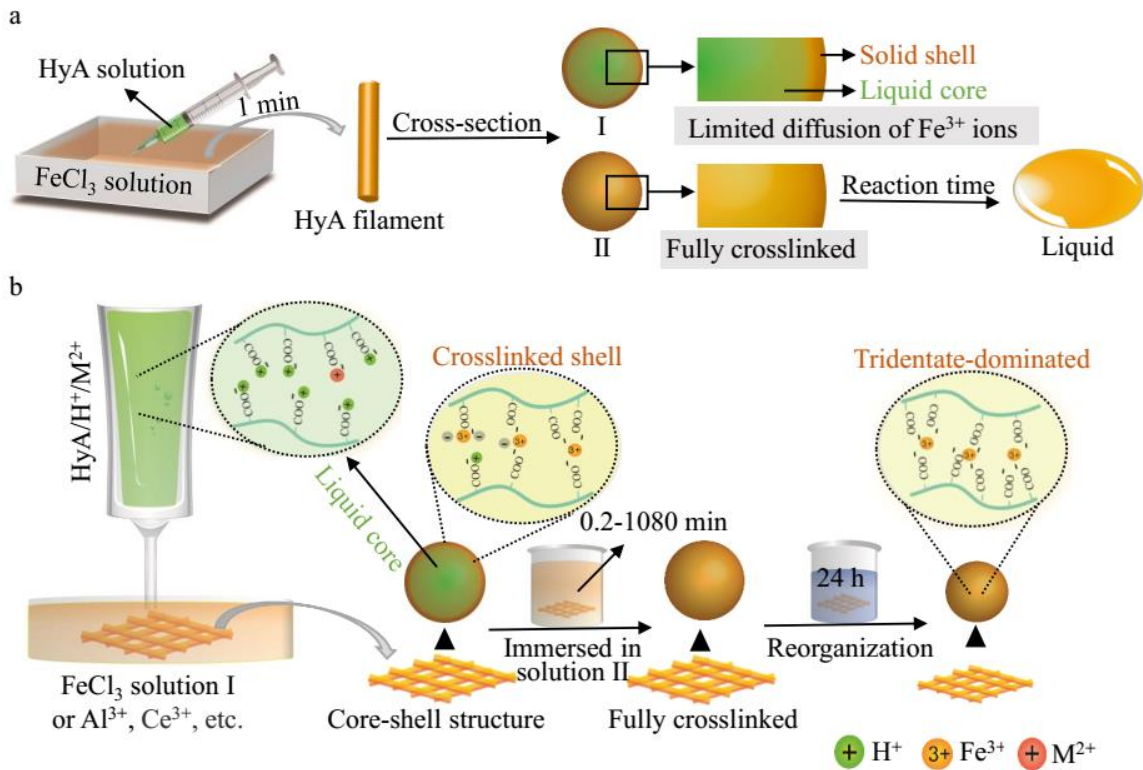


**Figure 4.1** Schematic diagrams showing direct writing of HyA solution in  $\text{FeCl}_3$  solution. (a) Crosslinking and phase transition of HyA hydrogels crosslinked using  $\text{FeCl}_3$  solution at different concentrations. (b) Procedures of directly writing HyA solution in  $\text{FeCl}_3$  solution.

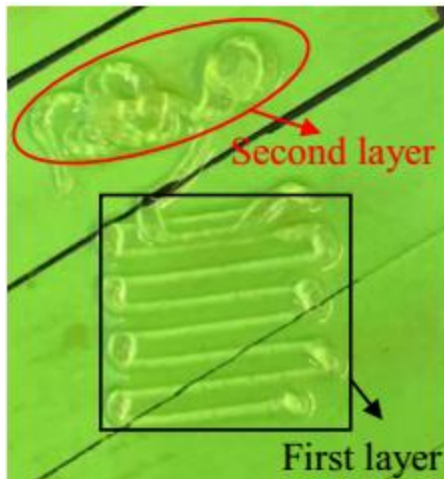


**Figure 4.2** Photograph showing HyA filaments prepared by direct writing of HyA solution in the  $\text{FeCl}_3$  solution.

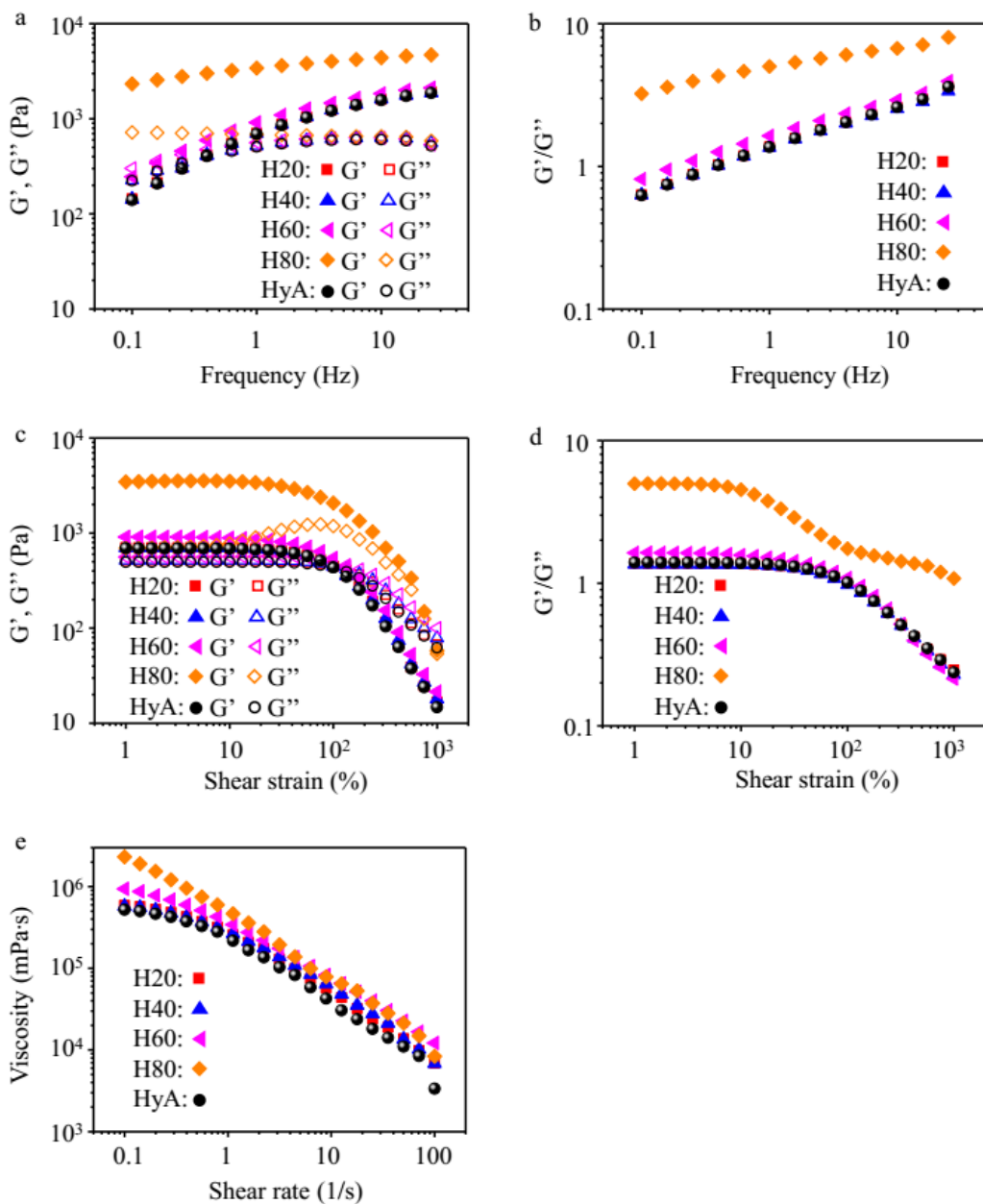
#### 4.3.2 Rheological Properties of HyA Solution Preloaded With Cations

Figure 4.3 shows the rheological properties of HyA solution preloaded with 20, 40, 60, and 80 mM HCl. As shown in Figure 4.3a and b,  $G'$  and  $G''$  of HyA solution preloaded with 20, 40, and 60 mM HCl and HyA control at different frequencies were similar, while HyA solution preloaded with 80 mM HCl exhibited significantly greater structural stability ( $G'/G''$ ). As shown in Figure 4.3c and d,  $G'$  and  $G''$  of HyA groups at different shear strains showed a similar trend as described above. HyA solution preloaded with 80 mM HCl also showed the highest viscosity among all the groups, as indicated in Figure 4.3e.

Figure 4.4 shows the rheological properties of HyA solution preloaded with 0.5, 1, 2, and 2.5 M  $\text{CaCl}_2$ . When the concentrations of  $\text{CaCl}_2$  were from 0.5-2 M, the  $G'$ ,  $G''$ , and viscosity of the HyA solution were similar. At the  $\text{CaCl}_2$  concentration of 2.5 M, all

the parameters significantly increased, indicating the crosslinking effects of  $\text{Ca}^{2+}$  ions at this concentration range.

Figure 4.5 shows the rheological properties of HyA solution preloaded with  $\text{Ca}^{2+}$  ion concentration of 2 M and  $\text{H}^+$  ion concentrations of 20, 40, 60, and 80 mM. Interestingly, all the HyA solutions loaded with cations exhibited similar  $G'$ ,  $G''$ , and viscosity.



**Figure 4.3** Rheological properties of HyA solution at different HCl concentrations. (a-b) Storage ( $G'$ ) and loss modulus ( $G''$ ) (a) and the ratio of  $G'/G''$  (b) of HyA solution at different frequencies. (c-d)  $G'$  and  $G''$  (c) and the ratio of  $G'/G''$  (d) of HyA solution at different shear strains. (e) The viscosity of HyA solution at different shear rates.

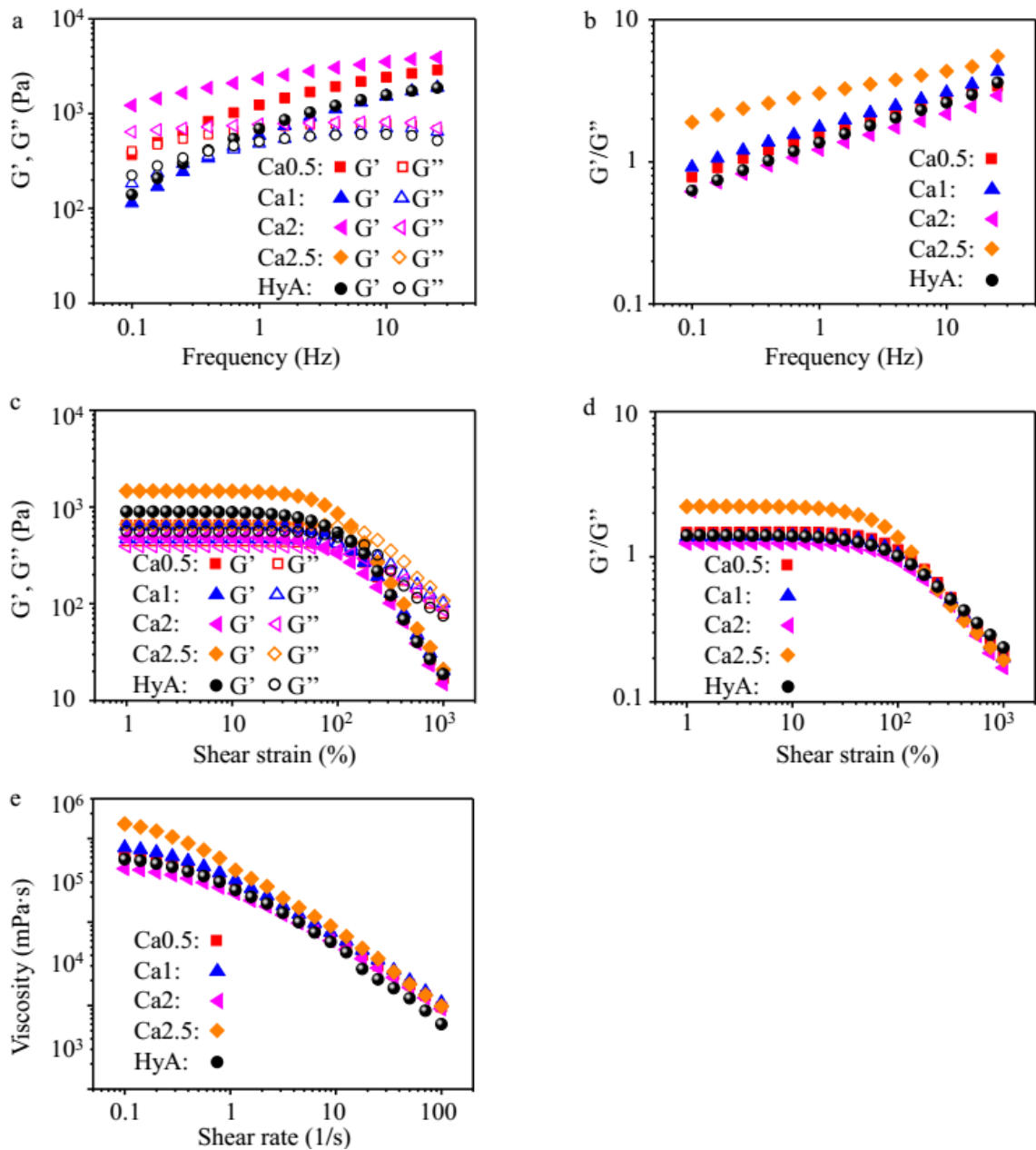


**Figure 4.4** Rheological properties of HyA solution at different CaCl<sub>2</sub> concentrations. (a-b) Storage ( $G'$ ) and loss modulus ( $G''$ ) (a) and the ratio of  $G'/G''$  (b) of HyA solution at different frequencies. (c-d)  $G'$  and  $G''$  (c) and the ratio of  $G'/G''$  (d) of HyA solution at different shear strains. (e) The viscosity of HyA solution at different shear rates.

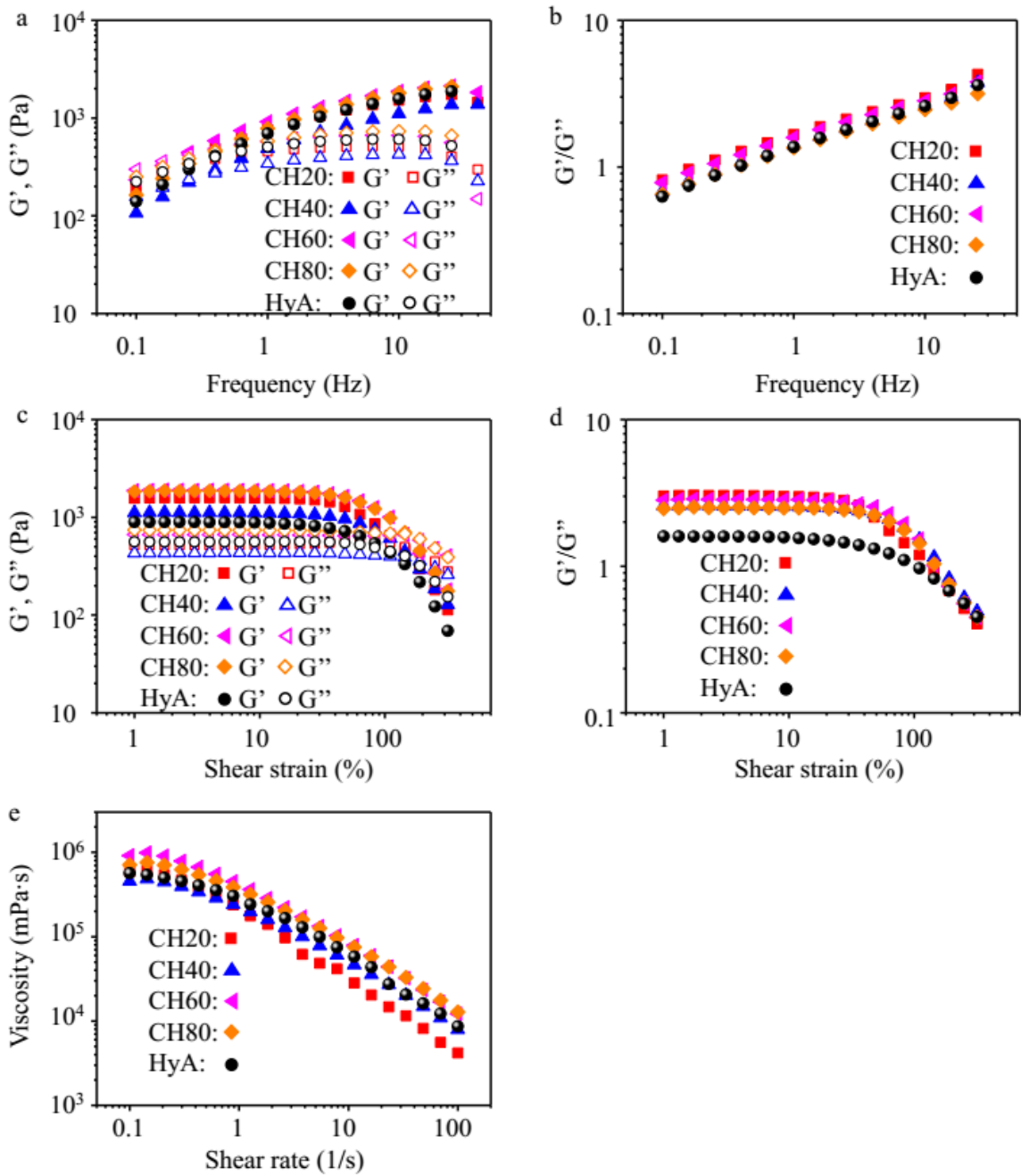


**Figure 4.5** Rheological properties of HyA solution at different HCl and CaCl<sub>2</sub> concentrations. (a-b) Storage ( $G'$ ) and loss modulus ( $G''$ ) (a) and the ratio of  $G'/G''$  (b) of HyA solution at the different frequencies. (c-d)  $G'$  and  $G''$  (c) and the ratio of  $G'/G''$  (d) of HyA solution at different shear strains. (e) The viscosity of HyA solution at different shear rates.

### 4.3.3 Direct Writing Capability of HyA Solution Preloaded With Cations

Figure 4.6 shows the FTIR-ATR spectra of HyA solution preloaded with different cations. When increasing the concentrations of  $H^+$  and  $Ca^{2+}$ , the characteristic peak for the carboxyl group switched toward the region with greater wavenumber, indicating the occupation of the crosslinking site by these cations. As shown in Figure 4.7, when loading with  $H^+$  or  $Ca^{2+}$  ions only, the injected hydrogel filaments cannot stick with each other, indicating the rapid solidification of HyA in  $FeCl_3$  solution. In the groups of HyA solution loaded with two types of cations, the injected filaments stuck together, indicating the 3D printing capability of these samples.

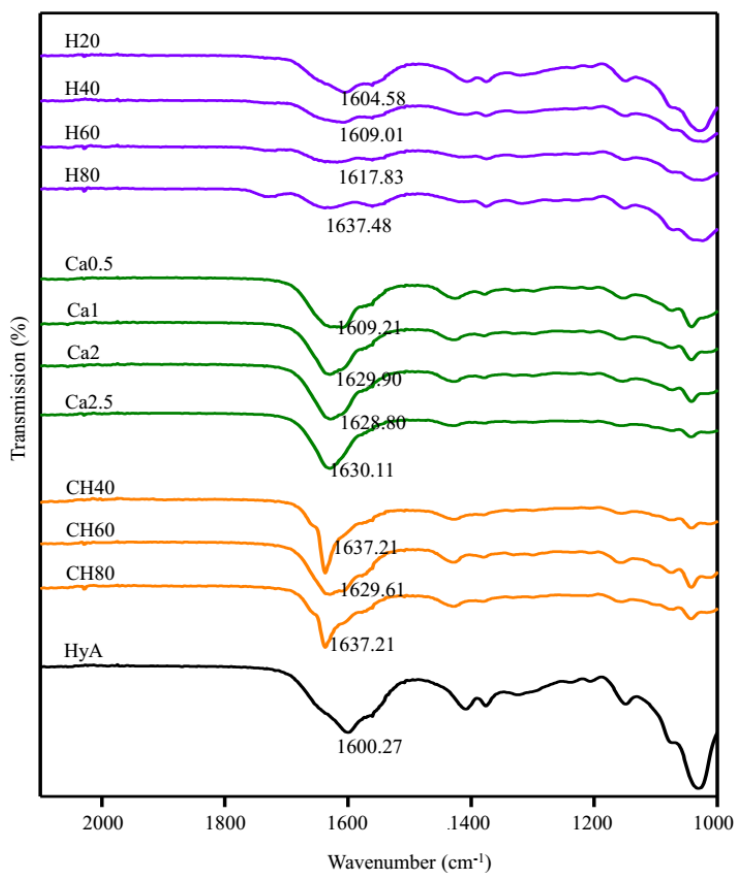


**Figure 4.6** FTIR-ATR spectra of HyA solution preloaded with different cations.

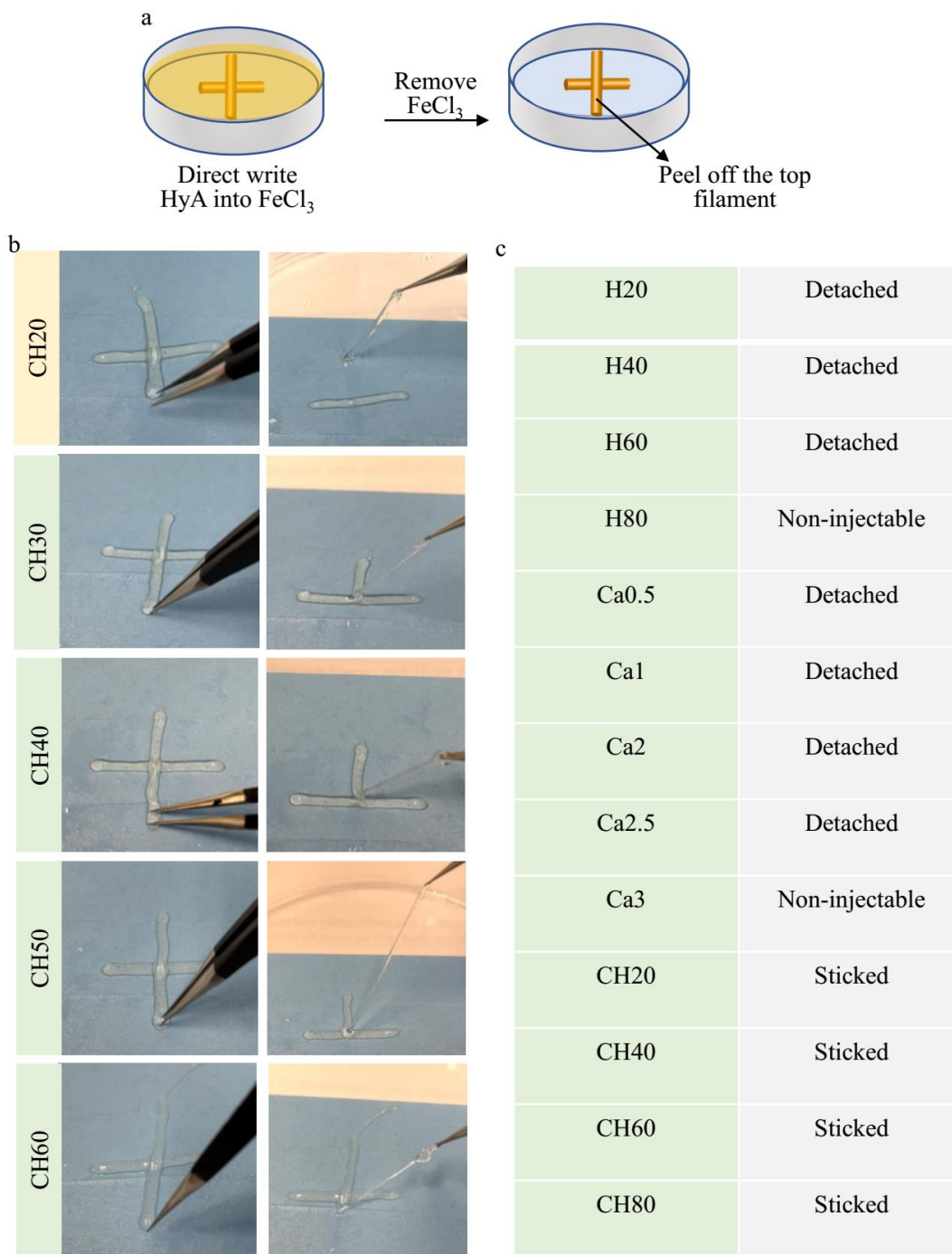


**Figure 4.7** Determination of direct writing capability of HyA solution preloaded with cations. (a) Illustration showing the direct writing of HyA filaments in  $\text{FeCl}_3$  solution. (b) Photographs showing the status of crossed filaments. (c) Status of the crossed filaments.

#### **4.3.4 Minimum and Maximum Reaction Time in Solution II**

As shown in Figure 4.8a, filaments crosslinked using 10-40 mM FeCl<sub>3</sub> solutions exhibited large pores, indicating the non-crosslinked core of the filament. As shown in Figure 4.8b, when crosslinking using FeCl<sub>3</sub> solutions at concentrations of > 50 mM, the morphology of the filament cross-sections changed from large pores to small pores over time, indicating the full crosslinking of the filament. Interestingly, when using FeCl<sub>3</sub> solutions at higher concentrations, it took a shorter time to fully crosslink the hydrogel filaments. Moreover, Figure 4.9 shows the photographs of hydrogel filaments crosslinked using FeCl<sub>3</sub> solutions at different concentrations for varied reaction times. The results indicated that when using FeCl<sub>3</sub> solutions at higher concentrations, the maximum reaction time that the filament can retain the solid phase becomes shorter. Figure 4.10 shows the quantitative data of minimum and maximum reaction time that the filament can be fully crosslinked but retain a solid state.

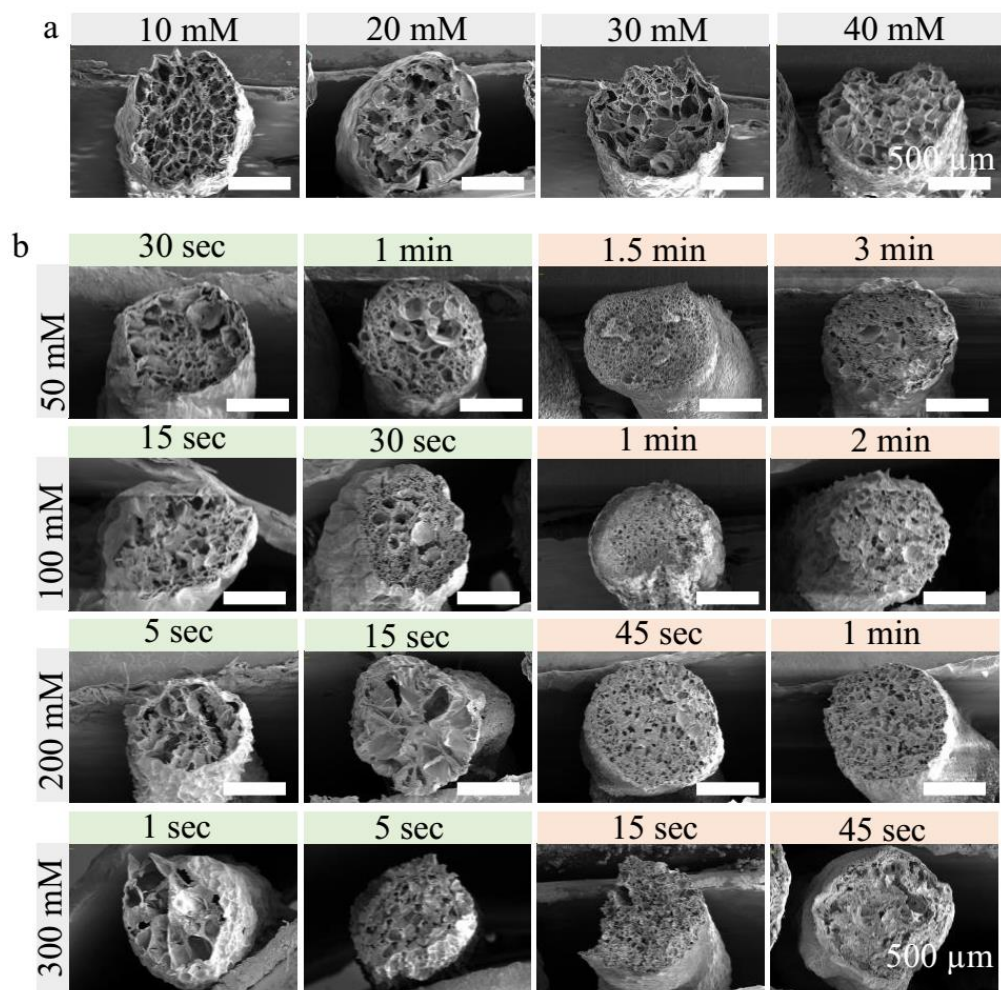


**Figure 4.8** Determination of FeCl<sub>3</sub> concentration and minimum reaction time. (a) Cross-sectional SEM images of HyA filaments crosslinked using FeCl<sub>3</sub> solution at concentrations of 10-40 mM. (b) Cross-sectional SEM images of HyA filaments crosslinked using FeCl<sub>3</sub> solution at concentrations of 50-300 mM for different reaction times.

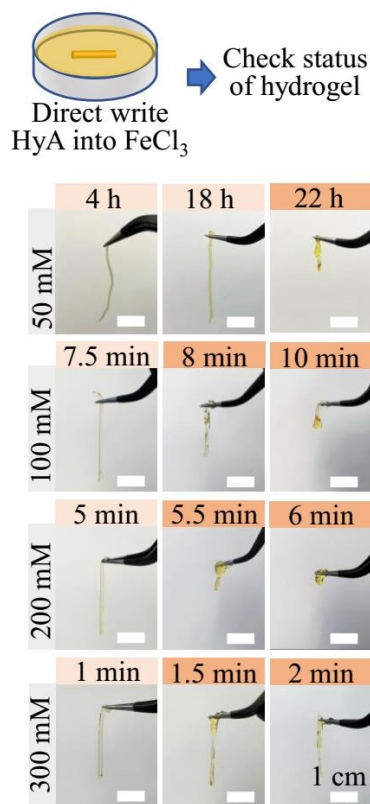


**Figure 4.9** Photographs showing the status of HyA filaments crosslinked using  $\text{FeCl}_3$  solution at the concentrations of 50-300 mM for different reaction times.

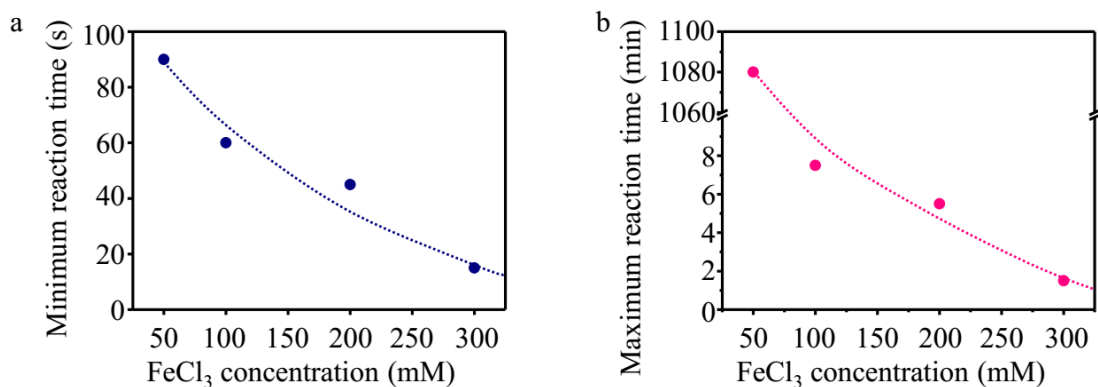


**Figure 4.10** Reaction time in the secondary crosslinking of HyA hydrogels. (a) The minimum reaction time of obtaining fully crosslinked HyA filaments using  $\text{FeCl}_3$  solution at the concentrations of 50-300 mM. (e) The maximum reaction time of retaining solid HyA filaments using  $\text{FeCl}_3$  solution at concentrations of 50-300 mM.

### 4.3.5 Effects of pH Value of Water

Figure 4.11 shows the photographs of HyA\_M samples in the water at different pH values over time. Specifically, when the pH values were from 1.3-2.5, the hydrogels gradually dissolved in the water, indicating their liquid phase at the equilibrium state. When the pH values ranged from 3-8, HyA\_M gradually transformed to HyA\_H, and the volume shrunk at the first hour of immersion. At the pH of 11, the samples became red, indicating the generation of  $\text{Fe}(\text{OH})_3$  under alkaline conditions.

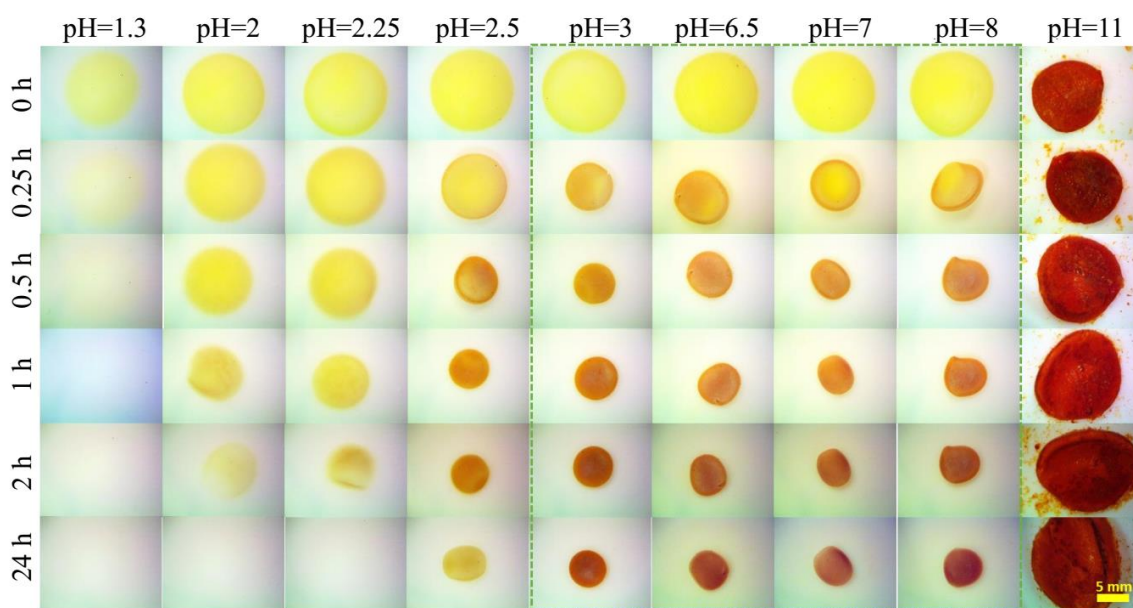


**Figure 4.11** Optical images showing the change of HyA hydrogels immersed in water with different pH values.

#### 4.3.6 Demonstration of Direct Writing of HyA Solution in FeCl<sub>3</sub> Solution

Figure 4.12 demonstrated the direct writing of HyA solution in FeCl<sub>3</sub> solution. As shown in the optical image, the printed filaments maintained their as-designed cylindrical shape although dramatic volume shrinkage occurred during the phase transition. The cross-section also exhibited that the 3D printed constructs had a layer-by-layer structure, indicating excellent structural stability during the 3D printing process.

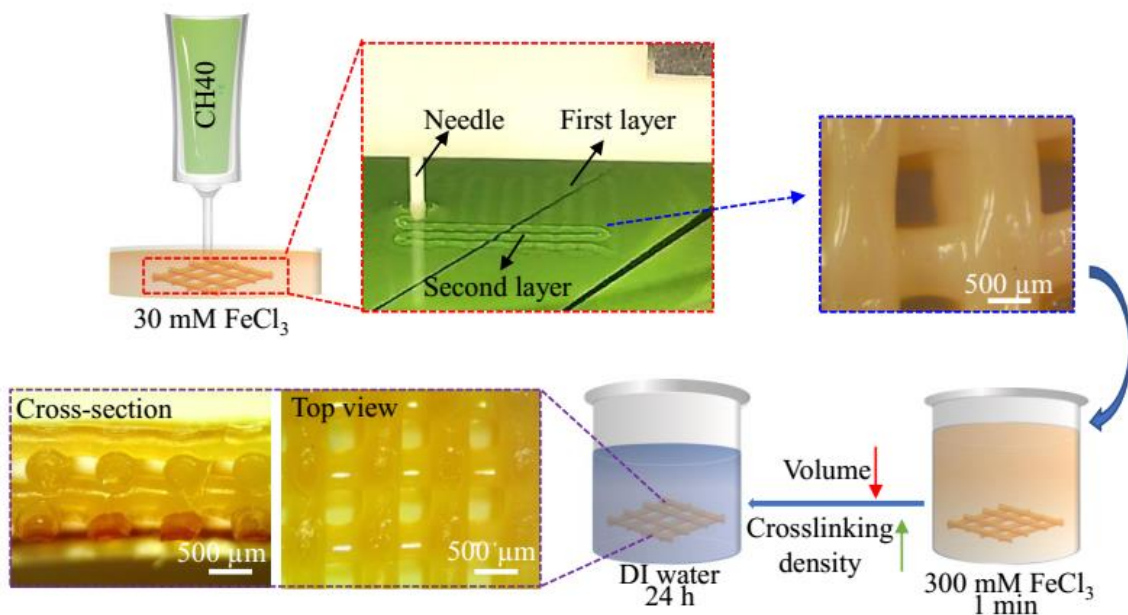


**Figure 4.12** Procedures of Direct writing of HyA solution in FeCl<sub>3</sub> solution and the optical images of printed HyA hydrogels.

#### 4.3.7 Effects of HyA Concentration and FeCl<sub>3</sub> Solution Concentration on the Shrinkage Coefficient of HyA Hydrogels During Phase Transition

Figure 4.13 shows the effects of HyA concentration and FeCl<sub>3</sub> solution on the shrinkage coefficient of HyA hydrogels during phase transition. The results indicated that the volume shrinkage dramatically decreased when using higher concentrations of HyA

solutions. Moreover, the HyA hydrogels exhibited similar volume shrinkage when the  $\text{FeCl}_3$  solutions were from 100-300 mM. The volume shrinkage significantly decreased when the  $\text{FeCl}_3$  solution of 50 mM was used to crosslink the hydrogel.

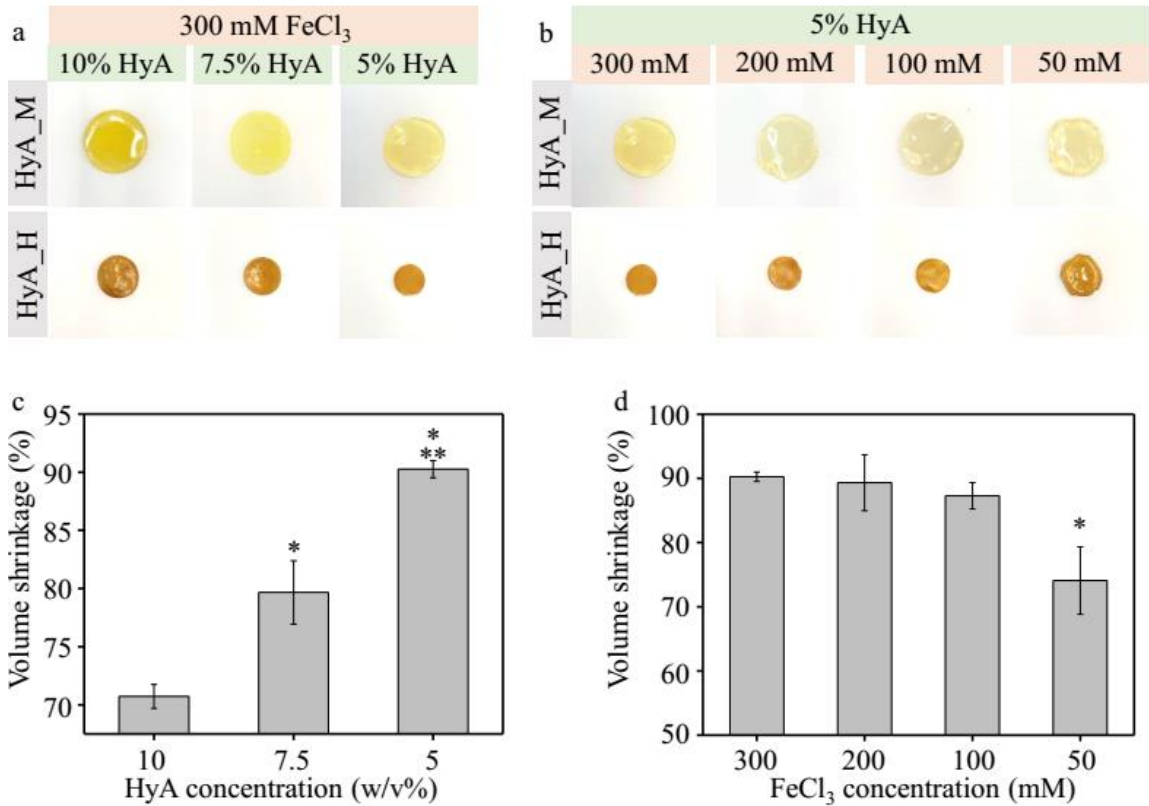


**Figure 4.13** 3D printing resolution enhancement via volume shrinkage. (a) Photographs showing the volume shrinkage of HyA hydrogels prepared using different concentrations of HyA solution. (b) Photographs showing the volume shrinkage of HyA hydrogels crosslinked using different  $\text{FeCl}_3$  concentrations. (c) Quantitative volume shrinkage of HyA hydrogels prepared using different concentrations of HyA solution. (d) Quantitative volume shrinkage of HyA hydrogels crosslinked using different  $\text{FeCl}_3$  concentrations.

#### 4.4 Discussion

Due to their low structural stability, hydrogel materials are relatively difficult to be 3D printed. Traditionally, hydrogels can be 3D printed into layer-by-layer structures on a substrate, and chemical modifications such as functionalization are usually inevitable.<sup>54-55</sup> In Recent years, several studies have reported the direct writing of hydrogels in aqueous solutions or soft gels.<sup>28, 53</sup> Compared to the hydrogel constructs prepared on a substrate, hydrogels printed in the solution or soft gel usually show better structural stability. This is because the buoyancy force applied on the 3D printed structure helps reduce the effects of gravity.

For the direct writing of hydrogels in the aqueous solution, it is very important to control their solidification rate. When the solidification process is slow, the 3D printed constructs may not retain their structural integrity during the 3D printing. When the solidification process is fast, the printed hydrogel filaments may not stick together to form integrity. There are many factors that may affect the solidification process of hydrogels in the aqueous solution, such as temperature, crosslinking agent, and hydrogel concentration. In this study, for the first time, I developed a strategy to slow down the solidification of hydrogels by pre-occupying the crosslinking sites on the polymers with cations. This method is versatile and can be applied to other hydrogels having carboxyl groups. Moreover, different cations can be used to serve as the preload ions, such as  $H^+$ ,  $Ca^{2+}$ ,  $Mg^{2+}$ ,  $Na^+$ ,  $Cu^{2+}$ , etc. In the future, different ions may be used to reduce the toxicity of the 3D printable HyA solutions.

## 4.5 Conclusion

For the first time, this study achieved the direct writing of HyA solution in  $\text{FeCl}_3$  solution via pre-occupying the crosslinking site of HyA molecules. Boundary conditions for achieving the 3D printing such as  $\text{FeCl}_3$  solution concentration and reaction time were determined. The resolution of 3D printing was dramatically enhanced via a novel volume shrinkage structure. The concentrations of HyA solution and  $\text{FeCl}_3$  solution influenced the shrinkage of HyA hydrogels during the phase transition. In the future, different polymers and cations may be used to reduce the toxicity of the material. This method is promising in printing complex structures, such as tissues and organs.

## CHAPTER 5 Cytocompatibility of Hyaluronic Acid Hydrogels Crosslinked via Dynamic Coordination of Innate Carboxyl Groups and Metallic Ions

### 5.1 Introduction

Different cell culture methods can be used to evaluate the *in vitro* cytocompatibility of biomaterials of interest for various aspects of applications *in vivo*. As shown in Figure 5.1, three *in vitro* culture methods, i.e., direct culture, direct exposure culture, and exposure culture, to mimic different *in vivo* scenarios where biodegradable implant materials are used inside the human body, are most commonly used.<sup>56</sup> The direct culture method is mainly used to evaluate the behavior of newly seeded cells directly adherent to and surrounding the implant materials. The direct exposure culture method mimics the *in vivo* scenario where the implant materials come into direct contact with the established cells and tissues. The exposure culture method can be used to show how the degradation products from the implant materials and changes in the local microenvironment can affect the established cells and tissues that are not directly in contact with the implant materials. To evaluate the cytocompatibility of biodegradable HyA hydrogels, the direct exposure culture method was utilized.

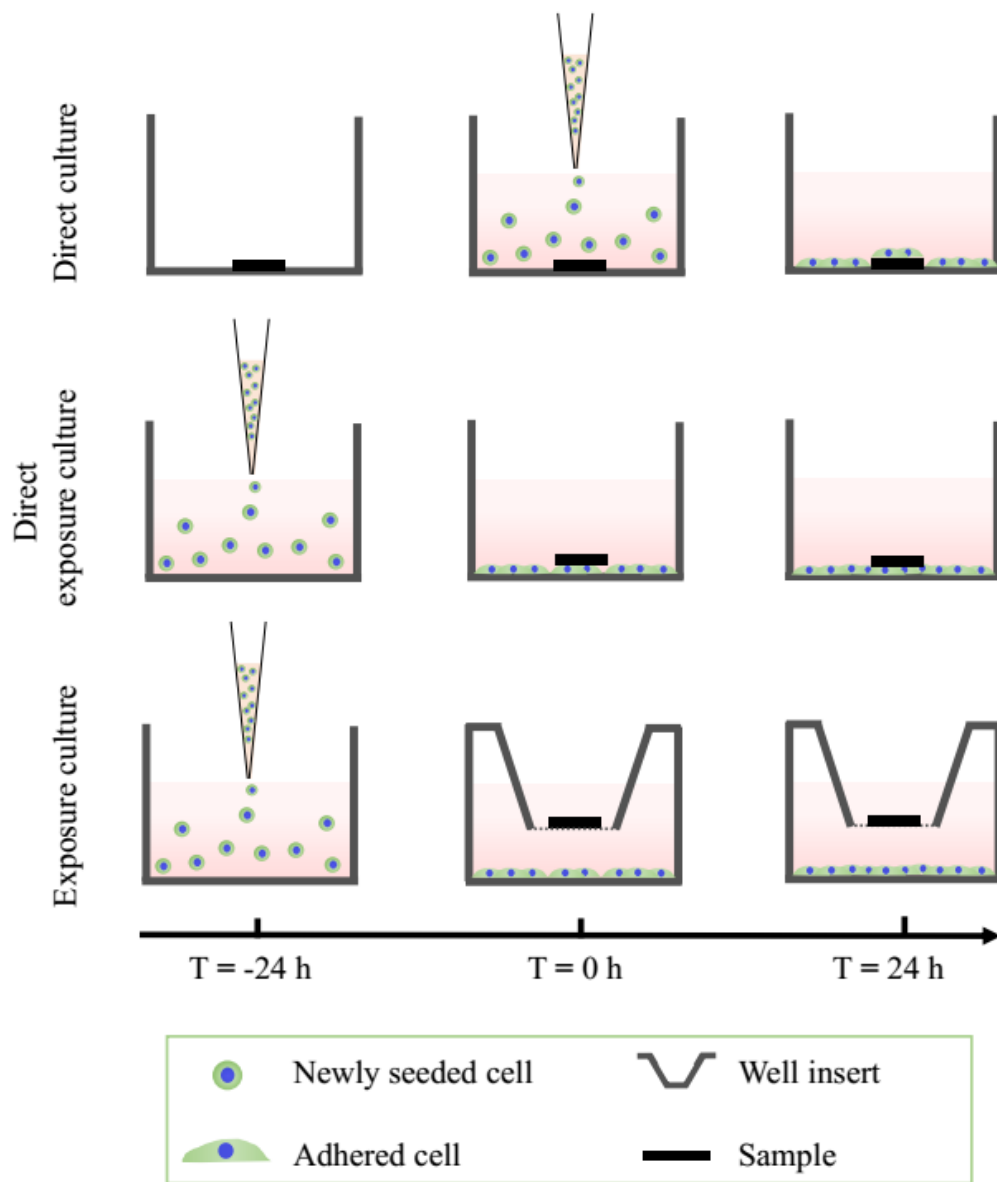


**Figure 5.1** Illustration showing three different cell culture methods to evaluate the cytocompatibility of biodegradable materials. This figure is adapted from<sup>56-57</sup>.

## 5. 2 Materials and Methods

### 5.2.1 Evaluate the Cytocompatibility of HyA Hydrogels With BMSCs in Direct Exposure Culture *in Vitro*

#### 5.2.1.1 Harvest and Culture BMSCs

Following the protocol approved by the Institutional Animal Care and Use Committee (IACUC) at the University of California at Riverside (UCR), rat BMSCs were harvested and cultured similarly as described in our previous work.<sup>56, 58-61</sup> Briefly, the distal and proximal ends of the femoral and tibial bones were dissected, and the bone marrow was flushed out of the bone cavity by Dulbecco's Modified Eagle Media (DMEM, #SLBC9050, high glucose, D5648, Sigma-Aldrich, St. Louis, MO) supplemented with 10% fetal bovine serum (FBS, HyClone, #SH30910, Thermo Fisher Scientific Inc., Waltham, MA) and 1% penicillin/streptomycin (P/S, HyClone, #SV30010, Thermo Fisher Scientific, Inc., Waltham, MA) using a syringe and collected in the centrifuge tube. Hereafter, the complete DMEM supplemented with 10% FBS and 1% P/S is referred to as the culture media in this study. The collected cells were filtered using a 70- $\mu$ m nylon strainer (Fisher Scientific, NH, USA) and then cultured in media under standard cell culture conditions (i.e., 37 °C, 5%/95% CO<sub>2</sub>/air, humidified, sterile environment) to 90-95% confluency. The descriptions for cell harvesting were reprinted (adapted) with permission from (Zhang, C.; Lin, J.; Nguyen, N.-Y. T.; Guo, Y.; Xu, C.; Seo, C.; Villafana, E.; Jimenez, H.; Chai, Y.; Guan, R. Antimicrobial Bioresorbable Mg–Zn–Ca Alloy for Bone Repair in a Comparison Study with Mg–Zn–Sr Alloy and Pure

Mg. ACS Biomaterials Science & Engineering 2019, 6 (1), 517-538). Copyright (2020) American Chemical Society.

#### *5.2.1.2 Prepare HyA Hydrogels and Controls for Cell Culture*

HyA powders were disinfected under ultraviolet (UV) radiation for 1 hour and DI water was sterilized by autoclaving. FeCl<sub>3</sub> (#169430010, Sigma-Aldrich, St. Louis, MO) was dehydrated in an oven at 120 °C for 30 min, weighed immediately afterward while it was still hot, and then dissolved in the sterilized DI water to prepare the 300 mM FeCl<sub>3</sub> solution. HyA hydrogel samples of 3D printed HyA\_H (HyA\_H\_3D), HyA\_H, HyA\_M, HyA\_P, and HyA\_L were prepared using similar methods as described in Chapter 2. Briefly, 2 mL of HyA solution at the concentration of 5 w/v% was manually printed onto a petri dish using a syringe with a 0.5 mm needle. The printed filament had no gaps and formed a uniform thin layer after 10 minutes in air at room temperature. After that, 10 mL of 300 mM FeCl<sub>3</sub> solution was added to the petri dish to crosslink the HyA layer. The HyA\_M was obtained after a 3-min reaction. The as-prepared HyA\_M film had a thickness of 0.47±0.06 mm and was punched into a cylindrical shape with a diameter of 12.17±0.15 mm. To produce HyA\_H, the as-prepared HyA\_M cylinders were immersed in sterilized DI water for 24 hours. The HyA\_H cylinders had a diameter of 5.43±0.12 mm and a thickness of 0.23±0.06 mm. To prepare HyA\_P and HyA\_L, 5 w/v% HyA solution was manually injected into the 300 mM FeCl<sub>3</sub> solution using a syringe with a 0.35 mm needle. The HyA\_P was produced after a 30-min reaction, while the HyA\_L was obtained after 1 hour of reaction.

We used the same volume and specific surface area of the HyA\_M, HyA\_P, and HyA\_L for the cell study. Different volumes or specific surface areas of the samples may affect the sample degradation rate and mode, and the contact area between cells and samples, which both may cause undesirable deviations in the cell study results. To ensure the HyA\_M, HyA\_P, and HyA\_L have similar volume and specific surface area, HyA\_P and HyA\_L were printed onto glass slides to form a cylindrical shape similar to HyA\_M. Briefly, the as-prepared HyA\_P and HyA\_L were manually printed onto sterilized glass slides (12 mm in diameter, LOT 18851, Fisher Scientific) using a syringe with a 0.5 mm needle. The printed hydrogel filaments had no gap and formed a uniform hydrogel layer completely covering one surface of the glass slides after 20 min in the air at room temperature. The uniform HyA\_L layer formed after 5 min in the air at room temperature. The hydrogel thicknesses on the glass slides were then measured to be  $0.63\pm 0.15$  mm for HyA\_P and  $0.47\pm 0.06$  mm for HyA\_L.

To prepare HyA\_H\_3D, the as-prepared HyA\_P was manually printed onto a petri dish using a syringe with a 0.5 mm needle to create a  $15\times 15$  mm network pattern with 225 repeating units of  $1\times 1$  mm square, and DI water was immediately added after printing. The 3D printed structure (HyA\_H\_3D) was obtained after immersing in DI water for 24 hours. The  $15\times 15$  mm network pattern was first drawn on a piece of paper placed under the transparent petri dish to serve as a guide during the printing. The filaments in the first layer were printed in parallel, and the orientation was defined as  $0^\circ$  angle. The filaments in the second layer were printed in parallel with an orientation of  $90^\circ$  angle to the first layer. The distance between the parallel filaments in both layers was

measured to be  $1.1\pm 0.34$  mm. The HyA\_H\_3D samples had two printed layers with an overall thickness of  $0.43\pm 0.15$  mm. To ensure the HyA\_H\_3D and HyA\_H samples contained a similar amount of hydrogel, the 3D printed constructs were cut to a cylindrical shape with a diameter of  $5.6\pm 0.17$  mm.

The respective HyA solution and  $\text{Fe}^{3+}$  ion solutions were both included as control groups in the cell study. Specifically, 1 mg/mL HyA in the cell culture media was used as the HyA control. To prepare the HyA control, 3 mg of HyA powders (equivalent to the amount of HyA in a single HyA hydrogel sample) was added into each culture well containing 3 mL of media.  $\text{FeCl}_3$  solutions at the concentrations of 2.09 mM and 6.08 mM were used as the  $\text{Fe}^{3+}$  ion control groups, to represent the low and high  $\text{Fe}^{3+}$  ion contents in the HyA hydrogels with high to low crosslinking densities. The HyA\_H sample had the lowest  $\text{Fe}^{3+}$  ion content among all the hydrogel groups because most of the free  $\text{Fe}^{3+}$  ions in the hydrogel network were released to DI water during the phase transition from HyA\_M to HyA\_H. HyA\_L had the highest  $\text{Fe}^{3+}$  ion content among all the hydrogel groups because it absorbed the highest amount of  $\text{FeCl}_3$  solution in its network and had the lowest crosslinking density. The  $\text{Fe}^{3+}$  solution at the concentration of 2.09 mM was used as a control to represent the low  $\text{Fe}^{3+}$  ion concentration in the media when all  $\text{Fe}^{3+}$  ions in a HyA\_H sample were completely released and dissolved in the media. The  $\text{Fe}^{3+}$  solution at the concentration of 6.08 mM was used as a control to represent the high  $\text{Fe}^{3+}$  ion concentration in the media when all  $\text{Fe}^{3+}$  ions in a HyA\_L sample were completely released and dissolved in the media. The amount of  $\text{Fe}^{3+}$  ions in HyA\_H and HyA\_L samples were measured using ICP-OES. We first dissolved the

respective HyA\_H and HyA\_L samples in 10 mL of 2 wt.% nitric acid. The 2 wt.% nitric acid was used as the solvent because it serves as a cleaning agent for ICP-OES and it can completely dissolve the crosslinked hydrogels to release all the Fe<sup>3+</sup> ions into the solution. The nitric acid solutions containing the dissolved Fe<sup>3+</sup> ions from HyA\_H and HyA\_L were then diluted with DI water at a dilution factor of 1:500 and fed into the autosampler of ICP-OES, similarly as described in Section 2.3.

#### *5.2.1.3 Direct Exposure Culture of BMSCs With HyA Hydrogels*

The direct exposure culture method was used to determine the cytocompatibility of HyA hydrogels with BMSCs, as established in the previous publication.<sup>59</sup> Briefly, BMSCs were seeded into each well of a 12-well plate with a seeding density of 10,000 cells/cm<sup>2</sup>. The cells in each well were cultured in 3 mL of media under standard cell culture conditions for 24 hours to form a monolayer of adherent cells. Before any samples were added, the optical micrographs of the cells were captured using an optical microscope (Eclipse Ti and NIS software, Nikon, Melville, NY, USA). Afterward, the media and non-adhered cells were removed from each well, and the cells were rinsed using a phosphate-buffered solution (PBS) three times. For HyA and Fe<sup>3+</sup> ion control groups, 3 mL of fresh culture media containing 1 mg/L HyA, 2.09 mM Fe<sup>3+</sup> ions, or 6.08 mM Fe<sup>3+</sup> ions were added to each respective well. For all the crosslinked HyA groups, the respective samples HyA\_H\_3D, HyA\_H, HyA\_M, HyA\_P, and HyA\_L were added on top of the adherent cells, as well as the fresh culture media. To ensure direct contact between the cells and the samples, a sterile glass slide was placed on top of each sample of HyA\_H\_3D, HyA\_H, and HyA\_M to prevent the samples from floating during the cell

culture. The HyA\_P and HyA\_L samples were flipped over and placed directly on top of the cell layer since they were prepared on the glass slides. The glass slides were also included in the cell studies and referred to as the Glass control group, even though they were merely used to hold the samples in place and should not affect the results of the cell studies. A group consisted of BMSCs cultured in the media without any samples served as a positive control, and referred to as the Cell group. The group containing the culture media only without any cells or samples served as a blank reference, and referred to as the Media group. Upon adding the samples, the photographs of each well were captured using a camera, and the pH values of the media were measured using a pre-calibrated pH meter (Symphony, Model SB70P, VWR). The BMSCs were then cultured with the samples for 24 hours under the standard cell culture conditions.

#### *5.2.1.4 Determine BMSC Morphology and Adhesion Density After 24-Hour Direct Exposure Culture With HyA Hydrogels*

After the prescribed direct exposure culture of cells with samples, the photographs of each well were captured using a camera. The glass slides were removed from each well using a tweezer after photographing, and the post-culture media were then collected in the respective 15-mL centrifuge tubes for further analysis. BMSCs attached on the well-plates were rinsed with PBS three times and fixed with 4% formaldehyde (10% neutral buffered formalin; VWR, Radnor, PA, USA) for 20 min. The fixed BMSCs were rinsed using PBS three times and stained with Alexa Flour 488-phalloidin (A12379, Life technologies) for F-actin for 20 min. The stained cells were then rinsed using PBS three

times and stained with 4',6-diamidino-2-phenylindole dilactate (DAPI, Invitrogen) for nuclei for 5 min. After that, the cells were rinsed with PBS three times before imaging.

The BMSCs directly under the samples, that is, in direct contact with the sample, were referred to as the cells in direct contact conditions. In contrast, the BMSCs attached on the culture plate surrounding each sample without direct contact with the samples were referred to as the cells of indirect contact conditions. The stained BMSCs were imaged using a fluorescence microscope (Eclipse Ti and NIS software, Nikon, Melville, NY, USA). The micrographs of cells under direct and indirect contact conditions were also captured using an optical microscope (Eclipse Ti and NIS software, Nikon, Melville, NY, USA). DAPI-stained nuclei with normal morphology were counted to determine cell adhesion density per unit area. For each group, at least five fluorescence images of BMSCs under direct contact conditions and five fluorescence images of BMSCs under indirect contact conditions were used for cell counting and statistical analyses.

#### *5.2.1.5 Analyze the pH Value, the Concentrations of $Fe^{3+}$ and $Ca^{2+}$ Ions, and Hydrogel Degradation in the Culture Media*

The pH values of post-culture media were measured using a pre-calibrated pH meter (Symphony, Model SB70P, VWR) immediately after collection. The concentrations of  $Fe^{3+}$  and  $Ca^{2+}$  ions in the post-culture media were measured using ICP-OES similarly as described in Section 2.3 and 2.6.1. Specifically, the post-culture media were centrifuged at 5000 revolutions per minute (RPM) for 3 min to separate the solid from the liquid. The supernatant of the media was collected and diluted with DI water. To

measure the  $\text{Fe}^{3+}$  ion concentration, the dilution factor of 1:100 was used for the crosslinked HyA groups, and the dilution factor of 1:3 was used for the control groups of HyA, Glass, Cell, and Media. To measure  $\text{Ca}^{2+}$  ion concentration, a dilution factor of 1:100 was used for all the groups. After dilution, the samples were placed on the autosampler for ICP-OES measurement.

Photographs of the samples in the culture media before ( $T=0$  h) and after the prescribed 24-h incubation ( $T=24$  h) were captured using a camera. Photographs of the collected post-culture media containing degradation products from the samples were also taken using a camera.

## **5.2.2 Evaluate the Cytocompatibility of HyA Hydrogels Prepared via Direct Writing of HyA Solution in $\text{FeCl}_3$ Solution**

### *5.2.2.1 Prepare Samples for Cell Culture*

To prepare 3D printed HyA samples, HyA solution (CH30) was printed into 30 mM  $\text{FeCl}_3$  solution to create a cylindrical structure with a diameter of 13 mm and a thickness of two layers. The needle size was 0.84 mm, and the gap between filaments was 2 mm. The filaments in the first layer were printed in parallel, and the orientation was defined as  $0^\circ$  angle. The filaments in the second layer were printed in parallel with an orientation of  $90^\circ$  angle to the first layer. The printed constructs were subjected to a secondary crosslinking in 300 mM or 50 mM  $\text{FeCl}_3$  solution for 1 min, followed by immersing in DI water for 24 hours. Samples crosslinked using 300 mM and 50 mM  $\text{FeCl}_3$  solution were named as HyA\_300 and HyA\_50, respectively. HyA solution ink (CH30) was included in the cell study as a control group, the weight of CH30 in each

well was 0.113 g, which is consistent with the weight of CH30 used to print one 3D sample. Fe<sup>3+</sup> ion control, HyA control, and cell-only reference were also included, following the same method as described in 5.2.1.

#### *5.2.2.2 Cell Culture and Post-Culture Analysis*

The cell culture and analysis of cells and post-culture media followed the same method described in 5.2.1.

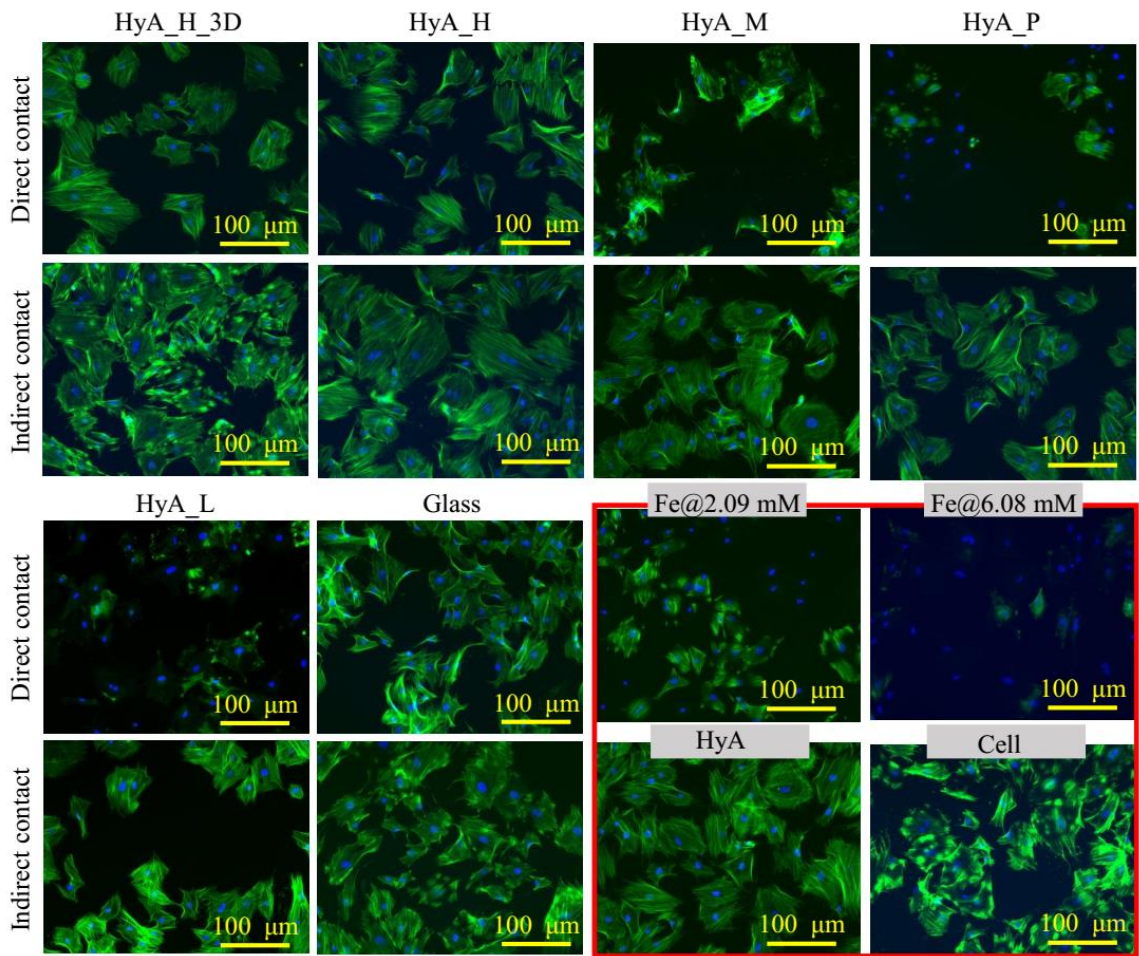
### **5.3 Results**

#### **5.3.1 Cytocompatibility of HyA Hydrogels With BMSCs in Direct Exposure Culture *in Vitro***

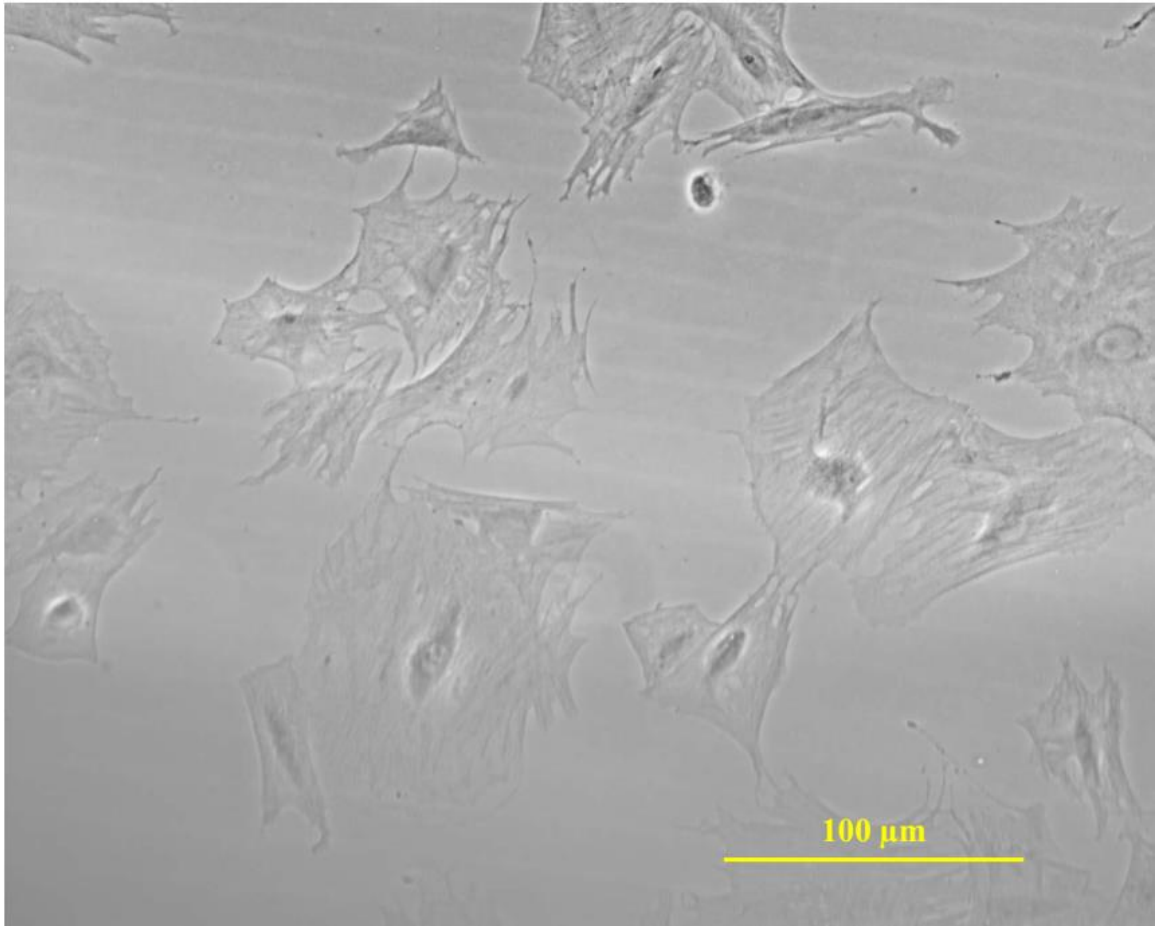
##### *5.3.1.1 BMSC Morphology and Adhesion Density After Direct Exposure Culture With HyA Hydrogels*

Figure 5.2 shows the representative fluorescence images of BMSCs directly in contact with the samples (i.e., direct contact) and BMSCs adhered on the culture plate surrounding the respective samples (i.e., indirect contact) after the 24-hour direct exposure culture. The fluorescence images show that the groups of HyA\_H\_3D and HyA\_H had more cells than the groups of HyA\_M, HyA\_P, and HyA\_L, under both direct and indirect contact conditions. For all hydrogel groups, the number of cells under indirect contact conditions was greater than the cells in direct contact conditions. Interestingly, for some cells under direct contact conditions in the groups of HyA\_M, HyA\_P, and HyA\_L and some cells in the groups of Fe@2.09 mM and Fe@6.08 mM, their fluorescence images show the DAPI-stained cell nuclei clearly, but not the

phalloidin-stained cytoskeleton. We speculated that  $\text{Fe}(\text{OH})_3$  may have precipitated on the cells in the groups of HyA\_M, HyA\_P, HyA\_L, and Fe@6.08 mM that had higher  $\text{Fe}^{3+}$  ion contents than other groups, which possibly interfered the Alexa Flour 488-phalloidin stain from entering the cells to bind with the cytoskeleton. Alexa Flour 488-phalloidin has a larger molecular weight of 1320 Da than the DAPI of 457.5 Da (molecular weight data was from the vendor), which may explain why the fluorescence of nuclei was observed but fluorescence of cytoskeleton was missing in some cells. As shown in Figures S4 and S5, the BMSCs all exhibited normal morphology with visible cytoskeleton on the culture plate before (Figure 5.3) and after the 24-hour direct exposure culture (Figure 5.4). The cells in the groups of HyA\_M, HyA\_P, HyA\_L, and Fe@6.08 mM with higher  $\text{Fe}^{3+}$  ion contents still showed normal morphology, indicating that the missing F-actin fluorescence signals in some cells is likely caused by the staining process of Alexa Flour 488-phalloidin.



**Figure 5.2** Representative fluorescence images of BMSCs directly in contact with the samples (direct contact) and on the culture plate surrounding each corresponding sample (indirect contact) after a 24-hour culture. Scale bar =100 μm for all images.



**Figure 5.3** Optical image of the cells adhered on the culture plate before adding any samples, that is, the cells at time zero ( $T=0$ ).

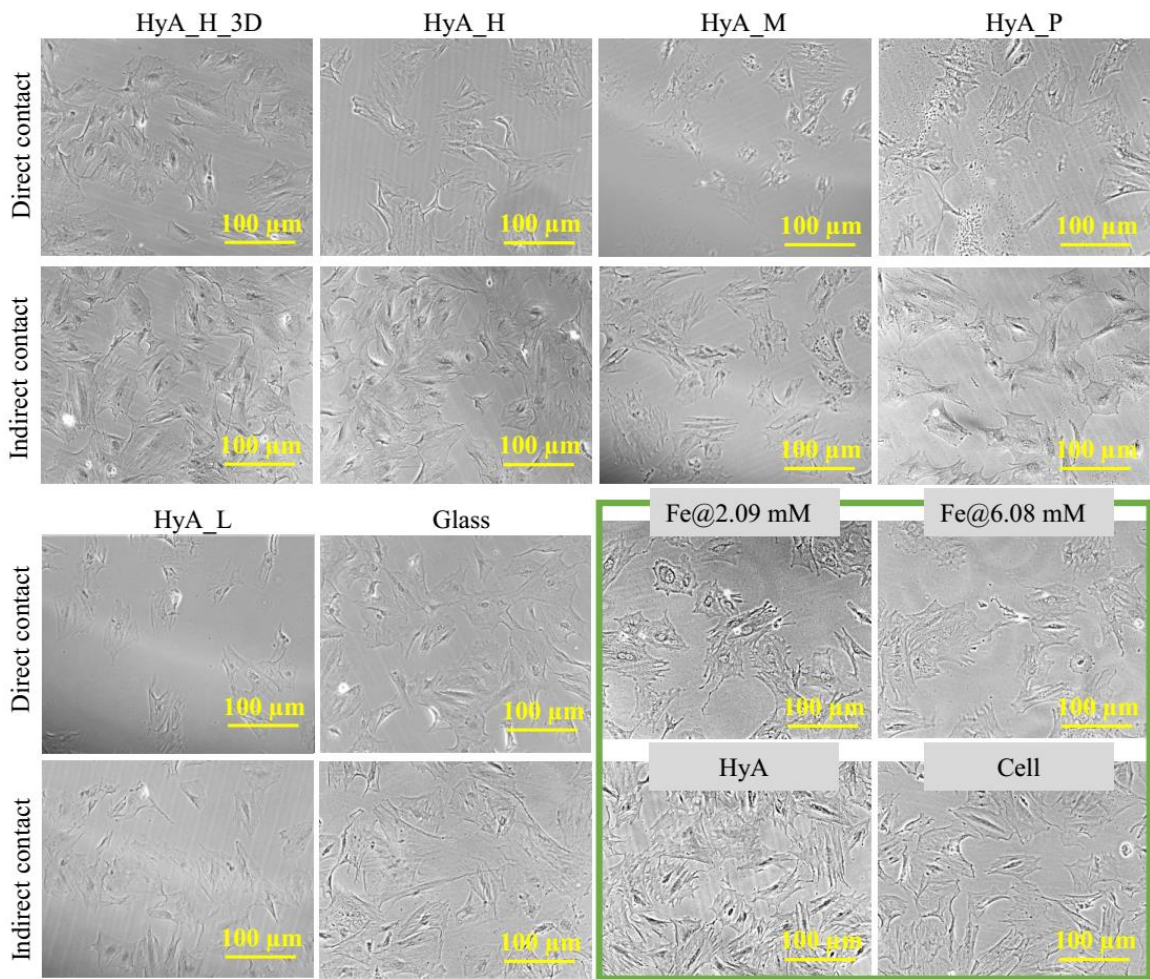


**Figure 5.4** Representative optical images of BMSCs directly in contact with the samples (direct contact) and cells on the culture plate surrounding each corresponding sample (indirect contact) after 24-hour direct exposure culture. Scale bar =100  $\mu\text{m}$  for all images.

Figure 5.5 shows the quantitative BMSC adhesion density in the cultures with different hydrogel samples and control groups. In average, the 3D printed HyA\_H (HyA\_H\_3D) and HyA\_H showed higher cell adhesion densities than the HyA\_M, HyA\_P, and HyA\_L hydrogel groups, under both direct and indirect contact conditions, and only HyA\_H\_3D showed statistically higher cell adhesion density than the groups of HyA\_M, HyA\_P, and HyA\_L under direct contact conditions. For all hydrogel groups of

HyA\_H\_3D, HyA\_H, HyA\_M, HyA\_P, and HyA\_L, cell adhesion densities in direct contact conditions were statistically lower than the same groups under indirect contact conditions. When the cells were in direct contact conditions, the cell adhesion densities for all crosslinked hydrogel groups were significantly lower than HyA control of  $8123 \pm 429$  cells/cm<sup>2</sup> and Cell control of  $8002 \pm 477$  cells/cm<sup>2</sup>. When the cells were under indirect contact conditions, only HyA\_M, HyA\_P, and HyA\_L had statistically lower cell adhesion densities than the control groups of HyA and Cell. Moreover, the cell adhesion densities of HyA and Cell control groups were similar, and both values were statistically higher than Fe<sup>3+</sup> ion control groups of Fe@2.09 mM and Fe@6.08 mM. Thus, we attribute the lower cell adhesion densities in the crosslinked hydrogel samples than the Cell control to the Fe<sup>3+</sup> and H<sup>+</sup> ions released from these samples.

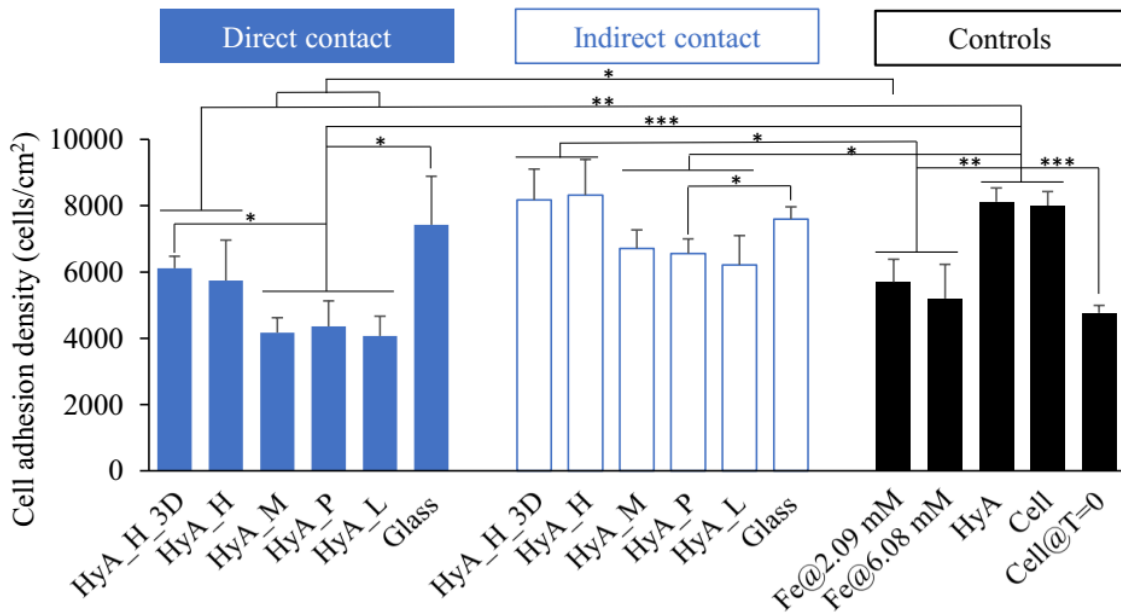


**Figure 5.5** BMSC adhesion densities under direct and indirect contact conditions in the groups of HyA\_H\_3D, HyA\_H, HyA\_M, HyA\_P, HyA\_L, and Glass, and in the control groups of Fe@2.09 mM, Fe@6.08 mM, HyA, and Cell. Data are shown as mean  $\pm$  standard deviation (n=3); \*p<0.05, \*\*p<0.01, \*\*\*p<0.001.

### 5.3.1.2 HyA Degradation, pH Values, and Fe<sup>3+</sup> and Ca<sup>2+</sup> Ion Concentrations in the Culture Media

After 24 hours of cell culture, solid HyA\_H\_3D and HyA\_H samples with tridentate-dominant coordination and solid HyA\_M samples with a mixed coordination of mono-, bi-, and tridentate bonding all lost their structural integrity in the media (Figure 5.6), and some hydrogel fragments were observed in the media (as highlighted in the dashed circles in Figure 5.7), which indicated partial solid-liquid phase transition.

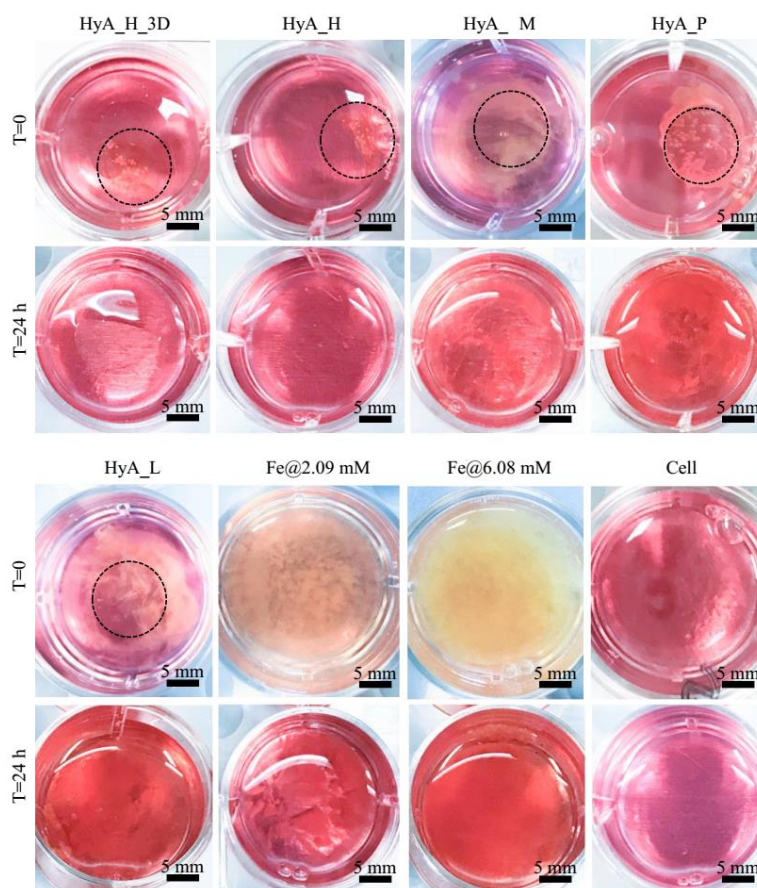


**Figure 5.6** Photographs of the samples in the culture media before (T=0) and after (T=24) the prescribed 24-h incubation. The dashed circles indicate the samples in the media. The brightness and contrast of the images were adjusted to highlight the samples in the media. Scale bar=5 mm for all images.

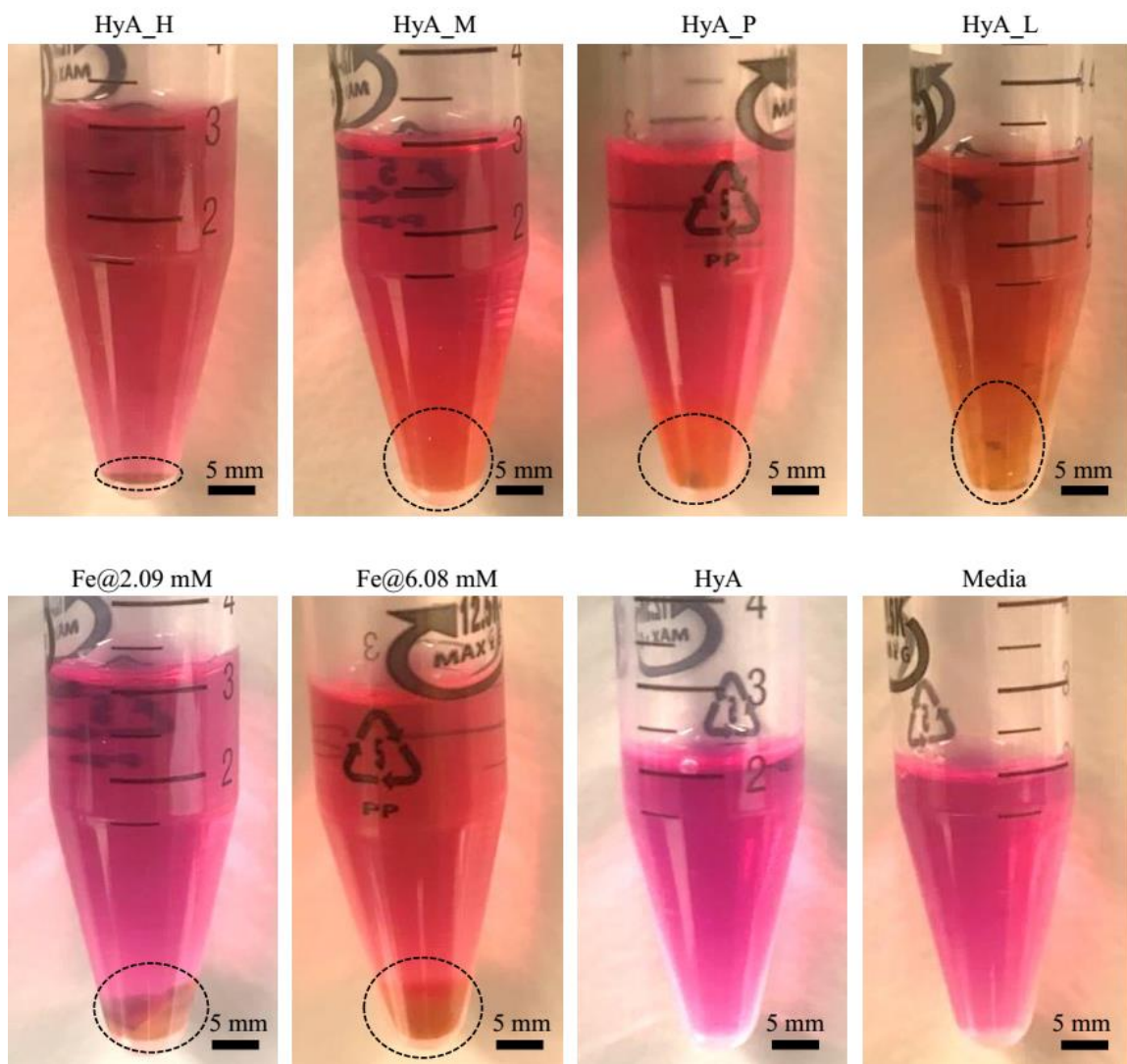


**Figure 5.7** Photographs of the collected media containing visible degradation products from the samples. Dashed circles are used to indicate the degradation products. Scale bar=5 mm for all images.

The changes in the pH values and ion concentrations of the media can significantly affect cell behavior. As shown in Figure 5.8a, upon adding the samples into BMSC culture, the pH values of the media for HyA\_M, HyA\_P, HyA\_L, Fe@2.09 mM, and Fe@6.08 mM were in a range of 6.77-7.30, which were statistically lower than the groups of HyA\_H, HyA, Glass, and Media with the pH values in a narrow range of 7.72-7.77. In average, the pH values of the media in HyA\_M, HyA\_P, HyA\_L, Fe@2.09 mM, and Fe@6.08 mM were lower than HyA\_H\_3D with a value of 7.62, even though no statistical difference was detected. After the prescribed 24-h incubation, the pH values of the media for all the groups except Fe@6.08 mM were in a narrow range of 7.85-7.93, even though statistical significances were found between some groups. Figure 5.8c shows the Fe<sup>3+</sup> concentrations in the post-culture media with different samples and controls. The Fe<sup>3+</sup> concentrations in the culture with HyA\_H\_3D and HyA\_H groups were significantly lower than HyA\_M, HyA\_P, HyA\_L, and Fe@6.08 mM groups, but statistically higher than the control groups of Fe@2.09 mM, HyA, Glass, Cell, and Media. Figure 5.8d shows the Ca<sup>2+</sup> concentration in the post-culture media for different groups. The groups of HyA\_M, HyA\_P, HyA\_L, Fe@2.09 mM, and Fe@6.08 mM showed statistically lower Ca<sup>2+</sup> concentrations than any other groups, possibly because of the Ca<sup>2+</sup> adsorption effects of Fe(OH)<sub>3</sub>. It has been reported that Al(OH)<sub>3</sub> and Fe(OH)<sub>3</sub> can adsorb cations such as Ca<sup>2+</sup> and Cd<sup>2+</sup> via ionic interactions,<sup>62</sup> and the groups of HyA\_M, HyA\_P, HyA\_L, Fe@2.09 mM, and Fe@6.08 mM had higher Fe<sup>3+</sup> ion contents and more Fe(OH)<sub>3</sub> precipitant formed in the media than the other groups.

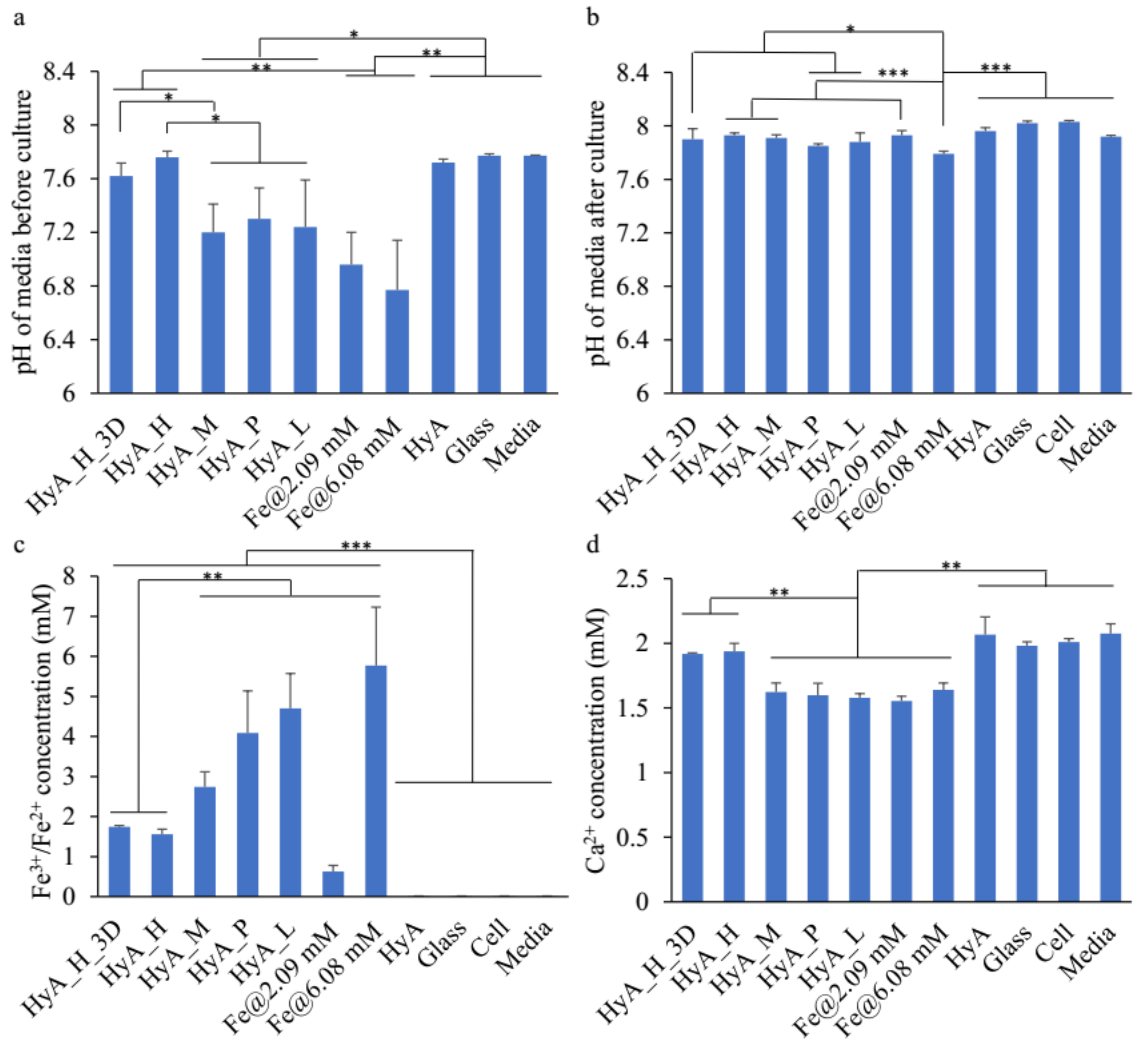


**Figure 5.8** The media analysis for HyA degradation and associated changes in the BMSC culture. (a) The pH values of media when the samples were added (T=0 h). (b) The pH values of media after 24 hours of culture with the samples (T=24 h). (c, d) The concentrations of Fe<sup>3+</sup> and Ca<sup>2+</sup> ions in the media at T=24 h. Data are shown as mean ± standard deviation (n=3); \*p<0.05, \*\*p<0.01, \*\*\*p<0.001.

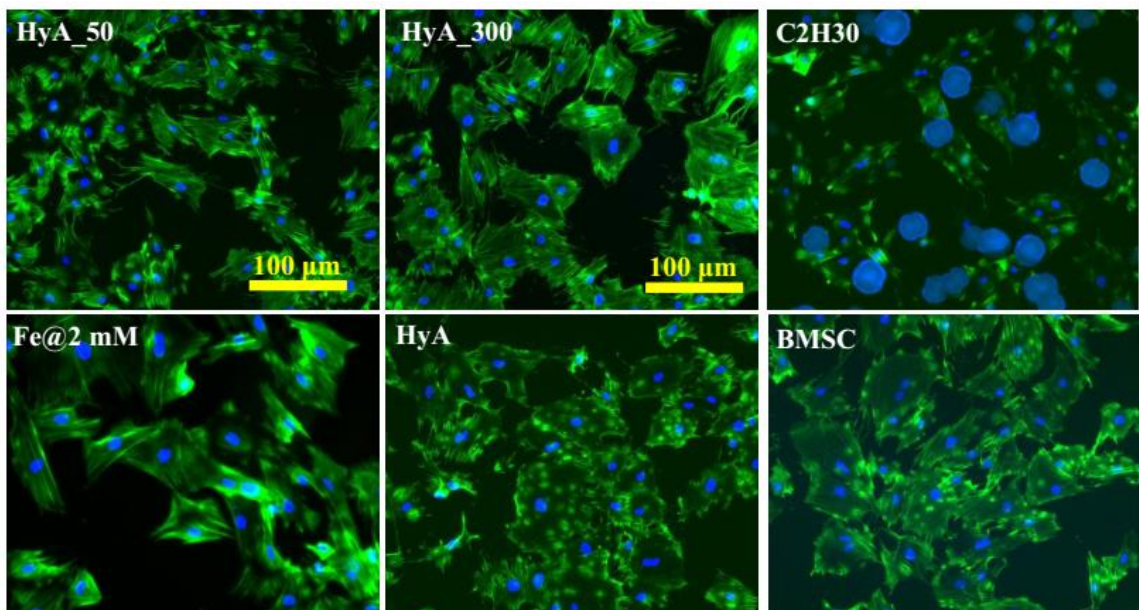


**Figure 5.9** Representative fluorescence images of BMSCs cultured with HyA hydrogels crosslinked via direct writing of HyA solution in  $\text{FeCl}_3$  solution after a 24-hour direct exposure culture. Scale bar = 100  $\mu\text{m}$  for all images

### 5.3.2 Cytocompatibility of HyA Hydrogels Prepared via Direct Writing of HyA

#### Solution in $\text{FeCl}_3$ Solution

##### 5.3.2.1 BMSC Morphology and Adhesion Density

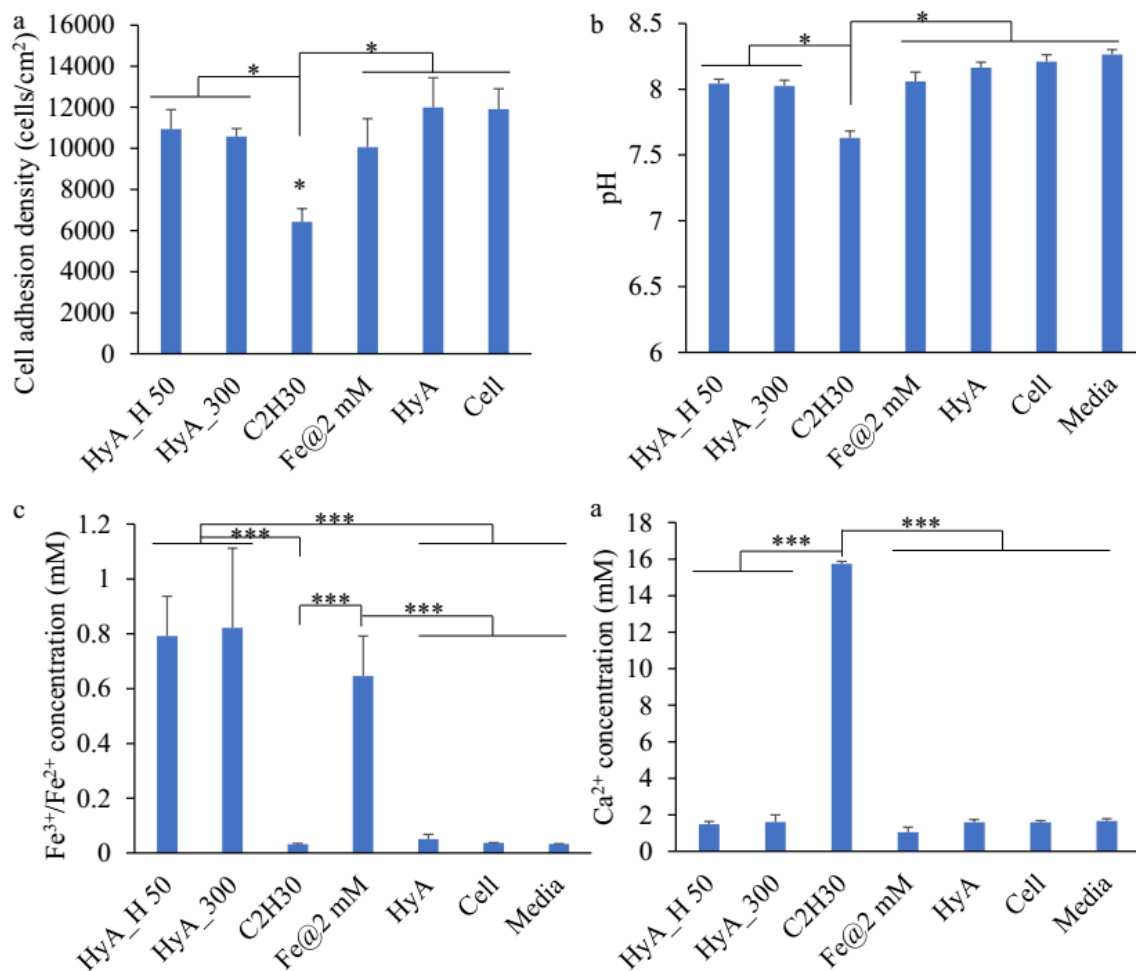
Figure 5.9 shows the representative fluorescence images of BMSCs adhered on the culture plate after the 24-hour direct exposure culture. The fluorescence images show that BMSCs in all the groups except CH30 had normal morphology compared to BMSC-only reference. For the group of CH30, large blue dots were observed, indicating the leakage of DNA from the cell nuclei. This may be attributed to the high concentrations of  $\text{H}^+$  and  $\text{Ca}^{2+}$  ions in the sample.

Figure 5.10a shows the quantitative BMSC adhesion density after 24 hours of direct exposure culture. The groups of CH30 showed statistically lower cell adhesion

density than all other groups, and no statistical difference was detected between any other groups.

#### *5.3.2.2 Post-Culture Media Analysis*

As shown in Figure 5.10b, the pH values in the media of all the groups except CH30 were in a small range of 8-8.25. Due to the high concentration of  $H^+$  ions, the pH in the CH30 group was statistically lower than in other groups. As expected, the groups of HyA hydrogel and  $Fe^{3+}$  ion control groups exhibited statistically higher  $Fe^{3+}$  ion concentration than other groups, as shown in Figure 5.10c. No other statistical difference was observed between the other groups. As shown in Figure 5.10d, the group of CH30 exhibited higher  $Ca^{2+}$  concentration than other groups, and no other statistical difference was observed between other groups.



**Figure 5.10** Cytocompatibility of HyA hydrogels printed via direct writing. (a) Quantitative BMSC adhesion density in different experimental and control groups. (b) pH value of post-culture media. (c) Iron ion concentration of post-culture media. (d) Ca<sup>2+</sup> concentration of post-culture media.

## 5.4 Discussion

### 5.4.1 Phase Transition of HyA Hydrogels in Cell Culture Environment

Kinetically, environmental factors such as the concentrations of other cations in the culture media could affect the rate of phase transition, that is, the time needed for a complete reversible phase transition. For example, the solid-liquid phase transition may not be complete within the time limit of 24-hour cell culture. Similar to  $H^+$  ions, multiple metallic ions, such as  $Ca^{2+}$ ,  $Mg^{2+}$ ,  $Na^+$ , and  $K^+$  ions can also bond to the carboxyl groups of HyA molecule and replace the tridentate or bidentate carboxylate- $Fe^{3+}$  coordination, thus decreasing the crosslinking density of hydrogels during the cell culture. After the 24-hour cell culture, the HyA hydrogels lost their structural integrity and dispersed in the media, which confirmed the decrease in crosslinking density of hydrogels and partial solid-liquid phase transition. Meanwhile, visible degradation products of the hydrogel samples in the post-culture media suggested that the solid-liquid phase transition were not completed in 24 hours of culture; that is, tridentate and bidentate coordination bonding was still present and not fully transitioned to the monodentate-dominant coordination state (Figures 5.6 and 5.7). Collectively, our results in Figure 2.5 confirmed that the solid-liquid phase transition of the HyA hydrogels could be fully reversible under the specific conditions, while Figures 5.6 and 5.7 suggested the solid-liquid phase transition in the cell culture condition may take longer than 24 hours to complete, because other cations in the culture media could affect the reaction kinetics.

#### **5.4.2 Strategies on Addressing the Toxicity Concern of Fe<sup>3+</sup> and H<sup>+</sup> Ions in the Crosslinked HyA Hydrogels**

The toxicity concern for our crosslinked HyA hydrogels is mainly related to the Fe<sup>3+</sup> and H<sup>+</sup> ions released. The pH values of the culture media should be neutralized quickly because of the bicarbonate buffering system in the media, as shown in Figures 5.8a and 5.8b. Similarly, Wetteland et al<sup>63</sup> reported the effects of cell culture media (DMEM) on neutralizing the changes in pH values caused by MgO and Mg(OH)<sub>2</sub> in an immersion study. However, before the hydrogel samples lost their structural integrity and became dispersed in the media, the region close to the samples would have a higher Fe<sup>3+</sup> concentration and lower pH values than the region farther away from the samples, because of the dynamic gradient of Fe<sup>3+</sup> and H<sup>+</sup> concentrations around the samples. As a result, the cells directly in contact with the samples and in a region closely surrounding the samples were exposed to higher Fe<sup>3+</sup> concentration and lower pH values than cells farther away from the samples. This explains why cell adhesion densities in direct contact conditions were significantly lower than the same samples under indirect contact conditions for all crosslinked hydrogel groups, as shown in Figure 5.5.

Fe<sup>3+</sup> ions have shown dosage-dependent toxicity to cells<sup>64</sup> and organs.<sup>65</sup> In mammals, iron is one of the essential elements and up to 25% is in the form of Fe<sup>3+</sup> ions.<sup>66</sup> For example, when the Human CD4<sup>+</sup> T cells were cultured in media at the adjusted Fe<sup>3+</sup> ion concentrations of 0 mM, 0.05 mM, 0.5 mM, 1 mM, and 5 mM, significant apoptosis levels of the cells were shown in the group of 5 mM Fe<sup>3+</sup> ion after 48-h culture.<sup>64</sup> In another example, when the rats were exposed to the drinking water at

the  $\text{Fe}^{3+}$  ion concentrations of  $\geq 0.87$  ppm (0.016 mM) for 100 days, the enzyme activity of the glutathione system in the rat liver was significantly affected, indicating hepatotoxicity due to iron overdose.<sup>65</sup> In our *in vitro* studies with BMSCs, the  $\text{Fe}^{3+}$  and  $\text{H}^+$  concentrations in the crosslinked HyA hydrogels have not yet been optimized. In the future, we will reduce the  $\text{Fe}^{3+}$  and  $\text{H}^+$  ion concentrations in the crosslinked HyA to minimize their toxicity concern for medical applications, while retaining the tunable crosslinking, reversible phase transition, and 3D printing capability. Specifically, according to our Equation 2.5b-2.7b, we can reduce  $\text{Fe}^{3+}$  concentrations and control the  $[\text{Fe}^{3+}]/[\text{H}^+]$  ratio to tune the crosslinking density.

Alternatively, some monovalent metal ions ( $\text{M}^+$ ) can be used to replace  $\text{H}^+$  ions at the coordination sites to eliminate the toxicity concern on excess  $\text{H}^+$  ions. Theoretically, some monovalent metal ions ( $\text{M}^+$ ) can bond to the carboxyl groups on HyA to form monodentate coordination like  $\text{H}^+$ . That is, the tunable ratios of mono-, bi-, and tridentate coordination and the resulted low-to-high crosslinking densities of the hydrogels can be achieved via the competition between  $\text{Fe}^{3+}$  and  $\text{M}^+$  ions (instead of  $\text{H}^+$  ions) at the coordination sites. In this case, the concentrations of  $\text{Fe}^{3+}$  and  $\text{M}^+$  ions and the reaction time can be used to control the ratios of mono-, bi-, and tridentate carboxylate- $\text{Fe}^{3+}$  coordination and the resulted crosslinking densities. The reaction equilibrium constant ( $K_M$ ) of the carboxylate-  $\text{M}^+$  is defined below:

$$K_M = \frac{[\text{M}^+\text{COO}^-]}{[\text{M}^+][\text{COO}^-]} \quad (5.1)$$

Equation (5.1a) is derived from Equation (5.1) to show the ratio of bonded to free carboxyl groups.

$$\frac{[M^+COO^-]}{[COO^-]} = [M^+]K_M \quad (5.1a)$$

When we combine Equation (2.5-2.7) and Equation (5.1), we can obtain Equation (5.2-5.4) to show the concentration ratio of mono-, bi-, and tridentate carboxylate-Fe<sup>3+</sup> coordination to carboxylate-M<sup>+</sup> coordination. The tunable ratios of mono-, bi-, and tridentate coordination and the resulted low-to-high crosslinking densities of this new hydrogel system with M<sup>+</sup> is expected to follow the thermodynamic and kinetic principles in Equation (5.2-5.4).

$$\frac{[Fe^{3+}COO^-]}{[M^+COO^-]} = \frac{K_1}{K_M} \cdot \frac{[Fe^{3+}]}{[M^+]} \quad (5.2)$$

$$\frac{[Fe^{3+}(COO^-)_2]}{[M^+COO^-]} = \frac{K_2}{K_M} \cdot \frac{[Fe^{3+}]}{[M^+]} \cdot [COO^-] \quad (5.3)$$

$$\frac{[Fe^{3+}(COO^-)_3]}{[M^+COO^-]} = \frac{K_3}{K_M} \cdot \frac{[Fe^{3+}]}{[M^+]} \cdot [COO^-]^2 \quad (5.4)$$

Critically, K<sub>M</sub> should be in an appropriate range, such as 10<sup>3</sup>-10<sup>5</sup>. When the reaction equilibrium constant (K<sub>M</sub>) is too small, such as <10, a high concentration of the monovalent metal ion is required to achieve the solid-liquid phase transition, which would raise the toxicity concern of the crosslinked hydrogels for medical applications. In contrast, when the reaction equilibrium constant is too high, such as >10<sup>40</sup>, the crosslinked hydrogels would be irreversible. In the future, monovalent metal ions with appropriate reaction equilibrium constant will be explored to eliminate the acidity concern induced by H<sup>+</sup> ions.

### 5.4.3 Prospects of HyA Hydrogels Crosslinked via Carboxylate-Fe<sup>3+</sup> Coordination for Biomedical Applications

The HyA hydrogel crosslinked via dynamic carboxylate-Fe<sup>3+</sup> coordination is promising for a wide range of biomedical applications. In this dissertation, we revealed not only the basic principles but also the practical conditions to achieve tunable crosslinking densities and reversible solid-liquid phase transition for HyA. Considering that these principles can be applied to many other polymers and hydrogels with carboxyl groups, our strategies can be used to create diverse hydrogels with specific properties for many applications. As we discussed above, the toxicity concerns of the Fe<sup>3+</sup> crosslinked HyA hydrogels can be minimized by reducing both the Fe<sup>3+</sup> and H<sup>+</sup> ion concentrations; and the acidity concern of H<sup>+</sup> ions could be eliminated by using other monovalent metal ions (M<sup>+</sup>) with appropriate K<sub>M</sub> instead of H<sup>+</sup> ions. Therefore, biocompatible and bioresorbable HyA hydrogels crosslinked via carboxylate- Fe<sup>3+</sup> coordination could be promising for biomedical applications such as tissue repair, wound healing, drug delivery, and cell delivery. For example, the hydrogels crosslinked via dynamic coordination could be promising as a cardiac patch because they can provide self-healing property to endure cyclic loading *in vivo*.<sup>36</sup>

Hydrogels crosslinked via dynamic metal-ligand coordination could provide attractive phase reversibility and self-healing capacity, while the hydrogels crosslinked with permanent chemical bonding could provide better structural stability.<sup>12</sup> Each crosslinking approach has its own advantages and disadvantages, which should be carefully considered when designing hydrogels for specific applications. For example, the

hydrogels crosslinked with permanent methacrylate bonding via UV curing are considered irreversible, but UV-crosslinked hydrogels have better structural stability than their counterparts crosslinked via metal-ligand coordination.<sup>28</sup> Photo-crosslinked hydrogels can retain their structural integrity longer when used for tissue repair in the body.<sup>67</sup> In contrast, HyA hydrogels crosslinked via dynamic metal-ligand coordination alone are expected to undergo significant swelling and lose structural integrity when used in a biological environment with abundant physiological fluid, such as the joint cavity filled with aqueous synovial fluid. Thus, the HyA hydrogel crosslinked via metal-ligand coordination may be unsuitable for applications that require long-term structural stability of hydrogels, but promising for certain applications where hydrogels are only needed to retain structural integrity for a short period.

In addition, HyA hydrogels can be chemically modified with functional groups such as IDA or BP, before crosslinking via metallic ion coordination, to meet the requirements for specific applications. For example, HyA conjugated with IDA was crosslinked by  $\text{Fe}^{3+}$  ions via IDA- $\text{Fe}^{3+}$  coordination to form a hydrogel for the prevention of peritoneal adhesion. In the *in vivo* studies using a rat model with sidewall defect and bowel abrasion, the animals treated with HyA\_IDA hydrogels showed a lower adhesion score of  $0.50 \pm 0.93$  than the non-treated control group of  $1.50 \pm 0.93$ , indicating a better clinical outcome of HyA\_IDA hydrogels in preventing peritoneal adhesion.<sup>13</sup> In another application, HyA modified with BP was crosslinked by  $\text{Ag}^+$  ions via BP- $\text{Ag}^+$  coordination and used for wound healing. The *in vivo* study using a rat model with full-thickness skin wounds showed that the thickness of the newly regenerated epidermal

layers in the wound treatment with the hydrogel at Day 10 post-surgery was  $144.4 \pm 32.5$   $\mu\text{m}$ , which was significantly higher than the non-treated control group with an epidermal thickness of  $63.8 \pm 32.4$   $\mu\text{m}$ , indicating the potential of the HyA hydrogels in regenerating skin tissue.<sup>68</sup>

Importantly, tunable crosslinking densities and reversible phase transition enabled the injectability and 3DP capability for HyA hydrogels, which could further extend the hydrogels to even broader applications. For example, injectable HyA hydrogels can fill tissue defects or wounds with irregular geometries and solidify via crosslinking *in situ*, thus conforming to the defect size and shape for better wound healing. Injectable hydrogels coupled with 3DP can produce well-controlled 3D structures with desirable porosity, pore size, and pore shape, leading to tunable mechanical properties and permeability, which is beneficial for wound healing. Moreover, HyA hydrogels (i.e., HyA\_P, HyA solution preloaded with cations) are promising ink materials for printing 3D tissues and organs with complex structures via our direct writing method. The buoyancy force applied on the printed constructs in aqueous solutions can offset the gravity effects, which can significantly increase the structural fidelity and stability. Live cells or biomolecules can be loaded into biocompatible hydrogel ink to print biomimetic tissues or organs. Hydrogel ink encapsulated with live cells can also be directly printed into the tissue defects *in situ*, for tissue repair or regeneration.

## 5.5 Conclusion

The *in vitro* cytocompatibility study showed that the HyA\_H\_3D and HyA\_H had higher average cell adhesion densities than HyA\_M, HyA\_P, and HyA\_L hydrogel groups under both direct and indirect contact conditions; and the cell adhesion densities in direct contact conditions were statistically lower than the same hydrogel groups under indirect contact conditions. The results also indicated that HyA hydrogels prepared via direct writing HyA solution in FeCl<sub>3</sub> solution showed excellent cytocompatibility. In the future, it is desirable to reduce the concentrations of Fe<sup>3+</sup> and H<sup>+</sup> ions in HyA hydrogels or use other monovalent metal ions to minimize the toxicity concerns for biomedical applications, following the thermodynamic and kinetic principles elucidated in this article.

## **CHAPTER 6 Incorporation of Magnetic Nanoparticles in the Hyaluronic Acid**

### **Hydrogels in Situ for Biomedical Applications**

#### **6.1 Introduction**

Hydrogels are three-dimensional (3D) polymeric networks that contain high water content in their structure. Hydrogels prepared from both natural and synthetic polymers have been extensively investigated and applied in various biomedical applications in recent decades.<sup>1, 69-71</sup> Hyaluronic acid (HyA) is one of the most well-known polymers that is utilized in hydrogel synthesis. HyA exists and plays significant roles in many tissues or organs. For example, it provides lubrication in the joint and serves as a shock absorber in synovial fluid.<sup>72</sup> In the skin, it helps immobilize the water in the tissue and regulate cell behaviors.<sup>73-74</sup> It is a very important component in the matrix of cartilage.<sup>75-76</sup> HyA hydrogels crosslinked via different reactions have been widely studied and applied in many biomedical applications, such as wound healing,<sup>77-78</sup> cell encapsulation,<sup>79-81</sup> cell therapy,<sup>82-84</sup> drug and cell delivery,<sup>85-87</sup> prevention of peritoneal adhesion,<sup>88-90</sup> and cosmetic applications.<sup>74</sup> Hydrogels with polymer-only composition usually have relatively low mechanical strength and modulus due to their high water content. The materials science tetrahedron demonstrates the processing, structure, properties, and performance of a material for a given application are inter-related. To alter the properties of the hydrogels, some modifications in processing and structure control are developed. For example, tunable mechanical properties of the hydrogels were achieved to control

their crosslinking density.<sup>91</sup> The integration of other materials such as ceramic and metallic materials in the polymeric networks is another common strategy to alter the microstructure and related properties of the hydrogel.

Nanocomposite hydrogels integrated the advantages of both polymers and nanoparticles. The incorporation of nanoparticles can alter the physicochemical properties of the composite hydrogels. The added properties may play an important role in improving the performance of the hydrogel for a specific application. Magnetic nanoparticles (MNPs) are the type of most commonly used nanoparticles that were embedded in the hydrogel matrix for biomedical applications.<sup>92-93</sup> MNPs can respond to the magnetic field and are promising in applications such as MRI,<sup>94-95</sup> drug delivery,<sup>96-97</sup> and hyperthermia.<sup>98</sup> For the addition of nanoparticles in the hydrogel phase, it is highly desirable to achieve the homogenous dispersion of nanoparticles. The traditional approach to load MNPs in the hydrogel phase is to mix the MNPs and the polymer solution directly, followed by the crosslinking process. It is relatively difficult to uniformly mix the MNPs and polymer solution, especially when the concentration of MNPs or polymer solution is high. Specifically, MNPs have high specific surface areas and will dramatically increase the viscosity of the polymer solution after mixing. HyA molecules have abundant carboxyl groups and exhibit negative charges, the HyA solution thus showed relatively high viscosity due to the entanglement of molecules. This further jeopardizes the MNP dispersion in the hydrogel. Moreover, although it is easier to uniformly mix the nanoparticles with the polymer solution at low concentration, phase separation will occur due to the settlement of the nanoparticle in a thin solution.

To enhance the dispersion of the nanoparticles in the hydrogel matrix, strategies have been developed to load the magnetic nanoparticles in situ.<sup>92, 99</sup> For example, the HyA solution can be crosslinked first to form hydrogel, and  $\text{Fe}^{3+}$  and  $\text{Fe}^{2+}$  ions at the molar ratio of 2:1 will be loaded into the hydrogel network. The HyA hydrogels loaded with  $\text{Fe}^{3+}$  and  $\text{Fe}^{2+}$  ions are then exposed to alkaline solutions such as ammonia hydroxide solution, and magnetic nanoparticles of  $\text{Fe}_3\text{O}_4$  will generate in situ in the hydrogel matrix via co-precipitation.

In our previous research, we demonstrated the tunable crosslinking and reversible phase transition of HyA hydrogels by controlling the coordination bonding between carboxyl groups on HyA and  $\text{Fe}^{3+}$  ions. We hypothesized that loading  $\text{Fe}^{3+}$  and  $\text{Fe}^{2+}$  ions in HyA solution can achieve the crosslinking of hydrogel while the MNPs will form in situ when immersed the hydrogel in the ammonia hydroxide solution. The  $\text{Fe}^{3+}$  ions will serve as the crosslinking agent and a source for MNP synthesis. The dispersion of the MNP will be enhanced and the MNP content in the hydrogel will be tunable by adjusting the concentration of  $\text{Fe}^{3+}$  and  $\text{Fe}^{2+}$  ions loaded in the hydrogel. The objective of this study is to incorporate MNPs in HyA hydrogels in situ using the co-precipitation approach and investigate the effects of  $\text{Fe}^{3+}$  and  $\text{Fe}^{2+}$  ion concentration on the content and dispersion of MNPs, as well as the cytocompatibility of the magnetic hydrogels.

## 6.2 Materials and Methods

### 6.2.1 Incorporate MNPs in HyA Hydrogels in Situ

The crosslinking of sodium hyaluronate (abbreviated as HyA; Bulk Supplements, Henderson, NV) solution followed the method reported previously, and the MNPs were generated in the crosslinked hydrogel network in situ via a co-precipitation approach, as shown in Figure 6.1. Briefly, 1 mL HyA solution at the concentration of 5 w/v% was injected onto the 10-mm petri dish using a syringe with a needle of 0.84 mm in diameter to form a thin layer. The as-injected HyA solution became a uniform layer with a thickness of around 1 mm via self-leveling. The mixed  $\text{Fe}^{3+}$  and  $\text{Fe}^{2+}$  ion solution at the  $\text{Fe}^{3+}$ :  $\text{Fe}^{2+}$  ratio of 2:1 was added into the petri dish to crosslink the HyA for 3 min. To control the MNP content in the magnetic hydrogel, different concentrations of 600 mM: 300 mM, 300 mM:150 mM, and 100 mM: 50 mM for  $\text{Fe}^{3+}$ :  $\text{Fe}^{2+}$  were utilized. The magnetic hydrogels were named as HyA/MNP\_H, HyA/MNP\_M, and HyA/MNP\_L to represent the hydrogels with high, medium, and low content of MNPs. The iron ion solution was poured into the waste bottle and the crosslinked hydrogels were cut into discs with a diameter of 13 mm using a hole punch. The hydrogels were rinsed using DI water to remove the iron ions on the surface and placed into the ammonia hydroxide solution at a concentration of 2.5-2.8%. After 5 min, the magnetic hydrogels were collected from the ammonia hydroxide solution and dehydrated using a lyophilizer (FreeZone Benchtop Freeze Dryer, Labconco). Specifically, the hydrogels were frozen in

-80 °C freezer for 2 hours and dehydrated in the lyophilizer at a temperature of -54 °C and a pressure of 0.01 mBar for 24 hours.

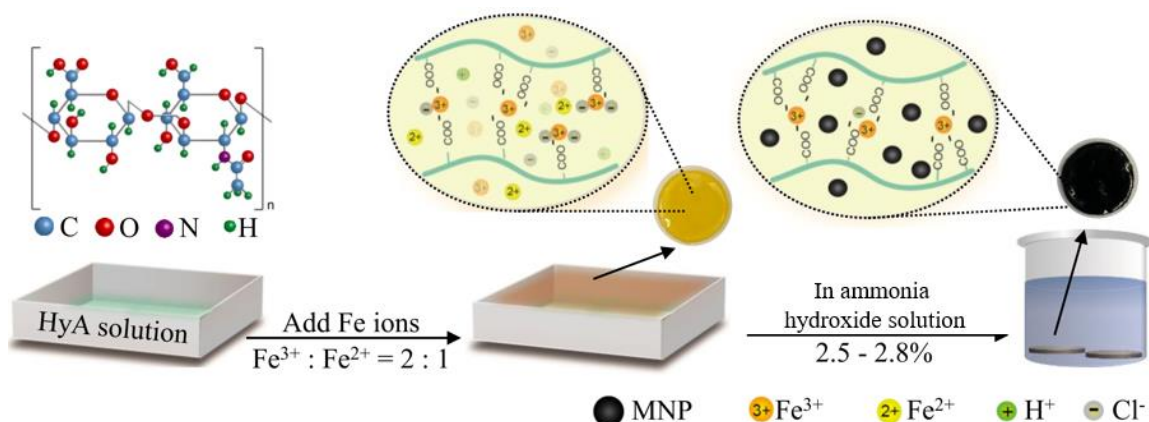


**Figure 6.1** Illustration showing procedures of incorporating MNPs in HyA hydrogels in situ.

## 6.2.2 Determine Microstructure and Elemental Composition

The microstructure and elemental composition of HyA/MNP\_H, HyA/MNP\_M, and HyA/MNP\_L was characterized using scanning electronic microscopy (SEM, Nova NanoSEM 450, FEI Co) and energy dispersive X-ray spectroscopy (EDS; X-Max 50 silicon drift detector). Specifically, the dehydrated HyA/MNP\_H, HyA/MNP\_M, and HyA/MNP\_L were cut into two pieces to expose the cross-sections and were mounted onto the SEM sample holder. The exposed cross-sections of the magnetic samples were coated with platinum/palladium layer using a sputter coater (model 108, Cressington Scientific Instruments Ltd., Watford, U.K.) at 20 mA with a 90 s sputter time. The sputter-coated cross-sections were characterized using an Everhart–Thornley detector (ETD) of SEM at an accelerating voltage of 5 kV, a spot size of 4, and the magnifications

of 200×, 3,500×, and 50,000×. Elemental compositions of the cross-sections of HyA/MNP\_H, HyA/MNP\_M, and HyA/MNP\_L were characterized using EDS attached to SEM with an accelerating voltage of 15 kV, a spot size of 4, and a magnification of 200×. Linear scanning was performed on both the edge and the center of the cross-section to compare their difference in elemental composition. EDS mapping images were also obtained to show the elemental distribution. Aztec Energy software (Oxford Instruments, Abingdon, Oxfordshire, U.K.) were used to analyze the elemental composition and distribution.

### **6.2.3 Determine Magnetic Response**

The magnetic response of the HyA/MNP\_H, HyA/MNP\_M, and HyA/MNP\_L was evaluated using a N42 neodymium magnet (#DEX0, K&J Magnetics, Inc., Pipersville, PA) with a diameter of 22 mm, a height of 25 mm, a pull force of 47.2 LB, and a surface field of 13,200 Gauss. The magnetic responses of HyA/MNP\_H, HyA/MNP\_M, and HyA/MNP\_L were tested in dry condition. Specifically, the dehydrated sample was placed in a petri dish, the N42 permanent magnet was then moved toward the sample. The maximum distance for magnetic responses were recorded using a video camera.

### **6.2.4 Thermogravimetric Analysis**

The HyA/MNP\_H, HyA/MNP\_M, and HyA/MNP\_L were analyzed using a thermogravimetric analyzer (TGA; TG 209 F1 Libra®, Netzsch) to determine their MNP content. Before the TGA testing, all the samples were lyophilized using the same method as described above. Briefly, the lyophilized HyA/MNP\_H, HyA/MNP\_M, and

HyA/MNP\_L of 5 mg each were placed in alumina crucibles and heated from 30 °C to 600 °C at a heating rate of 10 °C /min in a nitrogen (N<sub>2</sub>) atmosphere with a N<sub>2</sub> flow rate of 20 mL/min. The sample mass change over the temperature was analyzed and plotted.

### **6.2.5 Crystal Structure**

X-ray diffraction (XRD; Empyrean PANalytical) was used to analyze the crystal structure of the lyophilized HyA/MNP\_H, HyA/MNP\_M, and HyA/MNP\_L. The XRD was run at 45kV and 40 mA with a step size of 0.02°. The XRD spectra were compared with a library database using the HighScore software (PANalytical) to identify the phases.

### **6.2.6 Evaluation of the Cytocompatibility of Magnetic Hydrogels**

The descriptions of methods for this in vitro cell study are adapted with permission from Zhang, C.; Lin, J.; Nguyen, N.-Y. T.; Guo, Y.; Xu, C.; Seo, C.; Villafana, E.; Jimenez, H.; Chai, Y.; Guan, R. Antimicrobial Bioresorbable Mg–Zn–Ca Alloy for Bone Repair in a Comparison Study with Mg–Zn–Sr Alloy and Pure Mg. *ACS Biomater. Sci. Eng.* 2019, 6 (1), 517–538). Copyright (2020) American Chemical Society.

#### *6.2.6.1 Harvest and Culture BMSCs*

This part is the same as the protocol described in Chapter 5.

#### *6.2.6.2 BMSC Culture With Magnetic Hydrogels and Controls*

The lyophilized HyA/MNP\_H, HyA/MNP\_M, and HyA/MNP\_L were prepared similarly as described in 6.2.1. Before cell culture, these magnetic samples were immersed in DI water for 4 hours. HyA hydrogels without MNPs (HyA\_H), HyA without

crosslinking, and MNPs were also included in the cell culture. To prepare HyA\_H, HyA solution at the concentration of 5 w/v% was manually printed onto a petri dish using a syringe with a 0.84 mm needle. The printed filament had no gaps and formed a uniform thin layer after 10 minutes in air at room temperature. After that, 300 mM FeCl<sub>3</sub> solution was added to the petri dish to crosslink the HyA layer. The HyA hydrogel was obtained after a 3-min reaction. The as-prepared hydrogels were punched into a cylindrical shape with a diameter of 12.17±0.15 mm and immersed in sterilized DI water for 24 hours. Both sides of HyA/MNP\_H, HyA/MNP\_M, HyA/MNP\_L, and HyA\_H were disinfected under UV exposure for 30 min before cell culture. To prepare the HyA control, HyA powder was disinfected under UV exposure for 1 hour, 3 mg HyA powders (equivalent to the amount of HyA in a single HyA hydrogel sample) was then added into each culture well containing 3 mL of media. To prepare MNP control, MNPs were heated in an oven at 120 °C for 30 min and then weighed while they are still hot. The MNP concentration in the media for the MNP control was 1 mg/mL.

The direct exposure culture method was used to determine the cytocompatibility of magnetic hydrogels with BMSCs, as established in the previous publication. Briefly, BMSCs were seeded into each well of a 12-well plate with a seeding density of 10,000 cells/cm<sup>2</sup>. The cells in each well were cultured in 3 mL of media under standard cell culture conditions for 24 hours to form a monolayer of adherent cells. Afterward, the media and non-adhered cells were removed from each well, and the cells were rinsed using a phosphate-buffered solution (PBS) three times. For the groups of HyA/MNP\_H, HyA/MNP\_M, HyA/MNP\_L, and HyA\_H, the disinfected samples were then placed in

the culture wells, 3 mL of fresh media was added to each well. For the group of HyA and MNP control, 3 mL of media containing HyA or MNPs described above were added to the corresponding well. A positive control, designated as the “Cell-only” group, consisted of BMSCs cultured with the only DMEM in the wells, that is, without any samples. DMEM alone without cells and samples was also included as a blank medium reference and designated as the “Media” group. All the samples, control groups, and reference groups were run in triplicate.

#### *6.2.6.3 Characterize the BMSC Adhesion and Morphology*

After the prescribed cell culture, the photographs of samples in the media were recorded using a camera. The samples and post-culture media were collected for further analysis. BMSCs attached on the well-plates were rinsed using PBS three times and fixed with 4% formaldehyde (10% neutral buffered formalin; VWR, Radnor, PA, USA) for 20 min. The fixed BMSCs were stained with Alexa Flour 488-phalloidin (A12379, Life technologies) for F-actin for 20 min and 4',6-diamidino-2-phenylindole dilactate (DAPI, Invitrogen) for nuclei for 10 min. BMSCs were imaged using a fluorescence microscope (Eclipse Ti and NIS software, Nikon, Melville, NY, USA). DAPI-stained nuclei were counted to determine cell adhesion density per unit area. The fluorescence images of cells were analyzed using the ImageJ software to quantify the number of cells per unit area. The numbers of cells in each abovementioned spot were counted and divided by the image area to calculate the average cell adhesion density (cells/cm<sup>2</sup>).

#### *6.2.6.4 Analyze the Post-Culture Media*

The pH values of post-culture media were measured using a pre-calibrated pH meter (Symphony, model SB70P, VWR) immediately after collection. The ion concentrations of  $\text{Fe}^{3+}/\text{Fe}^{2+}$  and  $\text{Ca}^{2+}$  ions in the collected culture media were also measured using inductively coupled plasma optical emission spectrometry (ICP-OES; Optima 8000, PerkinElmer, Waltham, MA). To minimize the matrix effects in ICP-OES, the collected DMEM aliquots were diluted to 1:100 solutions in DI water (Millipore). Ionic concentrations were then calculated based on the calibration curves of Fe and Ca standards (PerkinElmer) diluted to the range of 0.1–1.0 mg/L, respectively.

#### **6.2.7 Statistical Analysis**

All numerical data in this study were obtained from experiments run in triplicate. The numerical data were examined using a one-way analysis of variance (ANOVA) followed by a Tukey test, when the data sets fulfilled the parametric criteria (i.e., data normality was greater than 0.05). Statistical significance was considered at  $p < 0.05$  for the Tukey test. For nonparametric data (i.e., data normality was less than 0.05), the data sets were examined using the Kruskal–Wallis analyses followed by a Dunn test and adjusted by Hochberg’s method. Statistical significance was considered at  $p < 0.025$  for the Dunn test.

## 6.3 Results

### 6.3.1 Microstructure and Elemental Composition

Figure 6.2 shows the microstructure and elemental composition of the cross-sections of lyophilized magnetic hydrogels. At the magnification of 200 $\times$ , all the samples of HyA/MNP\_H, HyA/MNP\_M, and HyA/MNP\_L had highly porous structures, suggesting their high water content before freeze drying. EDS mapping images show that the Fe element was uniformly distributed on the porous structure of the three samples. Linear scanning on the edge and center of the samples further indicated the Fe element was uniformly distributed in different areas. The MNP content in different magnetic hydrogels was calculated based on the EDS data. As expected, the magnetic hydrogel exhibited higher MNP content when higher concentrations of Fe<sup>3+</sup>/Fe<sup>2+</sup> were utilized during the synthesis. Specifically, HyA/MNP\_H had an MNP content of 53.34 wt.% on the edge and 53.90 wt.% on the center, HyA/MNP\_M showed an MNP content of 45.95 wt.% on the edge and 41.04 wt.% on the center, and HyA/MNP\_L exhibited an MNP content of 13.82 wt.% on the edge and 15.89 wt.% on the center.

SEM images with high magnifications of 3,500 $\times$  and 50,000 $\times$  showed dramatically different MNP morphologies in three magnetic samples. MNPs trended to agglomerate to larger particles in the sample of HyA/MNP\_H, while fewer agglomerations were found in the group of HyA/MNP\_M. The MNPs dispersed uniformly in the porous structure of HyA/MNP\_L, and no observable agglomeration was noticed.

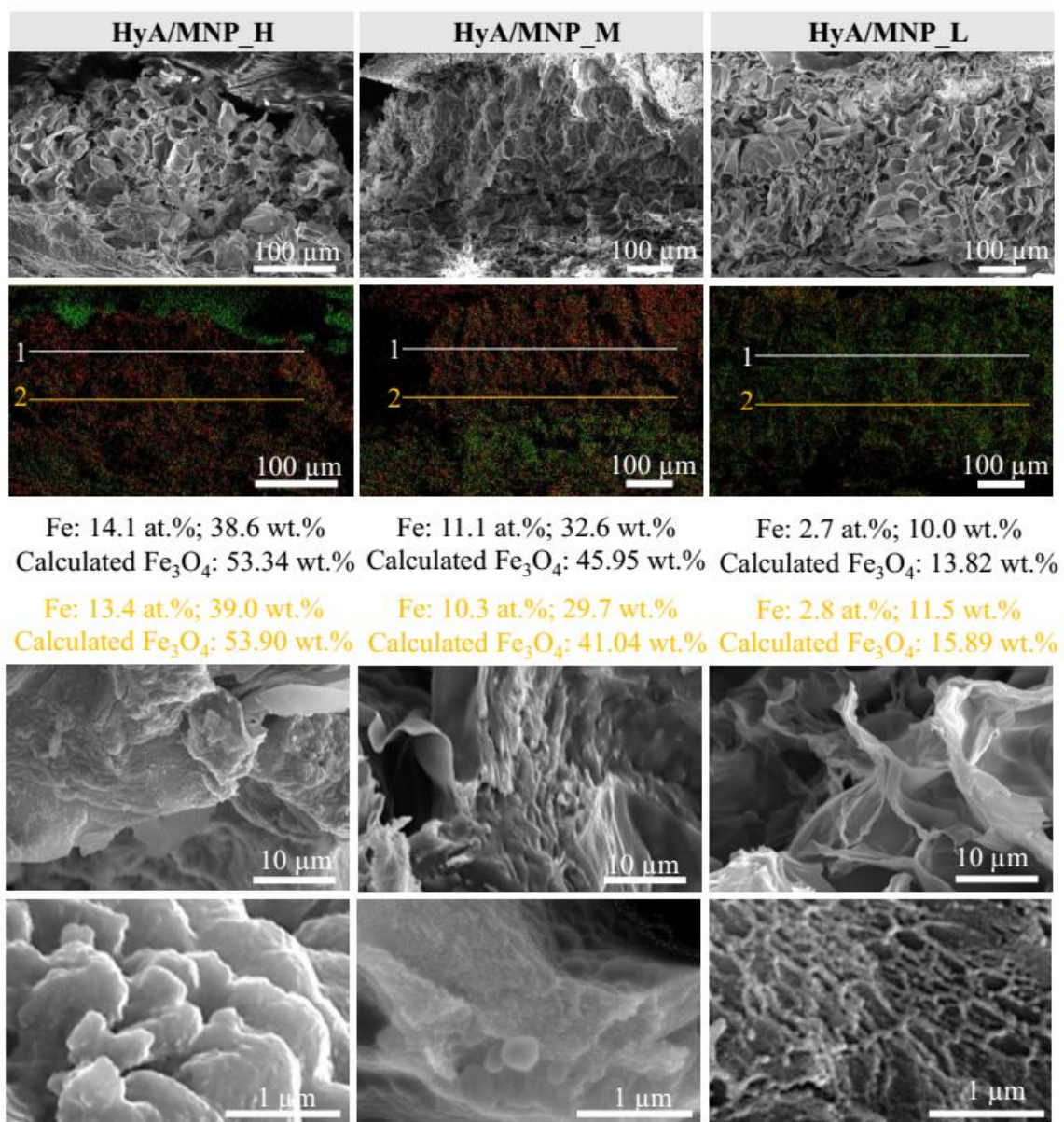


**Figure 6.2** Microstructure and elemental composition of the cross-sections of lyophilized magnetic hydrogels.

### 6.3.2 Magnetic Responses

Magnetic responses of the HyA-based magnetic hydrogels were evaluated *in vitro* for their potential to be magnetically guided in body fluids to a targeted location, as shown in Figure 6.3. As expected, the magnetic hydrogels with higher MNP contents showed a greater maximum distance that can respond to the magnet. Specifically, HyA/MNP\_H started to respond to the magnet at 30 mm away, HyA/MNP\_M started to respond to the magnet at 22 mm away, while HyA/MNP\_L started to show the magnetic response when the magnet was 17 mm away.

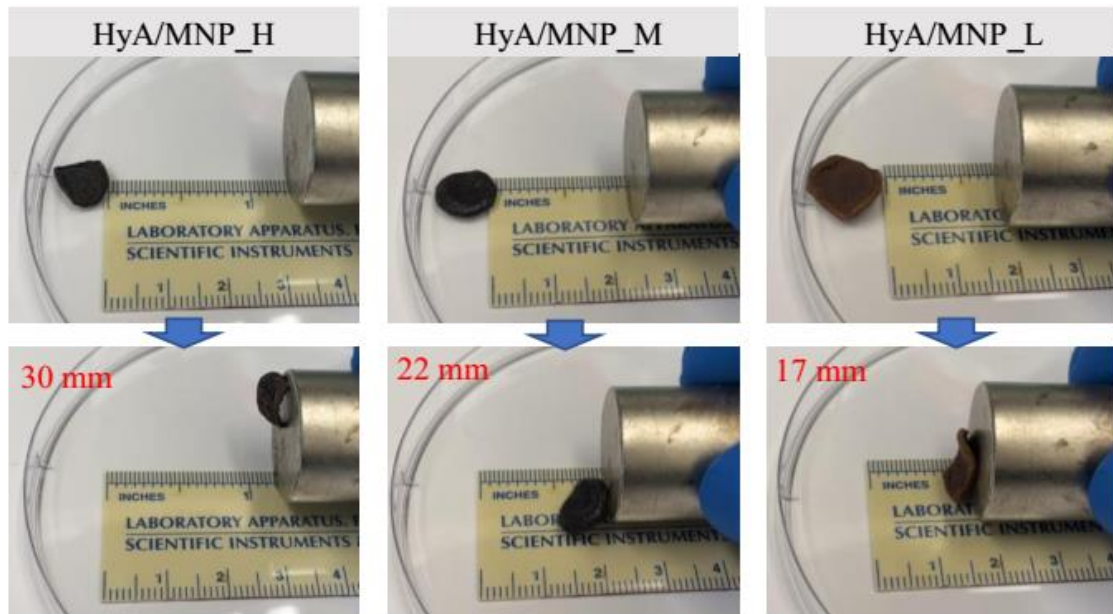


**Figure 6.3** Photographs showing the responses of magnetic hydrogels to a magnet.

### 6.3.3 MNP Content and Crystal Structure

TGA results in Figure 6.4a shows the percent mass over temperature for lyophilized HyA/MNP\_H, HyA/MNP\_M, HyA/MNP\_L, and HyA. and varied slopes were observed at distinct temperature ranges. Specifically, HyA/MNP\_H first underwent a continuous mass loss of 9.55% from 30 °C to 150 °C, followed by the second slope of 36.71% mass loss from 150 °C to 600 °C. After TGA for HyA/MNP\_H, 53.74% of the sample mass remained. HyA/MNP\_M showed a mass loss of 9.3% from 30 °C to 150 °C, and a second mass loss of 40.65% from 150 °C to 600 °C. The remained sample mass for HyA/MNP\_M was 50.05%. HyA/MNP\_L had a mass loss of 9.15% from 30 °C to 150 °C, followed by the second slope of 49.30 % mass loss from 150 °C to 600 °C. The remained sample mass for HyA/MNP\_L was 41.55%. For HyA control, it showed the first mass loss of 8% from 30 °C to 150 °C, and the second slope of 57.7% from 150 °C to 600 °C. The remained sample mass for HyA/MNP\_L was 34.21%. Because all of the samples have been lyophilized to remove free moisture before testing, the weight loss at the first slope was mainly attributed to the dehydration of bonded water. The weight loss from 150 °C to 600 °C was caused by the decomposition accompanied by the rupture of C–O and C–C bonds in the ring units resulting in the evolution of CO, CO<sub>2</sub>, and H<sub>2</sub>O, and formation of polynuclear aromatic and graphitic carbon structures.<sup>45</sup>

All the samples were lyophilized before the TGA, and thus the weight loss at the temperature below 150 °C is attributed to the removal of bonded water. The mass loss from 150 to 600 °C is attributed to decomposition of curcumin. The curcumin content in CMNP was calculated using the following equation (1).

$$MNP \text{ content} = R_{Total} - R_{Polymer} = R_{total} - ML_{Sample} / \frac{ML_{HyA}}{R_{HyA}} \quad (6.1)$$

where  $R_{Total}$  is the total mass remaining of the magnetic sample after TGA,  $R_{Polymer}$  is the mass remained caused by HyA in the magnetic sample,  $ML_{Sample}$  is the mass loss of each magnetic sample from 150 to 600 °C,  $ML_{HyA}$  is the mass loss of HyA control from 150 to 600 °C, and  $R_{HyA}$  is mass remaining of HyA group after TGA.

In Figure 6.3b, the major XRD peaks of (311), (400), (511), and (440) planes at the 5–65° 2θ angle range matched the JDCPS card (19-0629), confirming the presence of Fe<sub>3</sub>O<sub>4</sub> phase in HyA/MNP samples. No characteristic peak was found in HyA\_H control group. Moreover, major XRD peaks of (220), (311), (400), (511), and (440) planes at the 5–65° 2θ angle range were found in MNP control group.

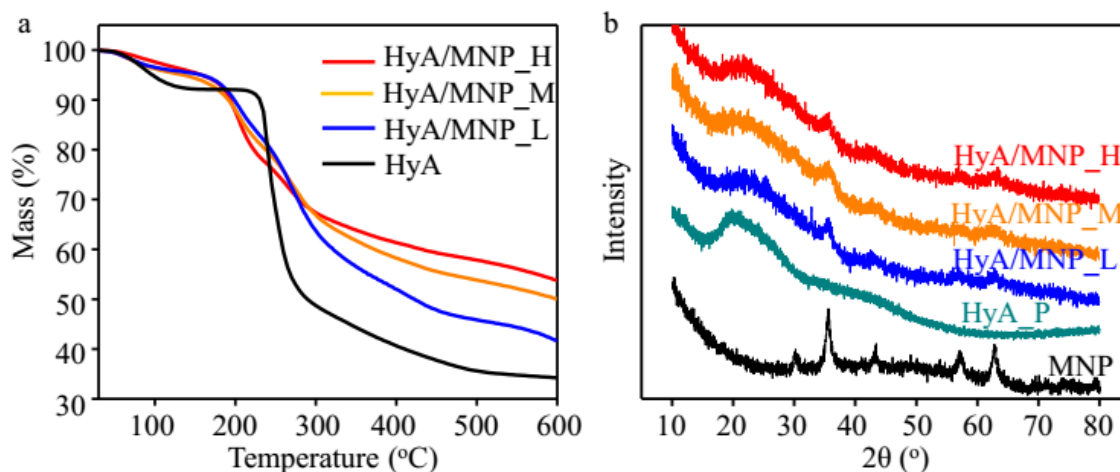
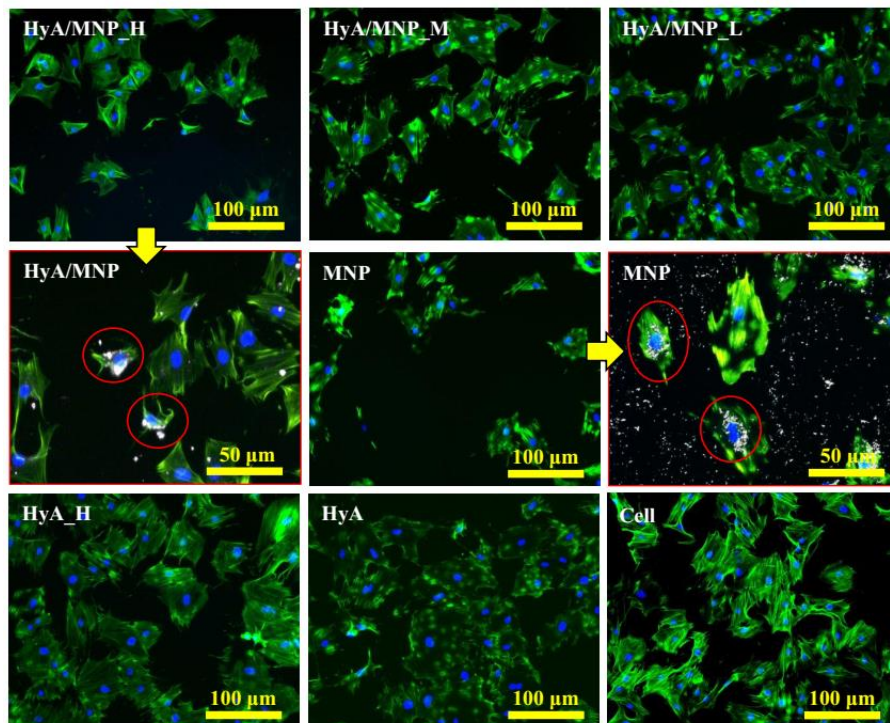


**Figure 6.4** Thermal properties and crystal structure of magnetic hydrogels. (a) Mass-temperature curves of magnetic hydrogels. (b) XRD spectra of magnetic hydrogels.

### 6.3.4 Cytocompatibility of Magnetic Hydrogels With BMSC in Vitro

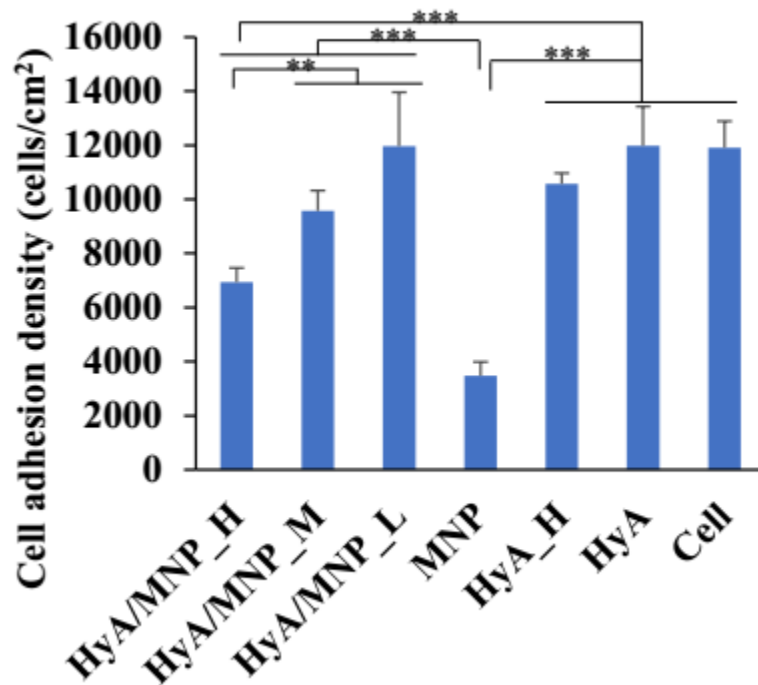
#### 6.3.4.1 BMSC Morphology and Adhesion Density After Direct Exposure Culture

Figure 6.5 shows the representative fluorescence images of BMSCs adhered on the culture plate after the 24-hour direct exposure culture. The fluorescence images show that BMSCs had normal morphology compared to Cell-only reference. For HyA/MNP hydrogels that had higher MNP contents, fewer BMSCs adhered on the well-plate. The images in the red boundary indicated the uptake of MNP in the BMSCs during the cell culture. As shown in the groups of HyA/MNP and MNP, MNPs (white dots) entered into the cells but surrounding the nuclei, indicating that the MNPs cannot enter nuclei.



**Figure 6.5** Representative fluorescence images of BMSCs cultured with magnetic hydrogels after a 24-hour direct exposure culture.

Figure 6.6 shows the quantitative BMSC adhesion density in the cultures with different hydrogel samples and control groups. For the magnetic hydrogels with the higher MNP content, the lower cell adhesion densities were shown. The group of HyA/MNP\_H show statistically lower cell adhesion density than all other groups except MNP control. The MNP control showed the lowest cell adhesion density among all the groups. No other statistical difference was detected among different groups.



**Figure 6.6** Quantitative cell adhesion density of BMSCs cultured with magnetic hydrogels after a 24-hour direct exposure culture.

#### *6.3.4.2 HyA Degradation, pH Values, and Fe<sup>3+</sup> and Ca<sup>2+</sup> Ion Concentrations in the Culture Media*

After 24 hours of cell culture, all the magnetic hydrogels of HyA/MNP\_H, HyA/MNP\_M, and HyA/MNP\_L swelled but retained their structural integrity, as shown in Figure 6.7. The samples of HyA\_H lost their structural integrity and were completely dissolved in the cell culture media. The pH value of the post-culture media was in a small range of 8-8.25, although some statistical differences were detected among the groups, as shown in Figure 6.8a. Figure 6.8b shows the Fe<sup>3+</sup> concentration in the post-culture media after 24 hours of direct exposure culture. Interestingly, magnetic hydrogel groups with higher MNP contents exhibited lower Fe<sup>3+</sup> concentration in the media. This may be because the hydrogel with higher MNP content had greater structural stability and fewer ions released from the hydrogel network to the media. Although the MNP control group had the greatest surface area among all the iron-containing samples, it showed the lowest Fe<sup>3+</sup> concentration among these groups. This is attributed to the fact that all other iron-containing groups had Fe<sup>3+</sup> ions. Figure 6.8c indicates that the groups of HyA/MNP\_H and HyA/MNP\_M had lower average Ca<sup>2+</sup> ion concentrations in the post-culture media than other groups. The negative charges of carboxyl groups on the HyA molecules can absorb cations such as Ca<sup>2+</sup> ions and good structural stability of these samples prevented the release of the absorbed Ca<sup>2+</sup> ions.

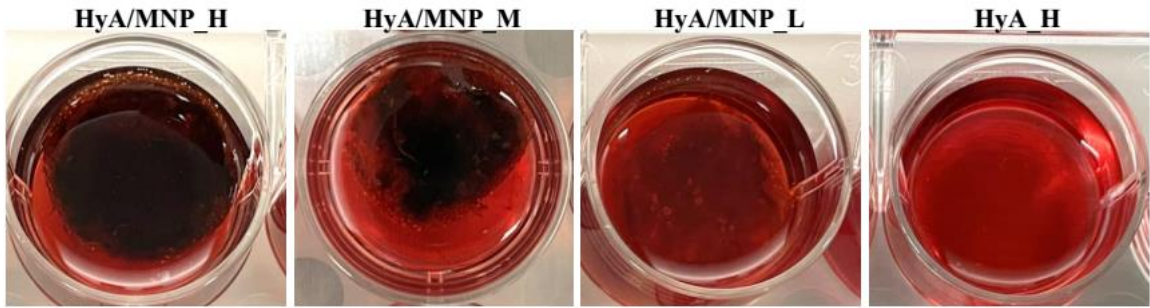


**Figure 6.7** Photographs showing the status of hydrogels after a 24-hour direct exposure culture.

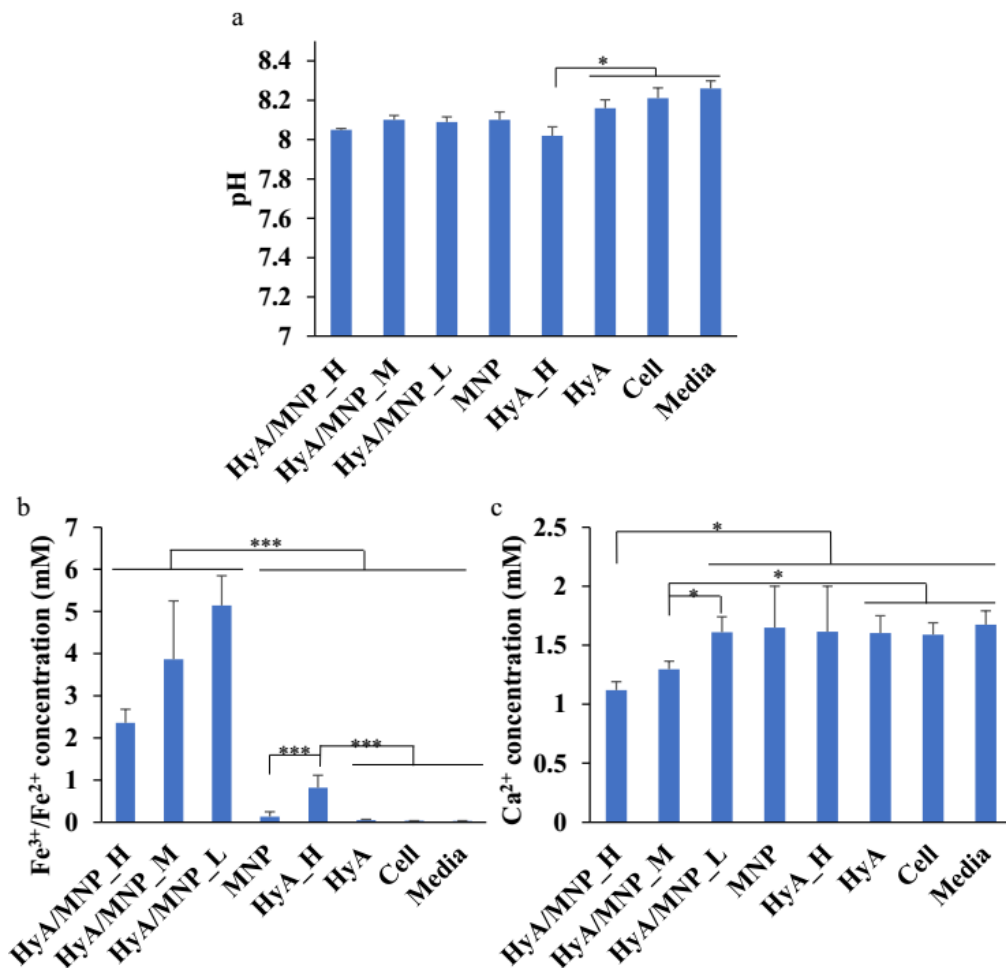


**Figure 6.8** Post-culture analysis of media. (a) pH value. (b) Fe<sup>3+</sup> concentration. (c) Ca<sup>2+</sup> concentration in the post-culture media after a 24-hour direct exposure culture.

## 6.4 Discussion

To improve the performance of nanocomposites for a specific application, achieving uniform dispersion of nanoparticles in the polymer phase is significant. The agglomeration or phase separation of nanoparticles in the polymer phase will change the properties of the material, such as surface properties, mechanical properties, and cytocompatibility. For example, Wetteland et al reported that PLGA (LA:GA = 50:50) with 30 wt.% agglomerated MgO nanoparticles showed significantly higher cell adhesion density than PLGA with 30 wt.% well-dispersed MgO nanoparticles.<sup>100</sup> This is because nanoparticle agglomeration increased direct contact of MgO with BMSCs and the concentration of MgO on the top surface was at a relatively high-level which is toxic to cells.<sup>100</sup>

Compared to the method that mix the nanoparticles with polymer solution directly, the incorporation of MNPs in situ significantly enhances the dispersion of MNPs. In this article,  $\text{Fe}^{3+}$  ions served as the crosslinking agent and a source for MNP synthesis. The strategy is different from the approach that loading  $\text{Fe}^{3+}$  and  $\text{Fe}^{2+}$  ions in pre-crosslinked hydrogels. Specifically, for pre-crosslinked hydrogels, the diffusion of the  $\text{Fe}^{3+}$  and  $\text{Fe}^{2+}$  ions is highly dependent on the crosslinking density of the hydrogel. For hydrogels with relatively high crosslinking density, a concentration gradient of  $\text{Fe}^{3+}$  and  $\text{Fe}^{2+}$  ions may exist in the hydrogel network. After the reaction in the alkaline solution, the concentration of MNPs in the edge and the center of the hydrogel may be distinct. In this article, however, the processes of  $\text{Fe}^{3+}$  and  $\text{Fe}^{2+}$  ion and hydrogel crosslinking occurred at the same time. Our previous results indicated that the HyA

solution was in a liquid phase at an equilibrium state when the concentration of  $\text{Fe}^{3+}$  ion was  $> 50$  mM. It suggested that diffusion of  $\text{Fe}^{3+}$  and  $\text{Fe}^{2+}$  ions in the HyA hydrogels would be easy during the crosslinking and ion-loading process. As a results, the MNPs showed uniform distribution in both the edge and the center of the hydrogels.

In this article, we only reported the incorporation of bare MNPs in the HyA hydrogels. However, bare MNPs may be oxidized and lose magnetism rapidly. To increase the stability of MNPs loaded in the hydrogels, some coatings may be applied to the MNPs. Our previous study indicated that curcumin and PVA coating can reduce the agglomeration and oxidization of the MNPs. As small molecules, curcumin can be loaded in the HyA solution and iron ion solution, and curcumin-coated MNPs can be incorporated into the HyA hydrogels after the alkaline treatment. The magnetic hydrogels with curcumin-coated MNPs are angiogenesis and promising in soft tissue repair. However, PVA coating may be hard to apply on the MNPs loaded in the HyA hydrogels in situ due to the entanglement of PVA and HyA polymeric chains. In the future, we may focus on the small molecule coating of MNPs which can be applied to the MNPs loaded in the HyA hydrogels in situ.

## **6.5 Conclusion**

In this chapter, MNPs were successfully incorporated in the HyA hydrogels in situ. The MNP content in the magnetic hydrogels was tunable by controlling the concentration of  $\text{Fe}^{3+}$  and  $\text{Fe}^{2+}$  ions. Magnetic hydrogels with low MNP content exhibited enhanced dispersion of MNPs but showed the lowest maximum distance that can respond

to a magnet. The results of 24-hour direct exposure culture with BMSCs indicated the magnetic hydrogels with higher MNP content exhibited lower cell adhesion density. In the future, coating based on small molecules such as curcumin may be applied in the synthesis to reduce the oxidation of MNPs in the magnetic hydrogels.

## Reference

- (1) Hoffman, A. S. Hydrogels for biomedical applications. *Advanced drug delivery reviews* **2012**, *64*, 18-23.
- (2) Burdick, J. A.; Prestwich, G. D. Hyaluronic acid hydrogels for biomedical applications. *Advanced materials* **2011**, *23* (12), H41-H56.
- (3) Collins, M. N.; Birkinshaw, C. Hyaluronic acid based scaffolds for tissue engineering—A review. *Carbohydrate polymers* **2013**, *92* (2), 1262-1279.
- (4) Garg, H. G.; Hales, C. A. *Chemistry and biology of hyaluronan*, Elsevier: 2004.
- (5) Huang, W. J.; Johns, D. B.; Kronenthal, R. L. Ionically crosslinked carboxyl-containing polysaccharides for adhesion prevention. *U.S. Patent* **1996**, 5,532,221.
- (6) Vorvolakos, K.; Isayeva, I. S.; Do Luu, H.-M.; Patwardhan, D. V.; Pollack, S. K. Ionically cross-linked hyaluronic acid: wetting, lubrication, and viscoelasticity of a modified adhesion barrier gel. *Medical Devices (Auckland, NZ)* **2011**, *4*, 1.
- (7) Tan, H.; Chu, C. R.; Payne, K. A.; Marra, K. G. Injectable in situ forming biodegradable chitosan–hyaluronic acid based hydrogels for cartilage tissue engineering. *Biomaterials* **2009**, *30* (13), 2499-2506.
- (8) Tan, H.; Rubin, J. P.; Marra, K. G. Injectable in situ forming biodegradable chitosan–hyaluronic acid based hydrogels for adipose tissue regeneration. *Organogenesis* **2010**, *6* (3), 173-180.
- (9) Bencherif, S. A.; Srinivasan, A.; Horkay, F.; Hollinger, J. O.; Matyjaszewski, K.; Washburn, N. R. Influence of the degree of methacrylation on hyaluronic acid hydrogels properties. *Biomaterials* **2008**, *29* (12), 1739-1749.
- (10) Shu, X. Z.; Liu, Y.; Luo, Y.; Roberts, M. C.; Prestwich, G. D. Disulfide cross-linked hyaluronan hydrogels. *Biomacromolecules* **2002**, *3* (6), 1304-1311.
- (11) Nimmo, C. M.; Owen, S. C.; Shoichet, M. S. Diels–Alder click cross-linked hyaluronic acid hydrogels for tissue engineering. *Biomacromolecules* **2011**, *12* (3), 824-830.
- (12) Poldervaart, M. T.; Goversen, B.; De Ruijter, M.; Abbadessa, A.; Melchels, F. P.; Öner, F. C.; Dhert, W. J.; Vermonden, T.; Alblas, J. 3D bioprinting of methacrylated

hyaluronic acid (MeHA) hydrogel with intrinsic osteogenicity. *PLoS One* **2017**, *12* (6), e0177628.

(13) Amano, Y.; Qi, P.; Nakagawa, Y.; Kirita, K.; Ohta, S.; Ito, T. Prevention of Peritoneal Adhesions by Ferric Ion-Cross-Linked Hydrogels of Hyaluronic Acid Modified with Iminodiacetic Acids. *ACS Biomaterials Science & Engineering* **2018**, *4* (9), 3405-3412.

(14) Ying, H.; Zhou, J.; Wang, M.; Su, D.; Ma, Q.; Lv, G.; Chen, J. In situ formed collagen-hyaluronic acid hydrogel as biomimetic dressing for promoting spontaneous wound healing. *Materials Science and Engineering: C* **2019**, *101*, 487-498.

(15) Zaviskova, K.; Tukmachev, D.; Dubisova, J.; Vackova, I.; Hejcl, A.; Bystronova, J.; Pravda, M.; Scigalkova, I.; Sulakova, R.; Velebny, V. Injectable hydroxyphenyl derivative of hyaluronic acid hydrogel modified with RGD as scaffold for spinal cord injury repair. *Journal of Biomedical Materials Research Part A* **2018**, *106* (4), 1129-1140.

(16) Johns, D. B.; Keyport, G. M.; Hoehler, F.; Group, I. A. P. S. Reduction of postsurgical adhesions with Intergel® adhesion prevention solution: a multicenter study of safety and efficacy after conservative gynecologic surgery. *Fertility and sterility* **2001**, *76* (3), 595-604.

(17) Saber, A. Effect of honey versus intergel in intraperitoneal adhesion prevention and colonic anastomotic healing: a randomized controlled study in rats. *International Journal of Surgery* **2010**, *8* (2), 121-127.

(18) Xu, X.; Zeng, Z.; Huang, Z.; Sun, Y.; Huang, Y.; Chen, J.; Ye, J.; Yang, H.; Yang, C.; Zhao, C. Near-infrared light-triggered degradable hyaluronic acid hydrogel for on-demand drug release and combined chemo-photodynamic therapy. *Carbohydrate Polymers* **2020**, *229*, 115394.

(19) Huang, G.; Huang, H. Hyaluronic acid-based biopharmaceutical delivery and tumor-targeted drug delivery system. *Journal of Controlled Release* **2018**, *278*, 122-126.

(20) Rajaram, A.; Schreyer, D.; Chen, D. Bioplotting alginate/hyaluronic acid hydrogel scaffolds with structural integrity and preserved schwann cell viability. *3D Printing and Additive Manufacturing* **2014**, *1* (4), 194-203.

(21) Gaetani, R.; Feyen, D. A.; Verhage, V.; Slaats, R.; Messina, E.; Christman, K. L.; Giacomello, A.; Doevendans, P. A.; Sluijter, J. P. Epicardial application of cardiac progenitor cells in a 3D-printed gelatin/hyaluronic acid patch preserves cardiac function after myocardial infarction. *Biomaterials* **2015**, *61*, 339-348.

- (22) Ge, M.; Sun, J.; Chen, M.; Tian, J.; Yin, H.; Yin, J. A hyaluronic acid fluorescent hydrogel based on fluorescence resonance energy transfer for sensitive detection of hyaluronidase. *Analytical and Bioanalytical Chemistry* **2020**, *412* (8), 1915-1923.
- (23) Ge, M.; Bai, P.; Chen, M.; Tian, J.; Hu, J.; Zhi, X.; Yin, H.; Yin, J. Utilizing hyaluronic acid as a versatile platform for fluorescence resonance energy transfer-based glucose sensing. *Analytical and bioanalytical chemistry* **2018**, *410* (9), 2413-2421.
- (24) Johns, D. B.; DiZerega, G. S. Development and clinical evaluation of Intergel adhesion prevention solution for the reduction of adhesions following peritoneal cavity surgery. In *Peritoneal surgery*; Springer: 2000; pp 351-366.
- (25) Collins, M. N.; Birkinshaw, C. Investigation of the swelling behavior of crosslinked hyaluronic acid films and hydrogels produced using homogeneous reactions. *Journal of Applied Polymer Science* **2008**, *109* (2), 923-931.
- (26) Vanderhooft, J. L.; Alcoutlabi, M.; Magda, J. J.; Prestwich, G. D. Rheological Properties of Cross - Linked Hyaluronan - Gelatin Hydrogels for Tissue Engineering. *Macromolecular bioscience* **2009**, *9* (1), 20-28.
- (27) Collins, M.; Birkinshaw, C. Comparison of the effectiveness of four different crosslinking agents with hyaluronic acid hydrogel films for tissue - culture applications. *Journal of Applied Polymer Science* **2007**, *104* (5), 3183-3191.
- (28) Shi, L.; Carstensen, H.; Hölzl, K.; Lunzer, M.; Li, H.; Hilborn, J.; Ovsianikov, A.; Ossipov, D. A. Dynamic coordination chemistry enables free directional printing of biopolymer hydrogel. *Chemistry of Materials* **2017**, *29* (14), 5816-5823.
- (29) Tomihata, K.; Ikada, Y. Crosslinking of hyaluronic acid with water - soluble carbodiimide. *Journal of Biomedical Materials Research: An Official Journal of The Society for Biomaterials and The Japanese Society for Biomaterials* **1997**, *37* (2), 243.
- (30) Zhang, Y.; Yang, B.; Zhang, X.; Xu, L.; Tao, L.; Li, S.; Wei, Y. A magnetic self-healing hydrogel. *Chemical Communications* **2012**, *48* (74), 9305-9307.
- (31) Cao, Y.; Tan, Y. J.; Li, S.; Lee, W. W.; Guo, H.; Cai, Y.; Wang, C.; Tee, B. C.-K. Self-healing electronic skins for aquatic environments. *Nature Electronics* **2019**, *2* (2), 75-82.
- (32) Cao, Y.; Wu, H.; Allec, S. I.; Wong, B. M.; Nguyen, D. S.; Wang, C. A Highly Stretchy, Transparent Elastomer with the Capability to Automatically Self - Heal Underwater. *Advanced Materials* **2018**, *30* (49), 1804602.

- (33) Zheng, S. Y.; Ding, H.; Qian, J.; Yin, J.; Wu, Z. L.; Song, Y.; Zheng, Q. Metal-coordination complexes mediated physical hydrogels with high toughness, stick–slip tearing behavior, and good processability. *Macromolecules* **2016**, *49* (24), 9637-9646.
- (34) Jeon, I.; Cui, J.; Illeperuma, W. R.; Aizenberg, J.; Vlassak, J. J. Extremely stretchable and fast self - healing hydrogels. *Advanced Materials* **2016**, *28* (23), 4678-4683.
- (35) Shi, L.; Ding, P.; Wang, Y.; Zhang, Y.; Ossipov, D.; Hilborn, J. Self - Healing Polymeric Hydrogel Formed by Metal–Ligand Coordination Assembly: Design, Fabrication, and Biomedical Applications. *Macromolecular rapid communications* **2019**, *40* (7), 1800837.
- (36) Lin, X.; Liu, Y.; Bai, A.; Cai, H.; Bai, Y.; Jiang, W.; Yang, H.; Wang, X.; Yang, L.; Sun, N. A viscoelastic adhesive epicardial patch for treating myocardial infarction. *Nature biomedical engineering* **2019**, *3* (8), 632-643.
- (37) Ouyang, L.; Highley, C. B.; Rodell, C. B.; Sun, W.; Burdick, J. A. 3D printing of shear-thinning hyaluronic acid hydrogels with secondary cross-linking. *ACS Biomaterials Science & Engineering* **2016**, *2* (10), 1743-1751.
- (38) Highley, C. B.; Rodell, C. B.; Burdick, J. A. Direct 3D printing of shear - thinning hydrogels into self - healing hydrogels. *Advanced Materials* **2015**, *27* (34), 5075-5079.
- (39) Lee, J.; Chang, K.; Kim, S.; Gite, V.; Chung, H.; Sohn, D. Phase controllable hyaluronic acid hydrogel with iron (III) ion–catechol induced dual cross-linking by utilizing the gap of gelation kinetics. *Macromolecules* **2016**, *49* (19), 7450-7459.
- (40) Ryu, J.; Kim, S.; Oh, I.; Kato, S.; Kosuge, T.; Sokolova, A. V.; Lee, J.; Otsuka, H.; Sohn, D. Internal Structure of Hyaluronic Acid Hydrogels Controlled by Iron (III) Ion–Catechol Complexation. *Macromolecules* **2019**, *52* (17), 6502-6513.
- (41) Williams, C. G.; Malik, A. N.; Kim, T. K.; Manson, P. N.; Elisseeff, J. H. Variable cytocompatibility of six cell lines with photoinitiators used for polymerizing hydrogels and cell encapsulation. *Biomaterials* **2005**, *26* (11), 1211-1218.
- (42) Leggat, P. A.; Kedjarune, U. Toxicity of methyl methacrylate in dentistry. *International dental journal* **2003**, *53* (3), 126-131.
- (43) Amira, S.; Spångberg, D.; Probst, M.; Hermansson, K. Molecular dynamics simulation of Fe<sup>2+</sup> (aq) and Fe<sup>3+</sup> (aq). *The Journal of Physical Chemistry B* **2004**, *108* (1), 496-502.

- (44) Curtiss, L.; Halley, J. W.; Hautman, J. Many-body effects in ion-water interactions: Fe<sup>3+</sup> in water. *Chemical physics* **1989**, *133* (1), 89-94.
- (45) Parikh, A.; Madamwar, D. Partial characterization of extracellular polysaccharides from cyanobacteria. *Bioresource Technology* **2006**, *97* (15), 1822-1827.
- (46) Wang, H.-L.; Cui, J.-Y.; Jiang, W.-F. Synthesis, characterization and flocculation activity of novel Fe (OH) 3–polyacrylamide hybrid polymer. *Materials Chemistry and Physics* **2011**, *130* (3), 993-999.
- (47) Stutz, H.; Illers, K. H.; Mertes, J. A generalized theory for the glass transition temperature of crosslinked and uncrosslinked polymers. *Journal of Polymer Science Part B: Polymer Physics* **1990**, *28* (9), 1483-1498.
- (48) Chen, F.; Clough, A.; Reinhard, B. M.; Grinstaff, M. W.; Jiang, N.; Koga, T.; Tsui, O. K. C. Glass transition temperature of polymer–nanoparticle composites: effect of polymer–particle interfacial energy. *Macromolecules* **2013**, *46* (11), 4663-4669.
- (49) Oh, H.; Green, P. F. Polymer chain dynamics and glass transition in athermal polymer/nanoparticle mixtures. *Nature materials* **2009**, *8* (2), 139-143.
- (50) Ash, B. J.; Siegel, R. W.; Schadler, L. S. Glass - transition temperature behavior of alumina/PMMA nanocomposites. *Journal of Polymer Science Part B: Polymer Physics* **2004**, *42* (23), 4371-4383.
- (51) Lin, P.; Ma, S.; Wang, X.; Zhou, F. Molecularly engineered dual - crosslinked hydrogel with ultrahigh mechanical strength, toughness, and good self - recovery. *Advanced Materials* **2015**, *27* (12), 2054-2059.
- (52) Appel, E. A.; del Barrio, J.; Loh, X. J.; Scherman, O. A. Supramolecular polymeric hydrogels. *Chemical Society Reviews* **2012**, *41* (18), 6195-6214.
- (53) Xu, C.; Hung, C.; Cao, Y.; Liu, H. H. Tunable crosslinking, reversible phase transition, and 3D printing of hyaluronic acid hydrogels via dynamic coordination of innate carboxyl groups and metallic ions. *ACS Applied Bio Materials* **2021**, *4* (3), 2408-2428.
- (54) Li, J.; Wu, C.; Chu, P. K.; Gelinsky, M. 3D printing of hydrogels: Rational design strategies and emerging biomedical applications. *Materials Science and Engineering: R: Reports* **2020**, *140*, 100543.

- (55) Kirchmajer, D. M.; Gorkin Iii, R. An overview of the suitability of hydrogel-forming polymers for extrusion-based 3D-printing. *Journal of Materials Chemistry B* **2015**, *3* (20), 4105-4117.
- (56) Xu, C.; Chen, Y.; Lin, J.; Liu, H. H. Direct and Indirect Culture Methods for Studying Biodegradable Implant Materials In Vitro. *Journal of Visualized Experiments: Jove* **2022**, (182).
- (57) Tian, Q.; Deo, M.; Rivera-Castaneda, L.; Liu, H. Cytocompatibility of magnesium alloys with human urothelial cells: a comparison of three culture methodologies. *ACS Biomaterials Science & Engineering* **2016**, *2* (9), 1559-1571.
- (58) Rutherford, D.; Exarhos, S.; Xu, C.; Niagaris, M.; Mariano, C.; Dayap, B.; Mangolini, L.; Liu, H. Synthesis, characterization, and cytocompatibility of yttria stabilized zirconia nanopowders for creating a window to the brain. *Journal of Biomedical Materials Research Part B: Applied Biomaterials* **2020**, *108* (3), 925-938.
- (59) Zhang, C.; Lin, J.; Nguyen, N.-Y. T.; Guo, Y.; Xu, C.; Seo, C.; Villafana, E.; Jimenez, H.; Chai, Y.; Guan, R. Antimicrobial Bioresorbable Mg–Zn–Ca Alloy for Bone Repair in a Comparison Study with Mg–Zn–Sr Alloy and Pure Mg. *ACS Biomaterials Science & Engineering* **2019**, *6* (1), 517-538.
- (60) Xu, C.; Uahengo, G.; Rudnicki, C.; Hung, C.; Huang, A.; Xu, Q.; Chen, Y.; Halaney, D. L.; Garay, J. E.; Mangolini, L. Nanocrystalline Yttria-Stabilized Zirconia Ceramics for Cranial Window Applications. *ACS Applied Bio Materials* **2022**.
- (61) Daya, R.; Xu, C.; Nguyen, N.-Y. T.; Liu, H. H. Angiogenic Hyaluronic Acid Hydrogels with Curcumin-Coated Magnetic Nanoparticles for Tissue Repair. *ACS Applied Materials & Interfaces* **2022**, *14* (9), 11051-11067.
- (62) Meng, X.; Letterman, R. D. Effect of component oxide interaction on the adsorption properties of mixed oxides. *Environmental science & technology* **1993**, *27* (5), 970-975.
- (63) Wetteland, C. L.; de Jesus Sanchez, J.; Silken, C. A.; Nguyen, N.-Y. T.; Mahmood, O.; Liu, H. Dissociation of magnesium oxide and magnesium hydroxide nanoparticles in physiologically relevant fluids. *Journal of Nanoparticle Research* **2018**, *20* (8), 215.
- (64) Caicedo, M.; Jacobs, J. J.; Reddy, A.; Hallab, N. J. Analysis of metal ion - induced DNA damage, apoptosis, and necrosis in human (Jurkat) T - cells demonstrates Ni<sup>2+</sup> and V<sup>3+</sup> are more toxic than other metals: Al<sup>3+</sup>, Be<sup>2+</sup>, Co<sup>2+</sup>, Cr<sup>3+</sup>, Cu<sup>2+</sup>, Fe<sup>3+</sup>, Mo<sup>5+</sup>, Nb<sup>5+</sup>, Zr<sup>2+</sup>. *Journal of Biomedical Materials Research Part A: An Official Journal of The Society for Biomaterials, The Japanese Society for Biomaterials, and The Australian Society for Biomaterials and the Korean Society for Biomaterials* **2008**, *86* (4), 905-913.

- (65) Budak, H.; Gonul, N.; Ceylan, H.; Kocpinar, E. F. Impact of long term Fe<sup>3+</sup> toxicity on expression of glutathione system in rat liver. *Environmental Toxicology and Pharmacology* **2014**, *37* (1), 365-370.
- (66) Albretsen, J. The toxicity of iron, an essential element. *VETERINARY MEDICINE-BONNER SPRINGS THEN EDWARDSVILLE-* **2006**, *101* (2), 82.
- (67) Levett, P. A.; Hutmacher, D. W.; Malda, J.; Klein, T. J. Hyaluronic acid enhances the mechanical properties of tissue-engineered cartilage constructs. *PloS one* **2014**, *9* (12), e113216.
- (68) Shi, L.; Zhao, Y.; Xie, Q.; Fan, C.; Hilborn, J.; Dai, J.; Ossipov, D. A. Moldable hyaluronan hydrogel enabled by dynamic metal–bisphosphonate coordination chemistry for wound healing. *Advanced healthcare materials* **2018**, *7* (5), 1700973.
- (69) Deligkaris, K.; Tadele, T. S.; Olthuis, W.; van den Berg, A. Hydrogel-based devices for biomedical applications. *Sensors and Actuators B: Chemical* **2010**, *147* (2), 765-774.
- (70) Daly, A. C.; Riley, L.; Segura, T.; Burdick, J. A. Hydrogel microparticles for biomedical applications. *Nature Reviews Materials* **2020**, *5* (1), 20-43.
- (71) Cascone, S.; Lamberti, G. Hydrogel-based commercial products for biomedical applications: A review. *International journal of pharmaceutics* **2020**, *573*, 118803.
- (72) Swann, D. A.; Radin, E. L.; Nazimiec, M.; Weisser, P. A.; Curran, N.; Lewinnek, G. Role of hyaluronic acid in joint lubrication. *Annals of the rheumatic diseases* **1974**, *33* (4), 318.
- (73) Papakonstantinou, E.; Roth, M.; Karakiulakis, G. Hyaluronic acid: A key molecule in skin aging. *Dermato-endocrinology* **2012**, *4* (3), 253-258.
- (74) Bukhari, S. N. A.; Roswandi, N. L.; Waqas, M.; Habib, H.; Hussain, F.; Khan, S.; Sohail, M.; Ramli, N. A.; Thu, H. E.; Hussain, Z. Hyaluronic acid, a promising skin rejuvenating biomedicine: A review of recent updates and pre-clinical and clinical investigations on cosmetic and nutricosmetic effects. *International journal of biological macromolecules* **2018**, *120*, 1682-1695.
- (75) Kim, I. L.; Mauck, R. L.; Burdick, J. A. Hydrogel design for cartilage tissue engineering: a case study with hyaluronic acid. *Biomaterials* **2011**, *32* (34), 8771-8782.
- (76) Holmes, M.; Bayliss, M.; Muir, H. Hyaluronic acid in human articular cartilage. Age-related changes in content and size. *Biochemical Journal* **1988**, *250* (2), 435-441.

- (77) Neuman, M. G.; Nanau, R. M.; Oruña-Sánchez, L.; Coto, G. Hyaluronic acid and wound healing. *Journal of pharmacy & pharmaceutical sciences* **2015**, *18* (1), 53-60.
- (78) Price, R. D.; Myers, S.; Leigh, I. M.; Navsaria, H. A. The role of hyaluronic acid in wound healing. *American journal of clinical dermatology* **2005**, *6* (6), 393-402.
- (79) Khademhosseini, A.; Eng, G.; Yeh, J.; Fukuda, J.; Blumling III, J.; Langer, R.; Burdick, J. A. Micromolding of photocrosslinkable hyaluronic acid for cell encapsulation and entrapment. *Journal of Biomedical Materials Research Part A: An Official Journal of The Society for Biomaterials, The Japanese Society for Biomaterials, and The Australian Society for Biomaterials and the Korean Society for Biomaterials* **2006**, *79* (3), 522-532.
- (80) Choh, S.-Y.; Cross, D.; Wang, C. Facile synthesis and characterization of disulfide-cross-linked hyaluronic acid hydrogels for protein delivery and cell encapsulation. *Biomacromolecules* **2011**, *12* (4), 1126-1136.
- (81) Coates, E. E.; Riggin, C. N.; Fisher, J. P. Photocrosslinked alginate with hyaluronic acid hydrogels as vehicles for mesenchymal stem cell encapsulation and chondrogenesis. *Journal of Biomedical Materials Research Part A* **2013**, *101* (7), 1962-1970.
- (82) López Ruiz, E.; Jiménez, G.; Álvarez Cienfuegos Rodríguez, L.; Antich Acedo, C.; Sabata, R.; Marchal Corrales, J. A.; Gálvez Martín, P. Advances of hyaluronic acid in stem cell therapy and tissue engineering, including current clinical trials. **2019**.
- (83) Shin, J.; Lee, J. S.; Lee, C.; Park, H. J.; Yang, K.; Jin, Y.; Ryu, J. H.; Hong, K. S.; Moon, S. H.; Chung, H. M. Tissue adhesive catechol - modified hyaluronic acid hydrogel for effective, minimally invasive cell therapy. *Advanced Functional Materials* **2015**, *25* (25), 3814-3824.
- (84) Lee, H.; Lee, T. W.; Chandrasekharan, A.; Sung, S.-E.; Yim, S.-G.; Kim, S.; Seong, K.-Y.; Seo, M.-S.; Yang, S. Y. Injectable Self-Crosslinkable Thiolated Hyaluronic Acid for Stem Cell Therapy of Atopic Dermatitis. *ACS Biomaterials Science & Engineering* **2022**, *8* (4), 1613-1622.
- (85) Huang, G.; Huang, H. Application of hyaluronic acid as carriers in drug delivery. *Drug delivery* **2018**, *25* (1), 766-772.
- (86) Mero, A.; Campisi, M. Hyaluronic acid bioconjugates for the delivery of bioactive molecules. *Polymers* **2014**, *6* (2), 346-369.
- (87) Jin, Y.-J.; Ubonvan, T.; Kim, D.-D. Hyaluronic acid in drug delivery systems. *Journal of Pharmaceutical Investigation* **2010**, *40* (spc), 33-43.

- (88) Ito, T.; Yeo, Y.; Highley, C. B.; Bellas, E.; Benitez, C. A.; Kohane, D. S. The prevention of peritoneal adhesions by in situ cross-linking hydrogels of hyaluronic acid and cellulose derivatives. *Biomaterials* **2007**, *28* (6), 975-983.
- (89) Chen, C.-H.; Chen, S.-H.; Mao, S.-H.; Tsai, M.-J.; Chou, P.-Y.; Liao, C.-H.; Chen, J.-P. Injectable thermosensitive hydrogel containing hyaluronic acid and chitosan as a barrier for prevention of postoperative peritoneal adhesion. *Carbohydrate polymers* **2017**, *173*, 721-731.
- (90) Sakai, S.; Ueda, K.; Taya, M. Peritoneal adhesion prevention by a biodegradable hyaluronic acid-based hydrogel formed in situ through a cascade enzyme reaction initiated by contact with body fluid on tissue surfaces. *Acta biomaterialia* **2015**, *24*, 152-158.
- (91) Jang, J.; Seol, Y.-J.; Kim, H. J.; Kundu, J.; Kim, S. W.; Cho, D.-W. Effects of alginate hydrogel cross-linking density on mechanical and biological behaviors for tissue engineering. *Journal of the Mechanical Behavior of Biomedical Materials* **2014**, *37*, 69-77.
- (92) Li, Y.; Huang, G.; Zhang, X.; Li, B.; Chen, Y.; Lu, T.; Lu, T. J.; Xu, F. Magnetic hydrogels and their potential biomedical applications. *Advanced Functional Materials* **2013**, *23* (6), 660-672.
- (93) Zhang, J.; Huang, Q.; Du, J. Recent advances in magnetic hydrogels. *Polymer International* **2016**, *65* (12), 1365-1372.
- (94) Schenck, J. F. The role of magnetic susceptibility in magnetic resonance imaging: MRI magnetic compatibility of the first and second kinds. *Medical physics* **1996**, *23* (6), 815-850.
- (95) Jin, J. *Electromagnetic analysis and design in magnetic resonance imaging*, Routledge: 2018.
- (96) Arruebo, M.; Fernández-Pacheco, R.; Ibarra, M. R.; Santamaría, J. Magnetic nanoparticles for drug delivery. *Nano today* **2007**, *2* (3), 22-32.
- (97) Tietze, R.; Zaloga, J.; Unterweger, H.; Lyer, S.; Friedrich, R. P.; Janko, C.; Pöttler, M.; Dürr, S.; Alexiou, C. Magnetic nanoparticle-based drug delivery for cancer therapy. *Biochemical and biophysical research communications* **2015**, *468* (3), 463-470.
- (98) Ortega, D.; Pankhurst, Q. A. Magnetic hyperthermia. *Nanoscience* **2013**, *1* (60), e88.

(99) Haas, W.; Zrinyi, M.; Kilian, H.-G.; Heise, B. Structural analysis of anisometric colloidal iron (III)-hydroxide particles and particle-aggregates incorporated in poly (vinyl-acetate) networks. *Colloid and Polymer Science* **1993**, *271* (11), 1024-1034.

(100) Wetteland, C. L.; Liu, H. Optical and biological properties of polymer - based nanocomposites with improved dispersion of ceramic nanoparticles. *Journal of Biomedical Materials Research Part A* **2018**, *106* (10), 2692-2707.